Surface plasmon resonance in gold nanoparticles: a review

Vincenzo Amendola,[1,*] Roberto Pilot,[1] Marco Frasconi,[1] Onofrio M. Maragò,[2] Maria Antonia Iatì[2]

[1] Department of Chemical Sciences, University of Padova, via Marzolo 1, I-35131 Padova, Italy and INSTM, UdR Padova, Italy

[2] CNR-IPCF, Istituto per i Processi Chimico-Fisici, v.le F. Stagno D'Alcontres 37, I-98158 Messina, Italy

* Correspondence: vincenzo.amendola@unipd.it

Abstract

In the last two decades, plasmon resonance in gold nanoparticles (Au NPs) has been the subject of intense research efforts. Plasmon physics is intriguing and its precise modelling proved to be challenging. In fact, plasmons are highly responsive to a multitude of factors, either intrinsic of the Au NPs or from the environment, and recently emerged the need for the correction of standard electromagnetic approaches with quantum effects. Applications related to plasmon absorption and scattering in Au NPs are impressively numerous, ranging from sensing to photothermal effects to cell imaging. Also plasmon enhanced phenomena are highly interesting for multiple purposes, including, for instance, Raman spectroscopy of nearby analytes, catalysis or sunlight energy conversion. In addition, plasmon excitation is involved in a series of advanced physical processes such as non-linear optics, optical trapping, magneto-plasmonics and optical activity. Here we provide the general overview of the field and the background for appropriate modelling of the physical phenomena. Then, we report on the current state of the art and most recent applications of plasmon resonance in Au NPs.

Introduction.

In the last decades, gold nanoparticles (Au NPs) have been the subject of a vast and exponentially growing literature. As their name entails, the small size of Au NPs is attractive for biomedical use in sensing,[1, 2] cellular imaging,[3, 4] drug delivery,[5] and cancer therapy,[6] but intensive research efforts are also directed to chemical analysis and catalysis,[7-10] electronics[11, 12] and non linear optical processes.[13, 14] This broad range of applications fostered a parallel research on a multitude of basic physical effects occurring in Au NPs.[15, 16]

The main reasons behind the success of Au NPs in the panorama of nanoscience and nanotechnology are three:[17-19] *i)* the high chemical and physical stability, also implying the intrinsic biocompatibility of gold nanostructures (colloidal gold was exploited for curative purposes since the Middle Ages), *ii)* the ease of surface functionalization with organic and biological molecules, and *iii)* the multitude of optical properties related to surface plasmons. In particular, Au NPs have a large number of easily polarizable conduction electrons, which is a general prerequisite for the preferential interaction with electromagnetic fields and for the generation of nonlinear optical phenomena.[4] In fact, compared to other organic and inorganic chromophores, Au NPs with size above 2 nm have larger extinction cross section, possibility to reach 100% of light-to-heat conversion efficiency, high photostability, and ability to amplify the electromagnetic field at nanometric distance from the metal surface, as discussed in the following sections.

The characteristic bright red colour of spherical Au NPs attracted the interest of manufacturers since ancient times,[20] and Au NPs or their nanoalloys can be found in ornamental cups such as the Lycurgus cup (ca. 4th century),[21, 22] red ruby glasses coloured with the “purple of Cassius” (Middle Ages)[23, 24] and luster plates (15th-16th century).[20] One of the oldest sample is represented by a gold plated Egyptian ivory dated back to 8th century BC, where Au NPs accidentally formed a purple staining by diffusion of gold from a thin foil into the porous ivory substrate (Figure 1A).[25] Indeed, this type of applications lasts even today.[26]

The first scientist that related the optical properties of Au NPs to their small size was Michael Faraday, which in 1852 gave a lecture at the Royal Institute in London entitled “Experimental Relations of Gold (and Other Metals) to Light”.[27] In his reports, Faraday described the Au colloid solutions as “a beautiful ruby fluid”, and attributed the effect to “a mere variation in the size of particles”. Later, Faraday’s study inspired the theoretical work of Gustav Mie in early 1900s, still valid until our days as described in section 3.[28]

In this review, we summarize the main concepts behind surface plasmon resonance in Au NPs, and the most relevant applications, with special attention to cutting edge topics. The review is divided in six main sections that are: 1. Fundamentals of SPR in Au NPs; 2. Factors influencing plasmon resonance; 3. Modelling the SPR of Au NPs; 4. Applications related to SPR optical extinction; 5. Applications related to local field enhancement; 6. Other applications and advanced phenomena. Note that this manuscript is not intended as a comprehensive review of the subject, but rather as a selection of helpful insights chosen from the literature.

1. Fundamentals of SPR in Au NPs.

1.1 Plasmons, localized plasmons and plasmonic quality factor.

"Plasmons" are collective oscillations of free electrons in metals.[15, 29] Since these oscillations occur at a well defined frequency, a "plasmon" is classified as a bosonic quasiparticle excitation and corresponds to a quantum of plasma oscillation (thus the -on suffix).[15, 29, 30] According to the Fermi liquid model, plasmons can be described as a negatively charged electron cloud coherently displaced from its equilibrium position around a lattice made of positively charged ions, in analogy to a real plasma (Figure 2A).[15, 29]

Excitation of plasmons by the electric field of electromagnetic radiation is not allowed in bulk matter, i.e. below metal skin depth, where plasmon and photon energy dispersion curves never cross each other.[15, 30] On the other hand, the presence of a surface in real materials allows the existence of specific plasmon modes which can be excited by the external electric field of the electromagnetic radiation,[15, 30] causing displacements of the electron gas with respect to their equilibrium position around positively charged ions. The light with a high angle of incidence (i.e., with wave vector nearly parallel to the surface, see Figure 2A) couples most efficiently with the free electron gas, such as in the attenuated total reflection (Kretschmann or Otto) configuration.[15] In fact, this type of oscillations are called propagating surface plasmon polaritons (PSPP), in analogy with propagating phonon-polaritons.[15, 29]

In case of metallic nanoparticles, i.e. with size comparable to the metal skin depth, the electric field of incident light can penetrate the metal and polarize the conduction electrons (Figure 2B).[15, 30] Contrary to PSPP, plasmons in NPs with size much smaller than photon wavelength are non-propagating excitations, called localized surface plasmons (LSPs), because the resulting plasmon oscillation is distributed over the whole particle volume.[15, 30] Such a coherent displacement of electrons from the positively charged lattice generates a restoring force that pulls the polarized electrons back to the lattice, i.e. the NPs act much like a "nanoantenna".[31] Hence, the plasmon in a NP can be considered as a mass-spring harmonic oscillator driven by the energy resonant light wave, where the electron cloud oscillates like a simple dipole in parallel direction to the electric field of the electromagnetic radiation (Figure 2C).[31-33] Only light with frequency in resonance with the oscillation is able to excite the LSP.[15] The simple mass-on-a-spring damped oscillator model, where the mass is represented by the electron density and the spring constant is set by the Coulomb restoring force between electrons and lattice atoms, has been utilized several times to gain conceptual and physical (semi-quantitative) understanding of plasmonic systems.[31-33] For instance, in case of a spherical Au NP with size much smaller than the wavelength of light (quasistatic approximation), the distortion of the electron cloud in response to the electric field can be expressed by the metal polarisability:[30, 34]

$$\alpha(\lambda) = 3\varepsilon_m(\lambda) V_{NP} \frac{\varepsilon(\lambda) - \varepsilon_m(\lambda)}{\varepsilon(\lambda) + \chi\varepsilon_m(\lambda)} \tag{1}$$

where λ is the light wavelength, ε_m the dielectric constant of the non absorbing ($Im[\varepsilon_m]=0$) surrounding medium, V_{NP} the NPs volume, χ is a geometrical factor (χ=2 in a sphere), and $\varepsilon(\omega)$ is the frequency (ω) dependent complex dielectric function (Figure 3A-B):[35, 36]

$$\varepsilon(\omega) = Re[\varepsilon(\omega)] + i\, Im[\varepsilon(\omega)] \tag{2}$$

From eq. (1) one can arrive to the quasistatic expression of the extinction cross section (σ_{Ext}) in a spherical Au NP:[15, 37]

$$\sigma_{Ext} = \frac{18\pi[\varepsilon_m(\lambda)]^{3/2}}{\lambda} V_{NP} \frac{Im[\varepsilon(\lambda)]}{[Re[\varepsilon] + 2\varepsilon_m(\lambda)]^2 + Im[\varepsilon(\lambda)]^2} \tag{3}$$

From eq. (3) it is evident that:

(i) the plasmonic properties of any material are defined by its $\varepsilon(\omega)$;

(ii) σ_{ext} scales with particles volume;

(iii) σ_{ext} is maximum when the denominator is minimized, namely the LSP is excited at the frequency where:[30, 34]

$$Re[\varepsilon_{NP}(\omega)] \approx -\chi\varepsilon_m(\omega) \tag{4}$$

Eq. (4), also called the Fröhlich condition, defines the localized surface plasmon resonance (SPR) condition. Clearly the frequency of the SPR is tuneable by changing the $\varepsilon_m(\omega)$ of the surrounding medium, but it is strongly affected also by NPs size, shape and composition,[38, 39] as discussed in section 2.

Obviously, the persistence of plasmonic oscillation is limited in time by loss.[36, 40] While $Re[\varepsilon_i]$ describes the resonance frequency of a plasmonic system, $Im[\varepsilon_i]$ describes its losses. Losses are due to many processes, including radiative damping, electron gas confinement, structural imperfections, and metal heating losses (see paragraph 1.2).[36, 40] However, in most plasmonic systems, such as in Au NPs, the main source of loss are intraband transitions, i.e. single particle excitations from the occupied 5d valence band to the unoccupied levels of the 6s-6p conduction band of gold (see paragraph 1.2).[36, 40] This is because the formation of electron-hole couples simultaneously to LSP excitation dramatically increases the electron-electron scattering rate (see paragraph 1.2).

From the plot of $Im[\varepsilon_i]$ in Figure 3B one can see that Au suffers higher losses than Ag in the visible range.[36, 40] The reason is that the band edge frequency in Ag, i.e. the frequency at which interband transitions become allowed, is above the SPR frequency, so that LSP cannot decay into electron–hole pairs, whereas in Au nanospheres there is an overlap resulting in a reduced plasmon intensity.[36, 40] However, Au is often preferred to Ag for the higher biocompatibility and chemical stability, in particular against surface oxidation and dissolution in liquid environments over times.[18, 19]

The considerations about SPR intensity can be quantified by the plasmonic quality factor Q_{SPR}. Every specific NP geometry has a different expression for the quality factor, but in the limit of low loss and in the quasistatic regime (i.e. when the NPs are much smaller than the wavelength of light, which means almost homogeneous electric field distribution along the whole NPs volume), Q_{LSP} can be written as:

$$Q_{SPR}(\omega) = -\frac{Re[\varepsilon_{Au}(\omega)]}{Im[\varepsilon_{Au}(\omega)]} \tag{5}$$

According to eq. (5), for a given plasmon resonance frequency ω_{SPR}, the LSP quality factor is determined only by the complex dielectric function of the material, independent of the NP shape or the dielectric environment (Figure 3C).[36, 40] However, we will see in section 2 that it is possible to shift the LSP frequency in the region of highest Q_{SPR} by acting on several factors.

The LSP is associated to two important physical effects:[15, 41]

(i) the Au NP optical extinction has a maximum at the SPR frequency, which occurs at visible-near infrared wavelengths and with extinction cross section (σ_{Ext}) that can be much larger than their geometrical size;

(ii) Au NPs behave as nanolenses, i.e. the electromagnetic field near particle’s surface (either inside and outside the NP) is greatly enhanced, and rapidly falls off with distance. This overcomes the resolution limit of ordinary far-field optics, allowing light localization on nanometric or subnanometric scale.

These two effects are at the core of SPR applications described in sections 4-5 and 6. A higher Q_{SPR} factor representing a sharper resonance is often desirable as it leads to higher optical extinction and stronger local-field enhancement.

The simplest way to probe the LSP is measuring the optical extinction of ensembles of Au NPs by optical absorption spectroscopy.[34, 42, 43] For instance, the optical extinction spectrum of a colloidal solution of spherical Au NPs is characterized by an SPR band in the proximity of 520 nm, partially superposed to the tail of interband transitions at shorter wavelengths (Figure 3D).[30, 43] However, the LSP in single Au NPs can be directly probed also by far field extinction microscopy (Figure 4A),[44, 45] electron energy loss spectroscopy (EELS, Figure 4B)[46-48] or cathodoluminescence (Figure 4B).[49, 50] In the last two cases, 3D mapping of the LSP over NPs volume has been also demonstrated (Figure 4C).[48, 49]

1.2 Dynamics of LSPR.

1.2.1 SPR bandwidth. The plasmon bandwidth of a single Au NP is associated to the dephasing time of the coherent electron oscillation, with larger bandwidth corresponding to a faster loss of coherence.[30, 51, 52] Typical electron dephasing times in Au NPs are of 2 - 50 fs, depending on particles structure and environment, and this value sets the SPR bandwidth.[30, 51, 52]

The total line width of the SPR band is contributed by a radiative term, producing elastically scattered radiation, proportional to the radiative decay rate Γ_r, and a non radiative term depending on electronic relaxation processes Γ_{nr}, essentially producing heat.[15, 30, 51]

Considering the LSP as an example of harmonic oscillator composed by a charge-on-a spring, the SPR bandwidth is proportional to the total relaxation rate Γ, that can be expressed as:[33]

$$\Gamma = \Gamma_{nr} + \omega^2 \Gamma_r \tag{6}$$

where one can see that the Γ_r term is multiplied for a ω^2 factor, meaning that its importance rapidly decreases while lowering the SPR frequency.

1.2.2 Radiative decay. The Γ_r term is associated with the far-field radiation emitted by accelerating and decelerating charged particles, and thus it is fully accounted by the classic electrodynamics theory (such as the Mie model, see paragraph 3.2.1). Since classical laws of electrodynamics necessitate that an accelerating charge release energy in the form of radiation, conservation of energy implies that this charge must consequently lose kinetic energy, and is referred to as the Abraham-Lorentz force or the radiation reaction force.[33, 53] The relative weight between the two contributions in eq. (6) sets the proportion between light scattering versus light absorption (intended as transfer of photon energy to the NPs lattice, see paragraph 2.2.1). The relative weight of the two processes changes with NPs size, and on a lower extent also with NPs shape and environment. The radiative decay contribution becomes more important for increasing NPs size, but for 20 nm Au NPs it accounts for only few percents of the total damping rate.[45, 54, 55]

1.2.3 Non radiative decay. Several groups extensively studied the non radiative SPR relaxation rate with ultrafast spectroscopy.[51, 52, 56, 57] There are several dephasing mechanisms contributing to Γ_{nr}, and the principal ones are the electron – electron scattering ($1/t_{e-e}$), electron-phonon scattering ($1/t_{e-ph}$), electron – defects scattering ($1/t_{e-d}$), and additional damping effects due to surface effects ($1/t_s$), discussed in paragraphs 2.1 and 2.2).[51, 52] According to Matthiessen law, all these contributions can be expressed as:[51, 52]

$$\Gamma_{nr} = \frac{1}{t_{e-e}} + \frac{1}{t_{e-ph}} + \frac{1}{t_{e-d}} + \frac{1}{t_s} \qquad (7)$$

When a single Au NP is polycrystalline or highly defective, the dumping frequency also increases producing a larger SPR band.[58]

1.2.4 Fate of the SPR. All the above scattering processes can be viewed as a unique Landau damping mechanism, with damping rate depending on the phenomena listed in eq. (7). In Landau damping, plasmon energy is transferred into a lower energy single or multiple electron–hole pair excitations on a timescale of 1 – 100 fs.[59, 60] The electron-hole pairs excitation can be either intraband or interband (see Figure 5A).[60-62]

Due to the energy overlap of plasmon absorption and the edge of interband transitions in spherical Au NPs, interband excitation corresponding to the excitation of one electron in the conduction band and creation of an hole in the lower lying *d* band has a remarkable contribution to the electron-electron relaxation rate,[62] ultimately explaining why Q_{LSP} in Au is lower than in Ag.[36, 40, 63]

After electron-hole formation by Landau damping, electron – electron scattering (such as Auger transitions) takes place on a time scale of ~500 fs, driving to electron thermalization (Figure 5).[51, 52, 60, 62] This can be seen as the relaxation of the interband electron-hole pairs and/or higher energy interband pairs, by formation of several lower energy intraband electron-hole pairs in the conduction band.[51, 60] In this way, electron energies rearrange from a non equilibrium to the quasi equilibrium Fermi – Dirac distribution corresponding to the system thermal energy plus the absorbed photon energy.[51] This means that for times ≤500 fs after plasmon excitation, the electronic temperature is still higher than the lattice temperature.[51, 52]

In 1 – 5 ps, electron – phonon scattering drives to the thermalization of the electronic bath with the lattice.[51, 52] The last process involves phonon – phonon interactions between the lattice and the surrounding medium, with a time scale of hundreds of picoseconds up to nanoseconds.[51, 52]

In general, one should consider that all these relaxation mechanisms are partially overlapping in time. Besides, the precise time scale depends on the intensity of the light beam and on the external temperature, for instance because all decay rates are temperature dependent.[55]

The relaxation processes following plasmon loss of coherence can be modelled according to the two temperature model (TTM), in which the electrons and the lattice are treated as two coupled subsystems with different initial temperature after LSP excitation, and with different heat capacities.[51]

1.2.5 Photoluminescence associated to SPR. Photoluminescence efficiency of LSP (i.e. inelastic radiative relaxation, measured as the number of emitted photons over the number of extinct photons) is typically below 10^{-3}-10^{-5}. This is expected for metals, where the non radiative decay processes are very fast. Indeed, the entity of intrinsic photoluminescence due to SPR decay in Au NPs is debated, as it implies the radiative recombination of electron – hole couples.[15, 51] However, the photoluminescence efficiency in Au NPs is 10^5 - 10^7 times higher than in bulk Au, and in Au nanorods (NR) it is ~10^2 times higher than in Au nanospheres.[51, 63] This is often reported as the "lightning rod" effect, which consists in the enhanced radiative recombination efficiency of *sp* bands electrons with *d* band holes thanks to the local electric field associated to the LSP (see section 5).[51] However, the strongest contribution to the photoluminescence measured so far in Au NPs is very often associated to the electronic states of surface impurities.[64]

2. Factors influencing plasmon resonance

2.1 Dielectric and physical-chemical environment.

2.1.1 Non-absorbing dielectric environment. Following eq. (4), a change in ε_m corresponds to a change in the SPR frequency of Au NPs in a non-absorbing matrix ($\varepsilon_m = Re[\varepsilon_m]$).[15] Since $Re[\varepsilon_{Au}]$ decreases versus wavelength (see Figure 3A), eq. (4) implies that the SPR is red shifted for increasing ε_m (i.e. going from water to glass) and blue shifted for decreasing ε_m (i.e. going from water to air).[34] The SPR red shift is associated to the increase of the Au NPs extinction cross section, because Q_{SPR} increases with wavelength in the 500 - 700 nm range (see Figure 6A).[36, 40]

Due to the nanometric size of NPs, i.e. to the large fraction of surface atoms over total, the SPR position is very sensitive to the environment dielectric properties, such as changes in liquid or gas density, formation of organic shells such as those of stabilizing ligands, and in general to any surface adsorption of chemical compounds.[34, 43] This finds important applications in sensing as described in paragraph 4.1.

2.1.2 Absorbing dielectric environment. The integration of Au NPs with absorbing materials, such as graphene, semiconductor quantum dots or metal oxides, is frequently sought for the realization of hybrid multifunctional materials. In this case, the SPR will experience both the spectral shift due to the change in the real part of ε_m, as described above, and the shielding effect due to light absorption associated to the imaginary part of ε_m. Depending on the geometry of the absorbing materials (size, thickness, shape, etc.) and the coupling distance, the effect on the SPR can go from plasmon enhancement to complete quenching.[65, 66] For instance, the SPR of Au NPs embedded in several graphene layers is quenched up to reaching a lower extinction than the sum of the two isolated components (i.e. an "enhanced transparency" effect).[65] This effect is distance dependent: it is stronger below 1 nm, and lost when graphene is at a distance of about 5 nm from the Au NP.[65] This result is non-trivial considering that graphene layers are not transparent and contribute to the overall absorption cross section of the nanohybrid (see Figure 6B). Therefore, coupling plasmonic NPs with graphene multilayers is a way to dramatically change the optical density in the SPR region without acting directly or irreversibly on the metal nanostructure.

2.1.3 Surface chemical interactions. Chemical modifications on Au NPs surface, such as reaction with thiolated ligands, physisorption of chemicals such as alkylamines or citrate, or adsorption of reactive gas species such as H_2S, change the LSP properties in three ways (Figure 6C-F):

i) Increase the pure dephasing rate Γ_{nr} (see eq. (7)) by introducing new electron relaxation pathways.[51] In particular, several models have been developed in which the LUMO of adsorbates couples with the free electron population via reversible charge transfer processes, contributing to a faster coherence loss.[30, 67, 68] Later, density functional theory (DFT) calculations demonstrated that electronic density of states near the Fermi level of Au NPs changes in presence of adsorbates,[57, 69] and with stronger effects going from amines to thiolated ligands (Figure 6C).[57] This effect is known as chemical interface damping (CID).[30, 57, 70]

ii) Formation of a shell of non metallic Au atoms,[71, 72] i.e. change in the bond order,[69] with overall reduction of the effective size of the plasmonic metal core in the NPs (for size effects see paragraph 2.2).[73] For instance, in the case of thiolated monolayer protected Au cluster such as $Au_{314}(SH)_{96}$, each SH ligand withdraws one electron out from the Au(6sp) subsystem and the effective "valence" electrons are only 218.[73]

iii) Variation of the dielectric environment of the Au NPs, with a consequent variation of the real part of the "effective" matrix optical constant, with the effects described in section 2.1.1.[34]

The relevance of the chemical effects strongly depends on NPs size, shape and on the type of reagent. In case of CID, different adsorbates have different LUMO energy and localization, then couple in a different way with the metal conduction band and originate different SPR widths.[57] In monolayer protected Au NPs, density and molecular weight of the ligands are also important.[70] For instance, coating of small (i.e. < 10 nm) Au NPs with a dense monolayer of short chain thiolated ligands is typically associated to SPR damping. It is worth noting that a 4 nm Au NPs is composed by ~2000 atoms, of which the 24% is located on the surface. In case of large Au NPs (i.e. > 10 nm) and long chain ligands (i.e. MW > 1000 Da), only SPR red shift is observed as a consequence of the increase in the real part of the "effective" optical constant of NPs environment.[30, 43, 71, 72]

2.1.4 Temperature. Temperature (*T*) increase is associated to SPR red shift and broadening (that means bleaching at SPR maximum).[55, 56, 74] For NPs embedded in solid matrixes or dispersed in liquids, these effects are much less relevant than modifications of the dielectric environment or structural NPs modifications at high T, that are induced by local plasmon heating (see paragraph 4.3). In spherical Au NPs embedded in silica matrix, this change is ca. +0.3% in red shift and ca. +5% in band broadening every 100 K of temperature increase.[74] However, in open air configurations, the actual T of NPs is important for appropriate modelling of experimental results.[55]

The red shift is due to thermal dilatation of the lattice, that means a decrease of electron density (n_e, see Figure 6G).[75, 76] In fact, in noble metals the LSP frequency (ω_{LSP}) is proportional to the bulk plasma frequency (ω_p),[77] and ω_p is proportional to $n_e^{1/2}$ according to its expression in free electron metals:[30, 56, 74]

$$\omega_p(T) = \sqrt{\frac{e^2 n_e(T)}{m_{eff}\,\varepsilon_0}} \tag{8}$$

where e is the electron charge, m_{eff} the electron effective mass and ε_0 the vacuum permittivity.

SPR broadening means that $\Gamma_{nr}=\Gamma_{nr}(T)$, i.e that the electron distribution near the Fermi level and the associated increased electron scattering rate increase with T, ultimately leading to an increase in $Im[\varepsilon_{Au}]$ and a consequent decrease of Q_{LSP}.[55, 74] On the other hand, Q_{LSP} can be slightly improved by decreasing T.[76]

The effect of temperature on the SPR depends also on the heating modality.[55] In case of transient heating such as during pump-probe ultrafast experiments, the electron – electron scattering frequency is the main parameter affected by T, because the tail of the Fermi-Dirac electron distribution increases with temperature, and $1/t_{ee}$ depends on the square of the difference between the free electron energy E and the Fermi energy E_F:[51, 56]

$$\frac{1}{t_{ee}} \propto \left(E - E_F\right)^2 \tag{9}$$

Transient SPR extinction spectra show the bleaching and the broadening of the plasmon band already in the first picoseconds, as a consequence of the higher electronic temperature and higher electron-electron scattering rate.[51, 56]

In steady state heating conditions, the change in the electron-phonon scattering rate is the dominating contribution, while the electron-electron scattering rate remain almost constant.[55, 74, 76]

2.1.5 Pressure. Pressure up to 1.2 GPa has no appreciable effects of on the SPR of Au NPs, [78] while for larger values plastic deformation of nanoparticles occurs.[79]

2.2 Size.

2.2.1 Absorption and scattering cross section. The SPR band detected in the optical extinction spectra of Au NPs dispersions is originated by the sum of scattered and absorbed photons, with a proportion strongly dependent on particles size.[15, 30, 37] We can express the extinction cross section of an Au NP as the sum of the absorption (σ_{Abs}) and scattering (σ_{Sca}) terms: [15, 30, 37]

$$\sigma_{Ext} = \sigma_{Abs} + \sigma_{Sca} \tag{10}$$

Assuming an homogeneous sample composed of *N* identical Au NPs in a volume *V*, the extinction cross section is related to the measured transmittance (*Tras*) and absorbance (*Abs*) by:[43]

$$Tras(\omega) = \frac{I(\omega)}{I_0(\omega)} = exp\left[-l\frac{N}{V}\sigma_{ext}(\omega)\right] = exp\left[-l\frac{N}{V}(\sigma_{Abs}(\omega) + \sigma_{Sca}(\omega))\right] \tag{11}$$

$$Abs(\omega) = -log_{10}\left[exp\left[-l\frac{N}{V}\sigma_{ext}(\omega)\right]\right] = -log_{10}\left[exp\left[-l\frac{N}{V}(\sigma_{Abs}(\omega) + \sigma_{Sca}(\omega))\right]\right] \tag{12}$$

where I_0 and I are, respectively, the incident and transmitted light intensity, and l is the optical path within the sample. Since *Tras* exponentially depends on σ_{Ext}, even a moderate increase in the cross section leads to a huge enhancement of light extinction.

For Au NPs with size $d<<\lambda$, where λ is the wavelength of the electromagnetic radiation, the absorption dominates over scattering.[15, 30] However, for NPs smaller than light wavelength, scattering and absorption scale respectively with the 6th and the 3rd power of particle's size,[15, 37] therefore the two effects become comparable for Au NPs of about 50 nm, and scattering prevails above 70 – 100 nm (see Figure 7A).[80]

The size dependence of σ_{Abs} and σ_{Sca} is relevant for applications related to optical extinction and near field enhancement, described in sections 4-5. In fact, light scattering is an elastic process consisting in the modification of photon propagation direction, therefore NPs with a large σ_{Sca} are preferentially exploited for biolabelling and sensing up to single particle sensitivity (see paragraph 4.1), as well as for nanolensing and enhancement of nonlinear optical properties in nearby objects (see paragraphs 5-6). Instead, light absorption consists in the transfer of photon energy to the plasmonic nanostructure, where it is rapidly converted to heat.[35, 81-83]

2.2.2 Extrinsic size effects. The extrinsic size effect is a retardation effect due to the excitation of multipolar plasmon modes when NP size increases with respect to the resonant electromagnetic wavelength,[30] i.e. when the size parameter x is close to 1, where x is defined as:[37, 84]

$$x = \pi d/\lambda \tag{13}$$

When Au NP size is small compared to the light wavelength (quasistatic regime, $x<<1$), the electric field distribution along the particle is essentially uniform, electron cloud polarization is coherent in each point of the metal and dipolar plasmon oscillations are excited.[15, 30] Conversely, when Au NP size is comparable or larger to the resonant electromagnetic wavelength, the electric field distribution along the particle is non uniform, electron cloud polarization is no more coherent in each point of the metal and multipolar plasmon oscillations are excited.[15, 30] This is a bare electromagnetic phenomenon accounted from the electrodynamic theory such as the Mie model, contrary to the intrinsic size effect described in next section.[30]

The extrinsic size effect appears in the optical absorption spectrum as broadening and red shift of the SPR for increasing Au NP size.[15, 30] The multipolar excitations are dominant for Au NPs larger than 60 nm, whereas dipolar oscillations dominates for particles of 25 nm or smaller.[30, 80] In Au nanospheres, extrinsic size effects allows tuning of SPR wavelength over 60 nm by varying particle size between 10 and 100 nm.[80]

2.2.3 Intrinsic size effects. Intrinsic size effects are due to the modification of the metal optical constant when Au NPs size is below 30nm.[30] The optical constant changes because of additional contributions to the free electron relaxation rate when the nanoparticle size is reduced.[30] In particular, the free electron scattering at particle surface is no more negligible when the conduction electrons mean free path (~ 30 nm for Au) becomes comparable to particle size.[30] Therefore, the intrinsic size effect is responsible for the increase of Γ_{nr} and $Im[\varepsilon_{Au}]$, thus the decrease of Q_{LSP}, and it appears as a damping of the SPR band for decreasing particle size (Figure 7C).[43, 85, 86] SPR quenching is almost complete in Au NPs smaller than about 2 nm, when this effect encompasses all the other scattering mechanisms including electron–electron, electron–phonon and defect interactions.[47]

The Au optical constant can be corrected for intrinsic size effects using a size-dependent relaxation frequency:[30, 43]

$$\Gamma_{nr}\left(L_{eff}\right)=\Gamma_{nr}^{bulk}+A\frac{v_F}{L_{eff}} \tag{14}$$

where L_{eff} is the effective NPs size, Γ_{nr}^{bulk} is the bulk Au value, v_F is the Fermi speed, and A is an empirical parameter. In NPs with arbitrary shape, L_{eff} is often expressed as the radius of a sphere with the same volume (V_{NP}):[87, 88]

$$L_{eff}=\left(\frac{3V_{NP}}{4\pi}\right)^{1/3} \tag{15}$$

However, another expression for L_{eff} has been proposed on the basis of a geometrical probability approach for electron scattering at the surface of NPs with arbitrary convex shape: [85]

$$L_{eff}=\frac{4V_{NP}}{S_{NP}} \tag{16}$$

where S_{NP} is the surface area of the NPs.

A is an empirical parameter indispensable to account for all factors affecting the electron scattering at NPs surface, such as the CID effect due to strongly interacting ligands, or other types of surface defectivity.[30, 43, 71] According to literaure, A spans the 0.1 – 2 range,[43, 47, 89] and for a specific system can be obtained from the comparison of optical extinction spectra with electron microscopy size analysis.[43, 47] This simple calibration procedure allows the evaluation of spherical Au NPs size and concentration based on the fitting of the optical extinction spectra with the Mie model (see paragraph 3.2.1), with an average error of 6% (Figure 6D).[43]

To introduce the size correction into the bulk Au optical constant, one must refer to the relatively simple Drude-Lorentz model for optical permittivity,[30, 43, 87] as described in paragraph S1 of S.I. This model provides high versatility in the correction of Au optical constant also as a function of other factors such as temperature.[55]

2.2.4 Quantum size effects on the SPR. Quantum effects influence the LSP already for NPs smaller than ~10 nm,[47] although they become more relevant for a size smaller than ~1.5 – 2 nm (depending on surface coating), when the SPR is in the regime of strong quenching due to the surface damping effects.[73] This happens because of the optical constant modification when approaching the quantum regime, known as “non local” effects (see paragraph 3.1). Indeed, for NPs with size between 2 and 10 nm, lattice contraction occurs, with consequent increase in electron density, that pushes the resonance towards higher frequencies.[47] For instance, accurate EELS measurement in “pure” (i.e. not passivated by ligands or chemicals) metal NPs with diameter decreasing from 20 to 2 nm evidenced SPR blue shift of ~0.5 eV.[47] The blue shift, not predicted by classical models, is well reproduced with quantum mechanical models accounting for the quantum confinement of the free electron gas by the NPs surface.[47] This surface confinement effect is appreciable in naked metal NPs, while CID dominates in ligand passivated particles.[47, 90]

In Au NPs with size below 2 nm, the Au(6sp) states are delocalized over the whole particle in analogy to the free electron gas in bulk gold metal.[73, 90-93] However, the quantum confinement effects in NPs create discrete energy bands with specific symmetries, and these bands are well-described by the model of “superatom”.[90] In fact, monolayer protected 1 - 2 nm Au NPs are known to have molecular-like electronic structure, and they represent the link between “molecular” gold clusters and “metal” gold NPs.[73, 90-93] For instance, a well defined SPR is predicted in a monolayer protected cluster with a 2.0 nm metal core (314 Au atoms), while in a smaller cluster with 1.5 nm gold core (144 Au atoms), the SPR is quenched and confined in the metal core (Figure 7E).[73] These results suggest a threshold size between 1.5 and 2 nm for the emergence of SPR in Au NPs.[94]

The discrimination of SPR in these systems is indeed difficult.[95, 96] It was recently suggested that the plasmonic state consists of a linear combination of many singly excited configurations that contribute additively to the transition dipole moment, whereas other excited states show significant cancellation among the configurations leading to weak absorption.[96] Recently, the “plasmonicity index” has been proposed as a mean to quantify the plasmonic character of optical excitations in small metal NPs.[95] The plasmonicity index is based on the concept that plasmonic excitations should locally enhance the applied electromagnetic radiation, and is extracted from theoretical atomistic models for optical extinction properties in metal clusters.[95]

2.3 Assembly.

Plasmons on distinct nanoparticles can reciprocally influence each other, depending on particles distance, geometry and relative light polarization, with generation of "hybrid" plasmon modes.[97, 98]

The simplest case of assembly is the nanosphere dimer in the quasistatic regime, where end-to-tail coupling of dipolar plasmon modes is possible, with consequent decrease of the overall SPR frequency (red shift) for excitation along the dimer axis.[97] Conversely, for electric field perpendicular to dimer axis, the dipolar plasmon modes couple head-to-head, with a slight blue shift of the SPR.[97, 98] In case of dimer size comparable to light wavelength, quadrupolar or higher order plasmon modes are possible, with different effects on the SPR frequency.[97, 98]

In more complex systems, the hybrid plasmon modes can be analyzed applying group theory to LSP of individual NPs.[97] For instance, according to group theory, a trimer of NPs arranged in the form of an equilateral triangle (point group D3h) supports nine dipolar plasmon modes.[97] Three of these modes can be classified as "bonding" modes (see the hybridization theory described in paragraph 3.2.2f), and three are non-bonding (or "dark"), with energies lower and higher than that of an individual particle, respectively. The mode with lowest energy has a ring-like arrangement of dipoles, meaning that it is dark for excitation with linearly polarized light, but can be excited with radially polarized light.[97, 99]

On the other hand, by referring to the analogy between LSP and a mass-spring harmonic oscillator, LSP hybridization can be seen as a serial coupling of two or more springs.[32, 100, 101] Multipolar LSP can be modelled as springs oriented along the interaction direction set by charge oscillation in the NPs.[101, 102]

The red shift due to SPR hybridization in Au NPs dimers decays near-exponentially with the interparticle gap over a distance that is roughly 0.2 times the particle size, independent of the nanoparticle size, shape, material, and the medium dielectric constant.[103, 104] This universal decaying behaviour of the SPR in nanoparticle pairs originates from the distance decay of the interparticle local field that couples the particles together.[103, 104] When nanoparticles are in touch through a conductive junction, the hybridization effects disappear and the SPR abruptly blue shifts to that of a particle with necklace shape (Figure 8A).[46, 104]

This behaviour is rather general and a "plasmon ruler" equation was proposed to estimate with good accuracy the distance between dimers from the measured fractional SPR shift:[103]

$$\frac{\Delta\lambda_{SPR}}{\lambda_{SPR}} = K\,exp\left(\frac{r/d}{s}\right) \tag{17}$$

where K is a constant depending on particles geometry and dielectric environment, r is the edge to edge NPs distance, d is particles diameter and s is the decay length close to 0.2 and almost independent on particles type, shape and dielectric environment. The same expression can be used to estimate the position of core@shell SPR for different core to shell ratios just replacing r with the shell thickness and d with the core radius.[105] In fact, plasmon modes couple in any metal structure, regardless if they are spheres, concentric metal layers or mixed shapes.[98, 103, 105]

Agglomerates with fractal structure made by tens of particles have two main bands, one close to the original spheres position and another red shifted.[98, 106, 107] Both are sensibly broader than single particle SPR and are originated by the convolution of a multitude of plasmon modes supported in each part of the fractal aggregate.[106] In aggregates with fractal number sensibly lower than 3 (meaning low density and highly ramified structure), the largest contributions come from pseudo-linear NPs assemblies aligned to the light polarization direction.[108] When particles in the aggregates are several hundreds, only one very broad red shifted band is present.[98, 106]

Assembly in disordered superclusters is exploited for sensing or for photothermal effects (section 4), and, assembly of plasmonic NPs is crucial also for all the effects related to local field enhancement, as discussed in section 5.

2.3.1 Fano resonances. For specific NPs assembly geometries, typically associated to well defined NPs disposition and homogeneous nanometric gaps between particles, the mutual interaction between plasmon oscillations can originate constructive and destructive interference phenomena yielding to asymmetric SPR band shapes and sharp dips or spikes in the optical extinction spectrum, known as Fano resonances (Figure 8B).[16, 109] Also in this case, the analogy between LSP and an spring-mass harmonic oscillator allows the convenient modelling of Fano resonances.[16] As Fano resonances arise from the interference between two or more oscillators, they are sensitive to changes in geometry or local environment, with the effect that small perturbations can induce dramatic resonance or lineshape shifts up to 600 nm per matrix refractive-index unit.[16] Besides, at those frequencies where constructive interference occurs, optical extinction and local field enhancement are larger.[16]

2.3.2 Magnetic plasmonic resonances. In principle, both the electric and magnetic components of light can excite LSP modes in Au NPs.[110] Charge currents associated to electric SPR have a dipolar character (i.e. the NPs behave as an electric dipole), while MPR are associated to a circulating displacement current and hence the NPs behave as a magnetic dipole (Figure 8C).[111, 112] The MPR phenomenon is also described as optical magnetism or artificial magnetism.[110, 112]

In isolated NPs, MPR are weak or located outside the range of optical frequencies.[111, 113] However, in assemblies of NPs, MPR at optical frequencies can be intense and even dominate the extinction spectrum.[111-113] This occurs especially when non-touching Au NPs are assembled in rings or shells (Figure 8C) .[111-113] For specific configurations, the mutual interaction between electric and magnetic LSP modes may also generate Fano resonances.[111, 113]

The symmetry of charge displacement in isolated or assembled Au NPs are accessible by the Mie theory and its generalizations (Section 3), providing a quantitative way for the identification of electric and magnetic LSP modes.[111, 112]

Interestingly, MPR are associated to the enhancement of the oscillating magnetic field, especially in case of magnetic Fano resonances, in analogy to the well known local electric field enhancement.[111, 113]

The main interest in MPR is due to their exploitability to obtain metamaterials with negative refractive indexes, because close to the MPR frequency both magnetic permeability and electric permittivity can become negative.[110] For this reason, the assemblies of NPs showing MPR are often defined “metamolecules” composed by “meta-atoms”.[113, 114]

2.4 Shape.

The width, position and number of SPRs are determined also by the shape of the Au NPs.[39] The recent advances in synthesis and characterization of plasmonic nanostructures made it possible to realize nanoparticles with many different shapes, such as nanoshells, nanowires, nanocubes, nanostars, nanotriangles, nanocones, just to mention a few of them (Figure 9).[38, 39, 115-121] Notable examples of this are the LSP resonances of core-shells and nanorods, that can be tuned away from the lossy interband transitions of gold, improving the SPR quality factor.[36, 40, 65, 80]

In general, NPs symmetry reduction is an effective method to modify the position, number and intensity of SPR.[39, 42, 87] A common feature of these new SPRs is that they are located at lower energy compared to the sphere. For instance, Au nanospheres with the size of 2–50 nm show only one plasmon band centered at about 520 nm, while two SPR bands appear when the symmetry is reduced from spherical to cylindrical, i.e. in Au nanorods.[122, 123] The first band, corresponding to the excitation along the minor axis, is slightly blue shifted with respect to the SPR in an equivalent sphere, while the second band, corresponding to the excitation along the major axis, is red shifted and more intense, since Q_{LSP} increase with wavelngth. By increasing the aspect ratio D of the nanorod (i.e. the main to minor axis ratio), the second SPR can be shifted from the visible to the near infrared (NIR) range.[122-124] The wavelength of the longitudinal plasmon absorption (λ_{SPR}^{L}) is almost linearly dependent on the aspect ratio and the matrix dielectric constant:[125]

$$\lambda_{SPR}^{L} = \left(K_1 D - K_2\right)\varepsilon_m + K_3 \qquad (18)$$

However, the aspect ratio alone does not uniquely determine the extinction spectrum of a nanorod even for a monodisperse sample of rods, and the optical properties are much different between ellipsoids and cylinders with hemispherical, hemiellipsoidal or flat ends.[123]

By referring to the analogy between LSP and a mechanical harmonic oscillator, NPs shape modification can be seen as a change in the elastic constant of the spring, with strongest restoring force belonging to nanospheres, and weakest force to nanorods with high aspect ratio.[31-33]

For specific geometries, such as concentric nanoshells with alternating layers of Au and dielectrics, also Fano resonances are observed because of mutual interaction of plasmon modes in distinct metal components of the composite NP.[16, 102]

In most Au nanostructures, especially when $x<1$, the absorption bandwidth is limited to a small portion of the visible-NIR range owing to the resonant nature of the plasmon excitation.[38, 39, 42] Recently, asymmetric networks of gold nanoparticles, also called nanocorals (NCs), have been proposed as an interesting system for obtaining versatile and multimodal plasmonic responses.[81, 126, 127] For instance, networks of partially fused Au NPs showed very low-energy surface plasmon modes capable of supporting long-range and spectrally tunable propagation in nanoscale waveguides.[126] These Au nanonetworks belong to the C1 point group, the one with the lowest symmetry for an isolated object; hence the number of allowed SPR is larger compared to nanoparticles with higher symmetry.[126] In fact, Au NCs dispersions exhibit flat broadband plasmon absorption ranging from the visible to the NIR and unitary light-to-heat conversion (Figure 9).[81]

2.5 Composition.

The plasmonic properties of any material, such as Q_{LSP} and SPR width, intensity and position, are fully described by its complex optical constant.[36] Therefore, any chemical modification to the Au lattice (such as doping or alloying) induces a remarkable change in ε and LSPs.[35, 36] This means that Au alloying and doping are other methods for tuning the optical response of plasmonic systems, in addition to the conventional modification of NPs size, shape, assembly and environment.[35, 36, 128]

However, composition has been seldom considered as a parameter for tuning the plasmonic response of Au NPs. This is often motivated by the general assumption that other metals cannot perform better than pure Au nanostructures, either in terms of plasmonic response, ease of synthesis, physical–chemical stability or biocompatibility.[35, 36, 40] The study of alloys is complicated also by the thermodynamic limitations to miscibility of Au with other metals, often yielding to phase segregated compounds.[36]

Indeed, there is a relatively low number of elements with appreciable plasmonic properties (mostly Au, Ag and Al).[36, 40, 129] Materials with partially occupied d states perform poorly as plasmonic materials due to the probability of low frequency interband transitions and consequent increase of the SPR relaxation frequency due to the enhanced electron-electron scattering rate, ultimately leading to larger $Im[\varepsilon]$ and lower Q_{LSP}.[36, 40] Additional contributions to $Im[\varepsilon]$ come from the larger probability of electron–electron and electron–defects scattering in doped crystals and disordered alloys.[36, 40, 128, 130, 131]

On the other hand, alloying is frequently desired for the combination of Au properties with that of the other elements, such as magnetism,[130, 132] catalytic activity or lower production costs.

Au alloys with Ag have been frequently studied, because of the ease of synthesis and of the superior plasmon properties of silver.[133-135] In fact, interband transitions in silver are at shorter wavelength than in gold, meaning that the alloy has larger $Re[\varepsilon]$ and smaller $Im[\varepsilon]$, leading to higher Q_{LSP}.[36, 87, 129] In Au-Ag NPs, the SPR frequency and width varies almost linearly from the elemental Ag value to the elemental Au value as the stoichiometry is varied.[133-135]

In Cu, the onset of interband transitions is shifted to the visible range, thus Au-Cu alloys have lower Q_{LSP}.[36] In fact, the metal with interband transitions at lower frequency dominates the plasmon response of the alloy. For a similar reason, Au alloys with Pt and Pd showed poor SPR.[136-138] Disordered Au alloys with Co and Ni also have low Q_{LSP} and depressed SPR, while SPR blue shift and moderate damping was observed in Au_3Zn NPs.[36, 129, 139] Extreme Q_{LSP} depression is calculated from thin film measurements of optical permittivity in Au-Si and Au-Sn alloys, due to the immiscibility of the constituents and consequent amorphous film structure, while for AuAl alloys the effect is similar but associated to SPR red shift.[36, 129, 140]

The case of Fe-doped Au alloy NPs was investigated in detail thanks to the ease of synthesis by laser ablation in liquid.[35, 128, 130] In these nanoalloys, SPR damping and blue shift of ~15 nm is observed after introduction of ~11at% of Fe (Figure 10A).[128, 130] Also the local field enhancement rapidly decreases of ~20 times while increasing the amount of iron in the Au lattice up to ~13at%.[128] Conversely, the absorption cross section of Au NPs with size above 70 nm is sensibly increased when iron is included in the lattice.[35] The increase of σ_{Abs} is size and shape dependent, with the higher increment up to 90–190% predicted in nanoshells with size above ~70 nm, that is the optimum size also for practical applications (Figure 10B).[35] The augmented plasmon absorption in iron-doped Au nanoalloys is prevalently observed in the red and near infrared (NIR) frequencies, which actually is the working window for most photothermal applications.[6, 141]

The change of σ_{Abs} originates from the modification of the optical constants of gold after doping with iron.[35] Doping Au with Fe introduces new single electron transitions, which are generated by electrons lying in the iron d-states below the Fermi surface of the metal.[142] In general, low-frequency interband transitions are observed when noble metals and transition metals with partially occupied d-states are alloyed together.[36] The effect is the decrease of the $Re[\varepsilon]$ and the increase of $Im[\varepsilon]$ compared to pure Au.[35] While this is detrimental for extinction and local field enhancement, absorption is set by the following expression:[40, 143, 144]

$$\sigma_{Abs} = \frac{k}{\varepsilon_0 E_0^2} \int_{NP} Im\left[\varepsilon_{NP}\right] \cdot E_{NP}^2 dV_{NP} \tag{19}$$

where k is the wavevector, E_0 is the modulus of the electric field of the incident light, measured in the medium surrounding the NP of volume V_{NP}, and E_{NP} is the modulus of the electric field inside the NP. On the one hand, σ_{Abs} is proportional to $Im[\varepsilon]$, which is augmented by iron doping. On the other hand, it depends on the integral of E_{NP}^2 over V_{NP}, that is maximized when Q_{LSP} is maximum, and it is size dependent. From the balance between these two factors, the σ_{Abs} in Au-Fe nanoalloys results larger than in pure Au NPs when particles size exceeds 70 – 100 nm.[35]

These findings are unexpected according to the common belief and previous experimental observations that alloys of Au with transition metals show a depressed plasmonic response,[36, 129] thus suggesting that the scarcely investigated field of plasmonic nanoalloys can be a source of new, yet unforeseen solutions for the improvement of plasmonic performance.[36]

An alternative case to alloys is that of nanograined materials. Plasmonic properties in heterostructures correspond to a linear combination of the properties of the constituent metals, weighted by their respective stoichiometries, with a larger damping contribution to account for scattering by grain boundaries.[36] However, pure nanograined NPs are quite rare, because doping and alloying during the mixing procedure at the nanoscale is highly probable.[145]

3. Modelling the SPR of Au NPs.

A full theoretical understanding of the optical behaviour of gold nanoparticles is fundamental to optimize their application and to account for the many different shapes and structures (see paragraph 2.4). This implies the need for accurate techniques capable of computing the optical properties of nonspherical or aggregated NPs.[146-148] To this aim several analytical and numerical methods have been proposed in the literature and actually there is no single universal method providing the best results for all nanostructure type and targeted physical phenomena. In particular, approximated models are often used to get an insight into the physics of the problem, such as in the case of the mass-spring model, but they may hide important effects and lack of quantitatively reliable results. In such situations, accurate computational approaches are required to get a good agreement with experiments and a correct understanding of the electromagnetic processes at the nanoscale.[146-148]

3.1 Optical constant

Appropriate modelling of LSP requires the knowledge of Au NPs optical constant.[146] Although corrections are often required for size effects, surface coating, temperature or compositional modifications, as discussed in section 2, the starting point is the optical constant of bulk gold, that is experimentally accessible with good precision. The most widely used values are those reported by Johnson and Christy,[149] or in the handbook edited by Palik,[150] and their values can be accessed also from on-line databases such as http://refractiveindex.info/.

However, some inconsistencies exist in the dielectric functions found in the literature, typically due to deviation from ideal flatness and density of bulk Au.[151, 152] Therefore, precise spectroscopic ellipsometry measurements have been recently repeated on samples with controlled surface roughness and density, and compared to literature values.[151, 152]

3.1.1 Non locality and quantum size effects.

The standard description of optical properties of Au NPs exploits a “local” bulk dielectric function, i.e. $\varepsilon(\omega)$ only depends on frequency but not on NPs size, shape and structure.[30] However, this approach fails for very small diameters.[47, 73, 153] Such an example of “non locality” of $\varepsilon(\omega)$ was already shown in paragraphs 2.2.3-4 concerning size effects. However, nonlocality has relevant implications also when metal nanoparticles are in close proximity,[154] irrespective of their size, and when their shape includes sharp features.[46, 146, 155-158] In these cases, an accurate description should also consider electron-electron repulsion due to Pauli exclusion and Coulomb repulsion, that manifest as a pressure in an electron gas resisting to the compression induced by the external electromagnetic field.[159] As a consequence, the “longitudinal” dielectric function becomes non local along the photon propagation direction, while the transverse dielectric function remains local and equal to the bulk dielectric function.[159] The main effect of the nonlocal response, thus, is that the electron gas cannot be squeezed into an infinitesimally small thickness on the particle surface, as proposed by a classical local electromagnetic treatment, but rather it spreads out by a minimun distance of the order of 0.25 nm, putting an upper limit to the field enhancement achievable by metallic nanostructures.[146]

To account for the electron pressure, a linearized hydrodynamical approach for the electron collective motion in the metal has been proposed.[159, 160] Such approach in a uniform medium predicts a spatially nonlocal longitudinal dielectric function (ε_L) depending on the modulus (k) of the propagation vector in addition to the frequency:[159]

$$\varepsilon_L(\omega,k) = \varepsilon_{Au} - \frac{\omega_p^2}{\omega^2 + i\gamma\omega - \beta^2 k^2} \tag{20}$$

where γ is the samping coefficient and β is the pressure coefficient proportional to the Fermi velocity:[161]

$$\beta = \sqrt{3/5}\, v_F \qquad (21).$$

A weakness of the hydrodynamical model is that it ignores the possible charge density spill-out outside the metal particle boundaries. This effect stems from the smooth transition of the electron density due to the finite length of the electron waves, generating a negative charge density outside the electronic body.[162] The charge density spill out is essential for incorporating quantum tunneling effects between the particles when their separation distance reaches the sub-nanometer scale.[46, 155]

To go beyond the hydrodynamical model into the quantum tunneling regime, a first-principles quantum treatment is required. The time-dependent density functional theory (TDDFT) appears as a good approach, describing the plasmonic optical response at the quantum level and taking account of non local effects.[157] The drawback is its computational complexity, so that it is indicated for particles containing only a few thousand electrons. This problem can be solved by using a classical local model capable of incorporating the quantum tunneling effects, the so-called Quantum-Corrected Model (QCM), which was recently implemented.[146, 163] The QCM can be included within any standard model for the description of SPR in Au NPs, and with excellent agreement to full quantum mechanical calculations, because the junction between two NPs is modelled as a fictitious material with dynamical conductivity adjusted to mimics the effects of electron tunneling.[158] Therefore the correction to the metal optical constant is actually demanded to the set up of an effective optical constant for the medium at the junction between NPs (see Figure 11). In case of curved surfaces such as a sphere dimer, this can be accounted for as a shell of fictitious material.[146, 158]

3.2 Analytical and numerical methods.

3.2.1 Mie theory. For homogeneous spherical particles embedded in a non absorbing medium, Mie theory provides the optical properties for any particle size and optical constant.[37] Indeed, the seminal paper by Gustav Mie deals exactly with colloidal Au NPs.[28] The approach is based on Maxwell equations and on the multipole expansion of the electromagnetic fields. The incident and the internal (within the particle) fields are expanded in multipole fields that are regular inside the particle, while the external scattered field is expanded in multipole fields that behave as outgoing spherical waves at infinity. By applying the boundary conditions across the surface of the particle, i.e., the requirement of continuity of the tangential components of the electric and magnetic fields, the unknown coefficients in the expansions of the internal and scattered fields are determined from the known expansion coefficients of the incident plane wave.[37, 147] This solution for spherical particles is sometimes referred to as the Lorenz-Mie theory since Lorenz also derived, independently, the solution in 1890. In the years the theory was extended to core-shell spheres,[164] and radially inhomogeneous spheres.[165] The analytical expression for the Mie model is fully reported in paragraph S2 of S.I.

An accurate solution is obtained when convergence of the multipole field expansion is carefully checked. When dealing with metallic nanoparticles, there is not a general formula to estimate the number of significant coefficients, but convergence is generally expected to be reached at higher multipole orders compared with dielectric particles of the same size.[162, 166] As particle size increases, higher order multipole modes appear and a description in terms of dipole contributions becomes inaccurate. However, for size below ~20 nm, i.e. in the quasistatic regime, the dipolar LSP dominates, and the Mie model can be reduced to the simple expression of eq. (3).[30, 34, 37]

3.2.2 Non-spherical shapes. In many situations of real interest, particles are far from exhibiting a spherical symmetry. For ellipsoids in the quasistatic regime, the Gans model still provides analytical solution to the problem (see paragraph S3 in S.I.). However, for more complex shapes and assembly of NPs, other models are required. Currently, the most commonly used numerical approaches for describing the optical response of non spherical gold - and more generally, metal - nanoparticles are the discrete dipole approximation (DDA), the finite difference time domain (FDTD) method, the finite elements method (FEM) and the boundary element method (BEM).[153, 167] Most of these models have been included in freely available codes (see Table 1).

Table 1. Summary of different computational methods for the SPR in Au NPs. Rectangular grids may cause computation inaccuracies in case of curved or highly dynamic surfaces.[7] A complete list of free codes can be found at http://www.scattport.org/

Method	**Type**	**Structure allowed**	**Grid type**	**Free code available**
Mie model	Analytical	Spheres (core-shells)	no grid	Mieplot SPRFit
DDA	Numerical (frequency domain)	Any	cubic	DDSCAT
FDTD	Numerical (time domain)	Any	rectangular	Time-domain codes
FEM	Numerical (frequency domain)	Any	triangular or tetrahedral	FEM codes
BEM	Numerical (frequency domain)	Any	Adaptive (only at interfaces)	MNPBEM
T-matrix	Analytical	Any (generally spheres, core-shells and their assemblies)	No grid	T-matrix codes

3.2.2a DDA. The DDA, also known as the coupled dipole method, was originally introduced by Purcell and Pennypacker for describing light scattering by interstellar dust grains, [168] and subsequently developed by Draine et al., which also created the popular DDSCAT code.[169-171] The DDA simulates the metal particle as an array of N point dipoles of known polarizability tensor organised on a cubic lattice to represent the nanoparticle shape. Each dipole interacts with the incident electromagnetic wave and with the waves re-radiated by all the other dipoles. This method has found many applications in modelling plasmonic NPs.[42, 65, 87, 88] The accuracy of DDA calculations critically depends on the discretization step. In order to approximate a given particle adequately, dipoles used in the simulation must be significantly smaller than the light wavelength.[172] Moreover, the inter-particle distance, r, must satisfy the condition $\left|n_{NP}\right| \cdot k \cdot r \leq 1$, where n_{NP} is the particle refractive index and k is the light wavenumber in the medium.[166, 173] A great advantage of the DDA approach is that it can be applied to arbitrarily shaped structures. Another remarkable advantage is that target optical constants are introduced directly from experimental data, independently of composition or geometry, and without any need for the interpolation with analytical models of the optical constants.[87, 88, 174]

The main drawback of this method is that it can produce artefacts when the number of dipoles is not large enough, and it can become time consuming and much demanding in terms of computing resources for large N.[148, 172] The theoretical basis for the DDA are reported in paragraph S4 of S.I.

3.2.2b FDTD. Another numerical approach that has been widely used to study the optical properties of metal nanostructures is the FDTD method.[175-177] The method is based on the numerical integration of the Maxwell equations in the time domain within a finite space, where fields will be calculated, containing the object of arbitrary geometry and composition.[153, 176, 178] In practice, space is discretized by a grid mesh (Yee cells). The space and time derivatives of the electric and magnetic fields are approximated using a finite-difference scheme with space and time discretizations selected to minimize computational errors and ensure numerical stability.[147] At the initial time a plane wave source is turned on. The wave excited by the source propagates towards the scattering particle, eventually interacting with it.[162] The fields are specified at spatial grid points and values at the grid points for the previous and current time steps are used to calculate the values at the next time step.

Advantages of the FDTD method come from its simple implementation, flexibility, and versatility. Moreover, the computational demand of FDTD grows only linearly with the number of parametrization points.[153] Like the DDA, the FDTD method can be applied to any particle shape. Disadvantages may be due to some limitations in terms of efficiency and accuracy when mesh spacing is large compared to NPs features (on the other hand, FDTD computations may be very time consuming when mesh size is very dense), and in terms of the maximum particle size parameter p.[147] The most widely used FDTD codes are commercial, such as the LumericalFDTD Solutions(TM), although free codes are also available (see Table 1).

3.2.2.c BEM. Another popular and efficient approach is the BEM, based on vector diffraction theory,[179] in which the electromagnetic field is expressed in terms of charges and currents distributed on the surfaces and interfaces of the particle.[162] By imposing the boundary conditions for the continuity of the tangential components of the electric and magnetic fields, a system of surface-integral equations is obtained. The solution is obtained by discretization of the integrals using a set of N representative points distributed at the boundaries. This ends up with a set of linear equations that are solved numerically by linear algebra techniques.[153, 180] The main advantages offered by BEM are a low computational and storage demand and the need for discretizing only the particle surface, which allows calculations with a number of nonspherical NPs that would not be feasible with the other models.[181] In fact, particle contour is discretized through a grid of points on the surfaces between different regions, with a variable frame that must be defined with the appropriate density to obtain accurate results.[153]

3.2.2d FEM. In FEM, the total simulation volume is discretized into a set of finite elements (tetrahedra or triangular prisms) chosed to best describe the geometry of the target. The unknown functions are represented by simple interpolation functions defined on each element with unknown coefficients. These functions provide an approximation to the solution within a finite element, which is obtained by recursively solving the corresponding system of equations. The region of computation is terminated using some artificial absorbing boundary, like in FDTD.

Although the most popular FEM code is commercial (Comsol(TM) Multiphysics package), free codes are also available (see Table 1).

3.2.2e T-matrix. A powerful approach, especially when dealing with dispersions of randomly oriented particles and aggregates, is the transition matrix (T-matrix) technique.[147, 182] The method, originally introduced by Waterman,[183] is based on the multipole expansions of the electromagnetic fields, so mainly the same framework in which the Lorenz-Mie theory develops. As a matter of fact, the T-matrix method reduces to the Lorenz-Mie theory when the scattering particle is a single isolated (homogenous or layered) sphere.[147] However, the T-matrix approach has proved to be very suitable to solve the light scattering problem by aggregates of spherical particles.[147, 182] Often in the literature the aggregates of spherical NPs are handled within the generalized Mie theory (GMT) which is based on the same kind of approach.[162]

In many cases the T-matrix allows a rigorous description of the scattering process, surpassing other commonly used techniques in terms of efficiency and x range that is possible to explore.[184, 185] A great advantage of the method results from the transformation properties under rotation of the T-matrix and concerns the possibility to perform an analytical evaluation of the scattering characteristics averaged over particle orientation.[186-188] This unique feature of the T-matrix method has relevant effects in saving computational time. Given a particle reference frame, the T-matrix needs to be computed only once, then the average scattering characteristics of a particle dispersion can be computed through simple analytical formulas.[147, 182] This interesting property makes the computational effort required by the T-matrix method much lighter than the one required by other approaches, like the DDA and the FDTD, which need *ex novo* calculation of the scattered field whenever the orientation of the scattering particle changes. Importantly, the T-matrix is a rigorous method for describing light scattering and the results are obtained with high accuracy; DDA, FDTD, and effective medium theories (see paragraph 3.2.3), on the other hand, involve approximations in the numerical simulations and so have to be considered as approximate methods.[189] The drawback of the T-matrix approach is that it is limited to spherical nanoparticles and their assemblies.[147, 182] Additional details about the Transition matrix method are reported in paragraph S5 of S.I.

3.2.2f Hybridization model (HM). This model accounts for hybrid plasmon modes appearing in NPs assemblies, or complex structures such as core shell or multilayers.[190, 191] In the HM, the new LSPs are expressed as linear combinations of non-interacting dipolar plasmons, in analogy to molecular orbital theory, justifying the concept of “plasmonic molecules”.[191] For instance, in a Au NPs dimer, the two non interacting LSP modes originates two hybrid modes corresponding to the bonding and antibonding combination.[190] Only the lower energy mode can be excited by electromagnetic radiation and is defined as bright or bonding state, while the other one is a dark or anti bonding state, non optically active (i.e. not emitting in the far field). By exploiting the analogy with the mass-spring harmonic oscillatior, dark modes are antiphase oscillations in which the "center of mass" is fixed, i.e. there is no net displacement of the electronic charge in the far field.[190]

According to the HM, the plasmon modes of a core-shell Au-dielectric NP are originated from the plasmon of a metal sphere and that of a cavity in a metal matrix, whose interaction produces two new plasmonic states with energy higher and lower than pristine plasmons.[191] The physical basis of HM is the interaction between free electrons, that are modelled as a charged incompressible liquid bound to the positive Au ion cores, in close analogy to the spring-mass model.

3.2.3 Effective medium theories (EMTs). EMTs provide alternative description of the light scattering properties of inhomogeneous, irregularly shaped particles or nanocomposite media with weakly interacting NPs, i.e. where NPs are well separated.[162, 189, 192] The real particle is approximated by a homogeneous one, e.g. a sphere, with an effective dielectric function obtained from a mixture of the dielectric functions of the surrounding matrix and of the particle inclusions. The resulting dielectric function is used in place of the pure metal one to reproduce the optical properties of Au NPs, for instance in the Mie or the T-matrix models.

Well known examples of EMTs mixing rules are the Maxwell-Garnett and the Bruggeman ones (see paragraph S6 in S.I. for the analytical expressions). They both come from the same integral equation, but with different approximations.[193] Although both theories provide similar results in most cases, the Bruggeman effective dielectric function generally applies to a randomly inhomogeneous medium, that is a medium in which no distinguishable inclusions, embedded in a matrix, appear.[37]

The simplicity of the method made the EMTs to be widely used, however strong concerns exist about their accuracy. The most limiting assumption of EMTs is that they do not take into account the real sample composition, hence EMTs fail when large voids and inclusions (compared with the wavelength of light) are present.[162, 189, 192]

4. Applications related to SPR optical extinction.

4.1 Sensing and imaging with plasmon resonance.

4.1.1 Sensing. The high σ_{Ext} and the possibility to modulate the SPR in response to a change of the surrounding chemical environment (see paragraph 2.1) makes the Au NPs an excellent signal transducer, widely used for the development of sensors.[2, 34] Sensing of chemical and biological species using plasmonic Au NPs has received considerable scientific attention with important implications in the field of environmental sciences, diagnostics and medicine.[194-196] In addition to their optical properties, Au NPs hold several attributes that make them an ideal sensing platform, including:[197]

(i) ease of synthesis,

(ii) chemical stability, photostability and biocompatibility,

(iii) high-surface to volume ratio, to enhance the sensitivity since the detection events between the analyte and the receptors occur on the particle surface,

(iv) functionalization of the surface with multiple organic and biological ligands for the interaction with the target analyte,

(*v)* large extinction cross sections, allowing single NPs sensors or single molecule assay in best cases.

Besides, optical extinction in NPs ensembles can be probed with UV-vis spectrometers, that are present in most laboratories, without altering the sample, and the registration of the spectrum requires short times.[34]

The ability to tune the optical properties, that depends on the particle size, shape and aggregation,[197] and to control the surface binding properties by suitable functionalization with proper ligands,[198] have provided many insights into the fabrication of sensitive and selective sensors with numerous applications in clinical diagnostic.

In order to generate a detectable response signal, the analyte-receptor event has to generate changes of the SPR. This signal transduction event has been achieved through analyte induced alterations in the interparticle distance, size and the dielectric constant of the surrounding solution (Figure 12). The two main classes of optical sensors based on Au NPs are colorimetric or connected to the SPR spectral shift.[34, 197, 199]

4.1.1a Colorimetric sensing with assemlies of NPs. The binding of the analyte on the NPs surface can induce aggregation of the NPs resulting in interparticle surface plasmon coupling (see paragraph 2.3) that translates in a visible change of color of the colloidal solution from red to blue (in case of Au nanospheres).[200] During the last two decades, several colorimetric sensors have been developed for the detection of a variety of compounds, such as metal ions,[201, 202] small organic molecules,[203, 204] proteins,[205-207] DNA,[208-211] and living cells.[212] For instance, DNA mediated assembly of Au NPs has been widely used to develop sensors for the detection of genetic mutation of DNA, which has important implications for the early diagnosis of many disease including cancer.[213] In this approach, two Au NPs probes were functionalized with two single-stranded DNA, complementary to the target oligonucleotide. The formation of double stranded DNA occurred in the presence of the target DNA, inducing the Au NPs aggregation and the concomitant color changes of the solution. By using this strategy, the selective and high sensitive (at subnanomolar level) detection of DNA was achieved,[208, 214] as the result of the high specificity of the base-pair hybridization along with the intense absoption of Au NPs. The readout of the signal for these assays, that in some configuration results in a visible color change of the colloidal solution, can be performed by the naked eyes or with UV-Vis spectrophotometers, allowing DNA detection at low cost.

Colorimetric assays for the detection of proteins of clinical interests have been developed using Au NPs coated with specific antibodies. The NPs aggregation and the corresponding color change of the colloidal solution is triggered by the target antigen through the antigen−antibody interaction. An important application of this colorimetric immunoassay is the detection of the β-hCG, an hormone released by pregnancy women, which is resulted in the well-known easy, rapid and low-cost pregnancy test.[197, 215]

Plasmon coupling in nearby Au NPs is also exploited in molecular rulers based on the SPR dependence on the distance between two metal nanoparticles.[216] Plasmon molecular rulers have been applied to the real time sensing of DNA hybridization processes as well as to DNA folding in presence of different saline buffers. In particular the SPR sensitivity on the coupling distance of two metal nanoparticles is so high that each step of dimer formation is measurable, included elastic recoil after the first contact.[216] Au NP of 40 nm in diameter allows monitoring distances up to 70 nm by far field extinction microscopy of a single dimer.[216] Contrary to organic fluorophores, which suffers of photobleaching, plasmon rulers are photostable, which allows the measurement down to a single NPs dimer.

4.1.1b SPR shift sensing. Another efficient strategy to monitor the binding of the analyte on the surface of functionalized Au NPs is based on local change of the refractive index of the medium surrounding the NP surface, that does not require changes of NPs assembly in response to the analyte. Starting from the Frolich condition (eq. (4)), it is possible to find an approximated linear relationship between the SPR maximum (λ_{max}) and the environment refractive index $n_m = \sqrt{\varepsilon_m}$:[34]

$$\lambda_{max} = \frac{2\pi c}{\omega_p}\sqrt{2n_m^2 + 1} \qquad (22)$$

where c is the light speed. Although the SPR wavelength is not strictly linear with n_m, this trend agrees with more accurate theoretical predictions and experimental results over small ranges of n. Eq. (22) provides the basis for expressing the refractive index sensitivity S of a NP in nanometers of peak shift (or eV if the energy scale is preferred) per refractive index unit (nm/RIU or eV/RIU):[34]

$$S = \frac{d\lambda_{max}}{dn_m} \tag{23}$$

In general, the precision for change of n_m depends on both S and the peak line width ($\Delta\lambda_{max}$). Therefore, a figure of merit (FOM) for LSP sensing can be obtained by dividing the sensitivity by the resonance line width:[34]

$$FOM = \frac{S}{\Delta\lambda_{max}} \tag{24}$$

An alternative FOM (FOM*) exists,[217] which considers the change in light scattered intensity (dI/I_0) at a given wavelngth (λ_0) versus n_m change, without including the line width:

$$FOM^* = \frac{1}{I(\lambda_0)} \frac{dI(\lambda_0)}{dn_m} \tag{25}$$

This is useful when it is difficult to define a consistent SPR line width, such as in the case of NPs lacking a single plasmon band. FOM* measured at $\lambda_0=\lambda_{max}$ can be expressed also as a function of S:[34]

$$FOM^* = \frac{1}{I(\lambda_{max})} \frac{dI(\lambda_{max})}{d\lambda_{max}} \frac{d\lambda_{max}}{dn_m} = \frac{S}{I(\lambda_{max})} \frac{dI(\lambda_{max})}{d\lambda_{max}} \tag{26}$$

In this way, sensors based on changes in intensity and those based on peak shifts can be directly compared.

The performances of the sensors are greatly enhanced when the NPs are fixed on substrates such as glass and metal films, rather than in solution. In these cases, the detection relies in UV-vis spectroscopy or in far field extinction microscopy.[34]

This type of SPR sensors allowed the detection of proteins by using biotin-streptavidin[218] or antigen-antibody interactions in microfluidic channels.[219] Immobilized Au NPs on a thin metal film have been also employed for the amplification of the signal of a propagating surface plasmon resonance, allowing the development of highly sensitive Au NP-based SPR sensors.[8] The enhancement of the SPR signal in the presence of Au NPs relies on the electronic coupling between the LSPR of the Au NPs and the surface plasmon wave generated on the Au sensing film.[8] Immunoassays have been developed using this principle to detect a variety of proteins and hormones in biological samples, demonstrating a signal enhancement of several orders when comparing to conventional propagating SPR sensors.[220-223]

4.1.2 Dark-field imaging. Isolated and aggregated Au NPs with size >30 nm possess large Rayleigh scattering cross section, that is ideal for cellular imaging using conventional dark-field microscopy, where signal comes from the intense light scattering from the label.[4] This is possible without any staining and also in living cells.[4] Several studies showed the possibility of monitoring Au NPs localization in specific cell compartments (Figure 13A),[224] penetration through specific cell barriers or specific receptors recognition.[3, 4, 225] All these features are connected to the surface coating of NPs or to the presence of targeting functions such as peptides or antibodies, as discussed below.

4.1.3 Role of surface functionalization. A key consideration in the development of a sensing or imaging platform based on Au NPs is their surface functionalization with recognition units, which allow the specific interaction with the target molecule, yet avoiding unspecific interactions (see Figure 13B). The nature of these NPs ligands has also a primary role in the stabilization of the particle itself, providing the interface between the NPs core and the surrounding environment. Indeed, the chemical synthesis of Au NPs involves the use of capping ligands, such as surfactants, which need to be removed for the modification with a specific recognition unit, but are not present in NPs obtained by laser ablation in liquids.[18, 81, 226] In the latter case, sensing of surface bioconjugation by monitoring the SPR red shift upon binding is possible,[226] and exploitable for controlling NPs sequential multi-functionalization.[224]

The most common and versatile surface chemistry performed on Au NPs uses thiol ligands, thanks to the formation of the strong gold-thiol interaction.[222, 227] Self-assembled monolayer of alkanethiols provides a simple and convenient system to tailor the interface properties of the Au NPs by using a whole gamut of terminal functional groups.[19, 228]

For sensing and imaging applications in biological environments, the compact layer of alkanethiols on the Au NPs is important to improve

(i) the biocompatibility,

(ii) the resistance to nonspecific adsorption of biological molecules, by using for example the thiol-terminated polyethylene glycol chains,[229] and

(iii) the stability of NPs in different environments.[34, 197, 199]

In addition, these functional groups provide suitable anchoring units for the immobilization of biomolecules, such as proteins, antibodies, nucleic acids, or other receptors for the specific recognition of the target analyte.[1]

4.2 Staining, information storage and photochromism.

The large extinction cross section, bright tuneable colors and physical and chemical stability of Au NP motivated their use in staining since centuries (see section 1). These properties are now being integrated with advanced technologies such as ink-jet printing,[26] or as new dyes for old tissues such as merino wool.[230] Importantly, the sensitivity of SPR to dielectric and compositional changes are exploitable for dynamic real-time color tuning, for instance for camouflage purposes (Figure 14A).[231]

Also optical information storage with the possibility of multiplexed optical recording is possible by exploiting the SPR tuneability with the length of Au nanorods, and the anisotropy of their optical extinction).[232] Optical recording can be made non permanent by exlpoiting reversible aggregation of Au NPs with appropriate surface functionalization (Figure 14B).[233]

4.3 Photothermal effects.

The conversion of light into heat is extremely efficient in Au NPs due to the combination of the following features:[6, 82, 234]

(i) efficient plasmon absorption in the visible and near infrared (NIR) regions,
(ii) excellent photostability compared to organic compounds,
(iii) low luminescence yield,
(iv) rapid relaxation of the SPR.

In particular, the absorption cross-section of Au NPs is several orders of magnitude larger than even the strongest absorbing organic chromophores,[6, 235] and the SPR can be tuned to the most suitable spectral regions, such as the “water transparency windows” where body tissues are more optically transparent (700–950 nm and 1000–1350 nm),[236, 237] making it also possible to heat gold nanoparticles in vivo.[6]

The photothermal heating mechanism after SPR excitation has been investigated intensively with ultrafast spectroscopies, and is well modelled with the TTM[51, 238] (see paragraph 2.2). These studies indicated that energy transfer from light to the environment, i.e. heating of the surrounding medium, occurs by phonon-phonon scattering already on a time scale of hundreds of ps after SPR excitation.[51]

Although the process is relatively simple in case of a single LSP excitation, in photothermal experiments each NPs absorb multiple photons in order to increase the surrounding temperature as much as possible, meaning that multiple LSPs are continuously excited during the irradiation period.[238] Therefore, with increasing intensity of the light source, the Au NP lattice temperature can increase more and more, passing through the following steps (Figure 15):[238]

(i) the threshold for acoustic vibration of the lattice, due to transient thermal expansion;
(ii) the melting threshold, which induce an irreversible shape transformation (for instance nanorods are melted into nanospheres);
(iii) the vaporization threshold, which induces size reduction of the original NPs and formation of smaller NPs in the surrounding medium by nucleation and growth of the Au vapours;
(iv) fragmentation of the NPs into smaller particles due to either boiling or Coulomb explosion, the latter due to electron ejection by photoionization or thermoelectric effect.

Similarly, the surrounding medium can be heated, melted, vaporized or deteriorated depending on the temperature reached by the Au NPs. In particular, vaporization is associated to cavitation, i.e. formation of a vapour bubble with larger pressure than the surrounding medium, which expands until cooling and collapsing (Figure 15). In all cases, a stress wave due to medium thermal expansion propagates in the surroundings of the heated NP.

This remarkable number of phenomena associated to photothermal heating depends on NPs absorption efficiency (i.e. particle size, shape, aggregation state and composition) as well as on the incident light parameters (i.e. intensity, wavelength, pulse duration, polarization).[6, 235, 238] However, there are some general criteria for maximizing photothermal effects in Au NPs. First of all, photons exciting plasmons are either absorbed or scattered, with probability of the two events determined by the respective σ_{Abs} and σ_{Sca} (see paragraph 2.2.1). In particular, there is a size threshold above which scattering prevails over absorption, which depends on the shape, structure, and composition of NPs.[4, 6, 37] For Au NPs it falls approximately at 80–100 nm, while Au NPs with size smaller than ~25 nm behave as pure plasmon absorbers, because of negligible σ_{Sca} compared to σ_{Abs} (Figure 7).[80, 81, 129] This means that absorption for unit mass (σ_{Abs}/V_{NP}) is maximized by reducing the particle size.[80, 143, 239] Since the cross section classically corresponds to the geometrical section of an ideally opaque object (*Tras*=100%) estinguishing the same number of photons of the NP (Figure 16A), another useful figure of merit for plasmon absorption is σ_{Abs}/S_{NP},[80] where S_{NP} is the geometrical NPs cross section. For instance, in case of an isolated Au nanosphere in water, the maximum σ_{Abs}/V_{NP} and σ_{Abs}/S_{NP} are reached at, respectively, 50 and 70 nm (Figure 16).

The importance of σ_{Abs} for local heating is well explained by the expression of the heat (q_{NP}) generated inside the NP:[144, 240]

$$q_{NP} = \sigma_{Abs}(\omega) I(\omega) = \frac{1}{2}\omega\varepsilon_m \int Im[\varepsilon(\omega)] E^2_{NP}(\omega) dV_{NP} \qquad (27)$$

A similar trend is found for the local temperature around a single NP in the steady-state regime:[40, 144, 240]

$$\Delta T(r) = \frac{q_{NP}}{4\pi K r} = \frac{\sigma_{Abs}(\omega) I(\omega)}{4\pi K_m r} \qquad (28)$$

where r is the distance from the center of the NP, and K_m is the thermal conductivity of the surrounding medium. The maximum temperature increase occurs at NPs surface (i.e. at $r = R_{NP}$), and since $\sigma_{Abs} \propto V_{NP} \propto R_{NP}^3$, the maximum ΔT is proportional to the second power of the NP radius. The two factors leading to this dependence are:[82, 83]

(i) the total heat generation rate inside the NP, proportional to the NP volume,

(ii) the total heat transfer through the NP surface, which is a function growing with NP surface area.

The measurement of local temperature at the surface of NPs is very challenging, and can be made through monitoring phase transformations of the surrounding matrix[82, 83] or with photothermal optical probes.[241]

Despite the σ_{Abs}/V_{NP} is maximum for small NPs, eq. (28) provides the important information that the absolute capacity of light-to-heat conversion for a single NP is proportional to NPs volume. Therefore, the most obvious way to increase ΔT is increasing the number of nanoparticles in the point of interest.[82] Besides, one can choose the shape and composition to maximize σ_{Abs} at the excitation wavelength.[80, 143, 239] For instance, at equal volumes, Au nanorods (NRs) have larger σ_{Abs} than Au nanoshells (NSs) composed of a silica core coated with a gold layer,[80] and Fe-doped Au nanoshells have up to 100% larger σ_{abs} than pure Au ones.[35]

There is a long list of applications possible for Au NPs with efficient absorption in the visible and NIR regions (Figure 17), such as photothermal therapy,[6, 124] light triggered drug release,[242, 243] antimicrobial systems,[244, 245] photoacoustic imaging[246] photothermal contrast imaging,[247] photothermal phase transformations.[248, 249] Another consequence of photon absorption is the alteration of the equilibrium electron Fermi distribution in the metal NPs, which allows charge injection in the conduction band of nearby materials, and it is exploited for plasmon enhanced catalysis and photocurrent generation.[60]

In analogy to sensing and labelling applications (see paragraph 4.1), the biocompatibility and the ability to conjugate Au nanoparticles with functional organic molecules is very important for most of the photothermal applications. For instance, surface functionalization is required for the colloidal stability in biological fluids or in liquid solution, the inclusion in polymeric matrixes, the addition of selectivity for biomolecules or other chemical species, and the formation of surface patterns with multiple applications.[6, 81, 124, 235]

4.3.1 Photothermal therapy (PT) and cell killing. PT offers a gentler alternative for cancer treatment by using optical heating for ablation of tumors.[6, 235] PT is mainly based on protein denaturation and cellular membrane disruption, with initiation of apoptotic mechanisms, when tissue temperature exceeds 42–44 °C.[6, 235, 250]

Photothermal therapy requires that strong photoabsorbers are located selectively in the tumor region to reduce nonspecific injury to adjacent healthy tissue.[251] The absorption cross-section of Au NPs (σ_{Abs} ~ 2.9 10^{-15} m^2 for 40 nm spheres with an absorption band around 530 nm) is five orders of magnitude larger than that of indocyanine green (σ_{Abs} ~ 1.7 10^{-20} m^2 around 800 nm), a dye used in earlier demonstrations of laser photothermal tumor therapy, thus promising higher efficacy at much lower irradiation energy.[124] SPR in the NIR region are useful for biological applications because of the transparency peak of skin, tissues, haemoglobin and blood in that spectral region,[236, 237] thus pointing to shapes such as nano-rods, -stars, -corals and -shells (see Figure 9).[6, 124] Besides, guiding *in vivo* the PT with the same plasmonic NPs is possible by using photoacustic (see paragraph 4.3.5) or SERS (see paragraph 5.2.4b) imaging techniques. Although tissue penetration is limited to tens of mm, the use of optical fibers is under investigation for PT in deep tissues, and Au nanoshells are currently under clinical validation for therapy of humans.[6]

The same principle of PT can be used for the realization of photothermal antimicrobial surface or substrates that destroy bacteria by light-triggered temperature increase.[244, 245]

4.3.2 Photothermal drug release and diffusion. The diffusion coefficient D of any molecular compound in a fluid medium is described by the Einstein-Smoluchowski law:[252]

$$D = f_{geom} \frac{k_B T}{\eta_m} \approx T e^{-a/T} \tag{29}$$

where k_B is the Boltzmann constant, f_{geom} is a geometrical factor depending on molecule shape, and η_m is the medium viscosity, that scales approximately as $e^{-a/T}$ with T. Therefore, local increase of T is a way to activate the diffusion of molecules near NPs surface.[253] In the most sophisticated cases, Au NPs can be included in polymeric cargos loaded with drugs, that open after T increase to release their payload,[254] or hydrogel matrixes.[255] Perfusion and oxygenation of tissues are also favoured by moderate heating, which justify the use of Au NPs for photothermal improvement of the delivery of cytostatic drugs.[242, 243]

4.3.3 Photothermal contrast imaging. In photothermal imaging, Au NPs are heated by a laser beam, while a second weaker probe beam is exploited to locally measure the changes in refractive index due to the temperatue gradient.[247] This technique allows monitoring very small single Au NPs (i.e. below 10nm) inside cells.[256]

4.3.4 Nanobubbling. Nanoscale bubble generation is exploitable for photoacustic imaging[257] (see paragraph 4.3.5), gene therapy treatments,[258] or direct suppression of tumor cells by cell membrane perforation.[259]

Repeated and effective bubble formation without particles fragmentation requires the use of optimal Au NPs structure and laser parameters. Interestingly, this occurs relatively far from SPR in case of single Au nanoshells.[258] In analogy with any photothermal application, the assemblies of multiple small Au NPs into large aggregates are very efficient for bubble formation, as demonstrated with self-assembled gold nanorods in lipid bilayer microcapsules.[259]

The vapor layer forms around the surface of Au NPs already tens of ps after SPR excitation, although nanoscale bubbles appear after 10^2-10^4 ps (Figure 18).

Short (ns) and ultrashort (ps, fs) laser pulses are usually exploited for nanobubbling, while the use of continuous wave (CW) is less frequent.[260] In fact, the threshold for nanobubble formation is lower for shorter pulses, due to competition of thermal dissipation mechanisms on the ns timescale and refractive index modification in the NP surrounding after bubble formation (hundreds of ns and longer) which makes light absorption from the metal particles very inefficient.[257, 260]

Interestingly, the local temperature required to trigger bubble generation is much larger than 100 °C, meaning that superheated liquid water, up to 220 °C, is achieved under ambient pressure conditions and even over arbitrary large areas by plasmon Au NPs heating.[248] This was exploited for proof-of-concept solvothermal synthesis, i.e. synthesis occurring in metastable liquids above their boiling point, which normally requires the use of a sealed autoclave under pressure to prevent the solvent from boiling.[261]

4.3.5 Photoacoustic imaging (PA). PA imaging (also called optoacustic imaging) is a rapidly emerging imaging modality with non invasive nature and relatively easy coupling with plasmonic nanoparticles for increased imaging contrast.[246] In PA imaging, acoustic waves are generated from the absorption of light, usually from a ns laser, by thermal-induced expansion of the medium surrounding Au NPs.[4, 246] The PA signal obtained is proportional to the Au NP concentration.[4] PA resolution is set by the laser spot size at the focal plane, which is of the order of 20 - 30 μm.[4, 246] PA can provide depth penetration of 10 - 50 mm, that is suitable for in vivo imaging.[262] There are several PA variants, however in the most common version the laser intensity is sufficiently high to promote bubble formation around Au NPs.[246, 263] A key empowering feature in this field is the development of red-NIR contrast agents which remains photostable.[246, 264, 265]

Recently, the PA ability of Au NPs was exploited for intraoperative tumor detection and surgical elimination of microscopic malignant lesions in vivo.[257] The selectivity for tumor tissues exploits two properties of Au NPs, *(i)* surface conjugation with antibodies, *(ii)* threshold energy for nanobubble generation significantly lower for large clusters of NPs, which are self-assembled by cancer cells through endocytosis of the NPs, compared to isolated or small clusters of NPs, which are non-specifically accumulated by normal cells. Importantly, the whole procedure exploits clinically validated gold colloids (conjugated to clinical antibodies against cancer-specific receptors).[257]

4.3.6 Photothermal activation of phase transformation. Au NPs are suitable for releasing controlled amounts of heat in nanoscopic regions. This allows controlled nanoscale phase separation and phase transitions, such as the formation of gold-polymer core-shell structures from polymer aqueous solution,[266] or the reversible gel-fluid transformation in phospholipid membranes,[267] or controlled chemical modifications.[268] Heating Au NPs in fluid media is also a way to control their velocity and to guide the nanoparticles to specific locations.[267, 268]

High intensity laser irradiation of Au NPs on borosilicate glass allowed substrate modification, with formation of nanometric craters, associated to NPs fragmentation and spread over the surface.[269] Another application related to phase transition concerns light induced vapour generation.[249, 270] Broadband light-absorbing Au NPs are well suited for sunlight photothermal heaters and generation of steam in standalone solar autoclave useful for sanitation of instruments or materials in resource-limited, remote locations.[270] The same principle was exploited also for water–ethanol distillation, yielding fractions significantly richer in ethanol content than simple thermal distillation.[271]

4.3.7 Au NPs welding, alloying and shape transformation. Heating of Au NPs assemblies at T close to the melting threshold allows formation of interparticle connections, resulting in nanobelts and nanochains.[272] At higher fluence, NPs size can be reduced by photofragmentation (above vaporization threshold), or increased by melting of NPs agglomerates into single objects (below vaporization thershold).[18, 238] Laser pulses are usually preferred to cw sources for obtaining selective and rapid delivery of energy to Au NPs. Laser irradiation also allows size reduction or increase,[18, 226, 238] shape transformation from low symmetry shapes into spheres,[51, 238] or growth into nanocorals supporting broadband SPR from visible to NIR.[81] Photofragmentation in the presence of various metal NPs is a way to obtain intermetallic or alloy NPs.[273]

4.3.8 Photothermal activation of chemical reactions. Heating is exploitable for nanoscale thermal activation of reactant molecules. A wide series of examples exist, including growth of semiconductor nanowires and carbon nanotubes by chemical vapor deposition (CVD) assisted by local heating of nanoscale metallic catalysts, thermal decomposition reactions, cross-linking reactions, decomposition reactions in the solid state, recrystallization of amorphous TiO_2 to anatase, radical polymerization, and thermal curing of polymers such as PDMS.[274] The synthesis of polymer nanostructures on the nanometer scale due to SPR-induced photothermal chemical reactions allows precise positioning of polymer layers with subdiffraction-limited spatial resolution.[274] Although theoretical calculations suggest that the origin of heat generation is not uniform over anisotropic Au NPs volume,[143, 240] these experiments allowed to identify that the steady-state temperature profile of photothermally heated NP is uniform because of thermal equilibrium within the metal lattice occurs just after hundreds of ps.[82, 83, 274]

A powerful advantage brought from the plasmon properties of Au NPs, is the ability of tracking chemical modifications at particles surface by SERS in real time (paragraph 5.2.4c). For instance, this was demonstrated with a Diels-Alder cycloaddition reaction photothermally activated in a nanometer-volume cavity.[275]

4.4 Plasmon induced hot-carrier effects.

Relaxation of LSP yields to the alteration of the equilibrium electron Fermi distribution in the metal and formation of "hot-electrons" (see paragraph 2.2). By definition, electrons are "hot" when they have larger energies than the thermal excitation at room temperature.[60, 274] Excitation of electrons in a solid is always associated to the formation of holes, therefore hot electrons implies the presence of "hot holes" with lower energies than at room temperature.[60, 276, 277] Due to their excess kinetic energy, hot-electrons can transfer into unoccupied levels of acceptor molecules or materials in contact with Au NPs surface (Figure 19). In fact, the activation enthalpy of electron transfer reactions catalysed by Au NPs is significantly reduced under visible light photoexcitation.[278]

Similarly, electron transfer from occupied adsorbate orbitals to hot-holes (i.e. transiently unoccupied states below Fermi energy in the metal) has been demonstrated.[60]

The geometry of NPs can be engineered to control the transfer of hot carriers to nearby species, a process that occurs preferentially from hot spots at NPs junctions, spikes, points or edges.[279] Size[276] and surface coating[277] of Au NPs are crucial parameters for the efficiency of the process.

The probability of hot-carrier transfer is lowered by their rapid relaxation and conversion into heat, and the difficult of matching their energy with the donors/acceptor levels.[60, 280] In general, the process is possible only for acceptors or donors electronic levels with energy close to the metal Fermi level.[60, 280]

When light intensity is large enough, the photoelectric effect is possible. In this case, angle-resolved photoemission spectroscopy can directly probe preferential photoemission from hot spots and subsequent charge acceleration by the evanescent plasmon field.[281]

Despite these challenges, hot-carriers are exploitable for multiple applications such as in light harvesting, photodetection, doping and photochemical reactions.[60] For instance, room-temperature dissociation of H_2 at Au NPs surface was reported.[282] Best performances are observed by coupling the Au NPs to other catalytic materials, such as Pt, TiO_2, MoS_2 or semiconductors quantum dots, forming hetero-nanostructures in which each component has direct contact with the other, to facilitate the photoinduced hot-carrier transfer.[276, 277, 283-285] For instance, fs pump-probe spectroscopy demonstrated that plasmon-induced hot electron transfer takes place in the Au NPs/MoS_2 heterostructure on a time scale of 200 fs.[286] These heterostructures allow artificial photosynthesis experiments on the photoelectrochemical water splitting by combining both plasmon-induced hot electrons and holes generation in the same integrated device.[287] Also generation of ammonia from atmospheric nitrogen and water using sunlight was possible with a strontium titanate ($SrTiO_3$) photoelectrode loaded with Au NPs and a zirconium/zirconium oxide

(Zr/ZrO_x) thin film.[288] In alternative to heterostructures, alloying of Au with catalytically active metals such as Pd or Pt was also reported.[136-138]

Beyond catalysis, hot electrons can be emitted over a Schottky barrier to produce a photocurrent in photodetectors with high responsivity,[60] while their application in plasmonic solar cells is more difficult due to the low internal quantum efficiency.[280]

5. Applications related to local field enhancement.

5.1 Local field enhancement.

One of the main reasons for the interest in Au NPs is their unique ability to channel far-field radiation to subwavelength dimensions, thus amplifying the electromagnetic field near particle's surface, i.e to act as nanolenses.[15] The nanolensing behaviour has been exploited to enhance several types of optical phenomena in nearby molecules or materials, such as Raman Scattering,[289] Fluorescence,[290] visible[291] and Infrared-Red extinction,[292] Coherent Anti-Stokes Raman Scattering (CARS),[293, 294] Hyper-Raman Scattering,[295, 296] and a series of other linear and nonlinear optical effects that are discussed in section 6.

In the literature, two different approaches are mainly used to describe the local field enhancement in plasmonic nanostructures:[15]

i) An euristic description based on the mechanical analogy with a mass spring harmonic oscillator, according to which the plasmon-induced near-field is directly proportional to the mass displacement, which corresponds to the charge density accumulated at the edge of the nanoantenna.[32, 33] Therefore, the local field is due to the instantaneous electrostatic field of the dipole generated by the charge density displacement.[32, 33]

ii) An electromagnetic approach which refers to the radiation generated by the radiative decay of the SPR (i.e. light scattering), associated to time-dependent electromagnetic fields that extend beyond the nanoparticle surface in the near-field by some nanometers, and transform into propagating plane waves in far field distance (i.e. at a distance larger than photon wavelength).[10, 34]

One can observe that the typical scattering cross section of a 100 nm Au nanosphere in water at the SPR maximum is of 3.6 10^{-14} m^2, that is 4.6 times the NP geometric cross section. It must be noted that the crossover between σ_{Sca} and the geometric cross section occurs in NPs larger than ~30 - 40 nm (see Figure 16 for Au nanospheres).

The local field enhancement factor EF at any point $\vec{r}$ can be expressed as the ratio of the moduli of the local electric field E_{loc} to the incident electric field E_0:[15, 146, 163]

$$EF(\vec{r}\,) = \frac{E_{loc}(\vec{r}\,)}{E_0} \qquad (30)$$

EF is dramatically affected by NPs structural parameters and position around the surface, and can range from less than 1 up to 10^2-10^3. The points with the largest *EF* in a single NP or a group of them are called electromagnetic “hot spots”.[146] On the other hand, some points on NPs surface can have $EF<1$ due to destructive interference between incident and scattered light.[15, 297]

In isolated NPs, the *EF* is larger in shapes with edges (nanocubes) or tips (nanorods, nanostars, nanotriangles, nanocones), as shown in Figure 20A-B.[42] However, the largest *EF* are possible at the junctions between NPs, such as in dimers, trimers and so on.[298] In the simple case of a NPs dimer, the *EF* at the junction between the particles increases monotonically as the distance between the two particles is reduced to approximately 1 nm.[97] This is a consequence of the gradual increase in the coupling between the particles while reducing their distance. In fact, the enhancement of the local electric field is limited to the near-field zone, i.e. that zone at a distance smaller than incident light wavelength. In individual nanospheres in the quasistatic regime, the local field scales as $1/r^3$, where r is the distance from NP surface.[15] This is obtained by approximating the LSP in the Au nanosphere to an oscillating dipole with dipole moment $\vec{p}$, to which corresponds a local electric field:[15]

$$\vec{E}_{loc}(r) = \vec{E}_0 + \frac{3\vec{n}(\vec{n}\cdot\vec{p}) - \vec{p}}{4\pi\varepsilon_0\varepsilon_m}\frac{1}{r^3} \qquad (31)$$

where $\vec{n}$ is the unit vector normal to the surface and pointing to the direction of interest. The $\sim 1/r^3$ decay of E_{loc} explains why LSP hybridization and hot spot formation strongly depends on interparticle distance.[97, 103, 105] As a rule of thumb, efficient coupling between NPs leading to hot spots is observed for interparticle separation lower than 0.5 times the NPs diameter.[4]

Below ~1 nm the *EF* remains constant or, according to recent studies, it decreases again, due to the appearance of quantum effects in the interaction between the electronic density of the two NPs, and to the possibility of electron tunneling from surface to surface (see paragraph 3.1.1 about the nonlocality of the optical constant). This is the reason for an estimated maximum *EF* in Au NPs of $\sim 10^2$-10^3.[299]

The remarkable dependence of *EF* on the geometrical arrangement of the nanoparticles,[300] is well described by the comparison of the maximum field enhancement in isolated Au nanospheres, dimers of nanospheres with same size (homodimers) and dimers with different size (heterodimers).[301] In this case, the 4th power of the maximum *EF* (G_{SERS}, see eq. (37)) was considered, because of interest for SERS[302] (see paragraph 5.2), and it was plotted versus NPs size, while maintaining dimers gap fixed at 1 nm (Figure 20D).[301] The results show that EF_{max} in the hot-spot of dimers is much higher than in isolated spheres. Besides, EF_{max} increases with NPs size and is higher for homodimers than in heterodimers at parity of total NPs volume.[301]

5.1.1 Near field red shift. It is worth noting that the maximum of near field intensity occurs at lower frequency than the SPR optical extinction peak,[303, 304] and the entity of red shift depends on NPs structural parameters. Several authors were able to explain this effect with the simple spring-mass model.[32, 33] In fact, when the harmonic oscillator is damped (due to radiative and non radiative plasmon decay mechanisms), the maximum oscillation amplitude (which corresponds to the near-field amplification) is located at lower frequency than the maximum dissipation (which corresponds to the far-field absorption).[32, 33] In particular, the spectral position of the maximum dissipation does not depend on the damping, while the maximum oscillation amplitude shifts to lower energies with increasing damping, meaning that the spectral shifts between near- and far-field peak intensities is larger in strongly scattering NPs (large NPs with large radiative damping) or in poor plasmonic systems (large $Im[\varepsilon]$ with large nonradiative damping).[305]

5.2 SERS.

Raman scattering is a well-established vibrational spectroscopic technique (Figure 21), possessing analyte fingerprint recognition capabilities. The efficiency with which Raman scattering occurs is very low, typically around ~10^{-29}-10^{-31} cm^2/molecule,[306, 307] but they can reach ~10^{-23} cm^2/molecule if the excitation source is resonant with electronic transitions of the molecule.[298, 307]

The intrinsic low efficiency of Raman scattering can be strongly improved if molecules are placed close to plasmonic NPs, in this case we talk about SERS (Figure 22A).[7, 10] The Raman and SERS signals can be formally expressed with the power read by the detector (respectively P_{Raman} and P_{SERS}):[306]

$$P_{Raman} = KNI\sigma_{Raman} \tag{32}$$

$$P_{SERS} = G_{SERS} P_{Raman} \tag{33}$$

where N is the number of illuminated molecules, I the laser intensity, σ_{Raman} the differential Raman cross section of the molecule and K is a proportionality constant accounting for the quantum efficiency of the detector, the transmittance of the spectrograph, the collection geometry and the collection optics (including the numerical aperture of the objective if a microscope is used).

G_{SERS} is called the total SERS enhancement factor and represents the effect of the plasmonic structure.[7, 10] G_{SERS} depends on two terms:[7, 10]

$$G_{SERS} = G_{em} G_{chem} \tag{34}$$

that account for the increase of signal due to, respectively, the electromagnetic (G_{em}) and the chemical (G_{chem}) effects.

5.2.1 Chemical enhancement (CE). The CE corresponds to a modification of the Raman cross section of a molecule, due to the adsorption on a metallic surface.[289] It can be formally expressed as the ratio between the Raman cross section of the molecule adsorbed on the metal (σ_{ads}) and of the "free" molecule (σ_{Raman}):[7, 289, 298]

$$G_{chem} = \frac{\sigma_{ads}}{\sigma_{Raman}} \tag{35}$$

G_{chem} is normally considered to be $< 10^2$.[7, 289] The exact nature of the CE is still debated in the literature. However, the most established and investigated case of chemical effect is the formation of a charge-transfer state between the metal and the molecule, because this state can be resonant at the excitation laser wavelength, leading to a resonantly enhanced Raman signal.[308, 309]

The CE can be included in systems that normally do not show this SERS, as in recently reported photo-induced enhanced Raman spectroscopy (PIERS).[277]

5.2.2 The electromagnetic enhancement. The G_{em} term can reach values as high as 10^9 - 10^{10} inside a single hot-spots.[146] For instance, in the 2 nm gap of a dimer formed by two Au spheres with diameters of 50 nm, the maximum G_{em} amounts to about 3 10^9.[289, 298] However, if the G_{em} is averaged over the whole dimer surface, its value is reduced by a factor of about 300.[289, 298] For this reason, the G_{SERS} experimentally measured by averaging over a whole Au NPs substrate for SERS purposes, can reach values of about 10^7-10^8.[307, 310] These results clearly indicate also that the electromagnetic enhancement brings along a much stronger contribution than the chemical one.[311]

G_{em} can be written in a simplified form, following the so called E^4 approximation described in ref.[298], as:

$$G_{em} = \left(\frac{E_{loc}(\nu_L)}{E_0}\right)^2 \left(\frac{E_{loc}(\nu_{Raman})}{E_0}\right)^2 \tag{36}$$

where E_0 is the electric field of the incident light, ν_L and $\nu_{Raman} = \nu_L + \nu_{Stokes}$ are the laser and the Raman scattering frequencies for the vibrational mode with energy ν_{Stokes}. In the single molecule case, E_{loc}^2 refers to the value of the local field at the specific point where the molecule resides. Instead, if G_{em} refers to the average value obtained from a large number of molecules adsorbed on the SERS substrate, E_{loc}^2 should be intended as the surface average of the local field square modulus. Eq. (36) indicates that, by local field enhancement, the metallic substrate plays two roles: amplifying the light intensity at the metallic surface (first factor, excitation) and increasing the Raman scattering rate from molecules (second factor, emission), similarly to the case of modified spontaneous emission (see paragraph 5.3). The above formula can be further simplified in the zero Stokes-shift limit of the E^4 approximation, by considering $E_{loc}(\nu_L) \approx E_{loc}(\nu_{Raman})$:[302]

$$G_{em} \approx \left(\frac{E_{loc}(\nu_L)}{E_0}\right)^4 \tag{37}.$$

Clearly, this approximation is more reliable for ν_L in the visible region than in the NIR, and for low frequency vibrational modes.[10]

As a rule of thumb, the G_{em} is expected to be maximum when both the excitation and the SERS photon wavelength fall within the SPR profile of the NPs, matching the condition $\lambda_L < \lambda_{SPR} < \lambda_{Raman}$ (Wokaun's rule).[312]

Eq. (36), or its zero Stokes-shift approximation, provides a good estimation of the magnitude of the SERS electromagnetic enhancement in most situations: however they fail in predicting the polarization properties of the SERS radiation, for example the depolarization ratios, i.e. $I_\perp / I_{//}$ where $I_\perp$ and $I_{//}$ are the intensity of the Raman scattering polarized perpendicularly and parallel to the incident laser polarization.[298, 313] This stems from the approximations adopted to carry out eq. (36), which neglect some issues related to the polarization of the emitted Raman scattering and to the relative orientation of the molecule with respect to the near field.[298, 313]

As mentioned in section 5, the local field rapidly decays with distance from NPs surface as $1/r^3$.[15] Therefore the efficiency of the electromagnetic enhancement quickly drops from the surface, making SERS highly selective towards molecules located in the first layers above the surface.[314-316] For instance, the distance dependence of G_{em} can be described by considering the simple case of a metallic sphere of radius R in the quasi-static approximation as:[306]

$$\frac{G_{SERS}(d)}{G_{SERS}(0)} = \left(\frac{R}{R+r}\right)^{12} \tag{38}$$

Considering a typical Au nanosphere with R = 30 nm, the $G_{sers}(d)/G_{SERS}(0)$ goes from 100% at r=0, to 10% at r~6 nm.

5.2.3 Analyte contribution to SERS. SERS signals depend also on the properties of the analyte, since each molecule is characterized by its Raman tensor and can have different orientation relative to the metal surface.[7] For instance, the orientation of the molecule on the metal surface can change significantly the coupling efficiency with the local field,[317, 318] which are determined by specific surface selection rules.[7, 317] In general, vibrations with a change of polarizability perpendicular to the surface are enhanced, whereas Raman modes oriented parallel to the metal surface are weakly or not enhanced.[7]

Importantly, brightest Raman signals are observed when both resonant Raman and SERS occur, a condition known as surface enhanced resonant Raman scattering or SERRS. In resonant Raman scattering, the excitation frequency coincides with that of the electronic transitions in the analyte. In this case, the P_{SERS} is large because of both the G_{SERS} and the P_{Raman} terms are very large (see paragraph S7 for the full justification).[301, 319] The optical absorption bands of the analyte tell in most cases which are the optimal excitation lines to obtain both resonant Raman scattering and SERSconditions.[301, 319]

5.2.4 Applications. SERS is a well-established vibrational spectroscopic technique that simultaneously provides fingerprint recognition capabilities and extremely highly detection sensitivity, down to a single molecule level.[320, 321] These features have triggered the application of SERS in many fields like analytical and bioanalytical chemistry, chemistry, nanomedicine and biolabelling. Notably, the progress made in the engineering of the substrates, miniaturization and sensitivity of the equipment are moving SERS towards real-life applications.[7, 322] The fabrication of suitable plasmonic substrates for SERS is crucial for successful results.[7, 323-326]

5.2.4a Fundamental studies. Due to the ultra-sensitive molecular recognition allowed by SERS, single molecule Raman spectroscopy has been the subject of in depth investigations. What is a reliable proof of single molecule SERS, or what information can be extracted from single molecule Raman spectra is still debated in literature.[321]

Moreover, the possibility of quantifying the near-field intensity, has made SERS a valuable tool to investigate fundamental plasmonic issues. Since SERS is an indirect probe of the near-field intensity, wavelength scanned SERS has been used to carry out fundamental structure-to-property studies aimed to investigate the connection between the morphology of the plasmonic substrate and its near and far field properties.[303, 304, 327-330] In fact, the spectral gap between the near- and far- field properties (see pragraph 5.1.1) is a crucial issue for analytical applications. The near-field wavelength dispersion is not easily predictable on the basis of the far-field spectra in complex plasmonic substrates.[303, 304, 327-330]

5.2.4c Analytical and bioanalytical applications. SERS detection can follow two conceptually different approaches, that is direct detection[7] (in which the SERS signal is generated from the target species, see Figure 22A) and indirect detection[331] (in which the SERS signal comes from a Raman reporter molecule that is bound to a larger nanostructure which can selectively recognize the target species, see Figure 22B).

Direct detection has been exploited for biological species,[332, 333] antineoplastic drugs,[319] chemical warfare agents, toxic industrial chemicals, pesticides, food additives, and in the fields of art preservation and forensic science.[322, 334, 335]

Indirect detection is more common in complex environments, like those often encountered in the medical field.[331] Indirect detection relies on “SERS tags”: they are composed of one or more plasmonic nanoparticles, a Raman reporter molecules anchored to their surface, a stabilizing layer to prevent coalescence and fouling and one or more targeting function for the selective binding of analytes.[301, 331, 336] To achieve the largest possible brightness, these tags are built with Raman reporter capable of SERRS at the expected excitation wavelength.[301] SERS tags have been used for ionic (i.e. Hg^{2+}, Cd^{2+}, As^{3+}), biomolecular (i.e. glutathione, glucose), pathogenic (i.e. Salmonella bacteria) detection[337, 338] as well as in *in vivo* studies aimed to the identification of cancer by passive accumulation[132, 339] or active targeting of cancer markers.[339-341] Most of these studies exploit the multifunctionality of Au NPs for combined imaging techniques or guiding the therapeutic follow-up.[132, 342, 343]

5.2.4b Monitoring of chemical reactions. Real time monitoring of chemical reactions is possible by SERS, also when Au NPs do not act as substrates for the reaction.[10] Due to the SERRS effect, chemical reactions inducing changes in the electronic structure of reagents are especially easy to be monitored. SERS can be performed at specific points of a reaction environment.[344] For instance, when SERS is coupled with a microfluidic reaction chambers, reaction kinetics can be easily controlled.[344] SERS methodologies are well-suited also to study electron transfer reactions because the Au NPs both act as plasmonic substrate and metal conducting electrode.[345] On the other hand, the contribution from photothermal and photochemical effects due to SPR excitation must be considered in these experiments.[344]

5.2.5 Coherent Anti-Stokes Raman Scattering (CARS). CARS is a third order nonlinear process in which a pump and a Stokes beam at frequency ν_P and ν_{Stokes} are crossed, with a suitable geometry, in the sample (Figure 21). When ν_P - ν_{Stokes} matches the frequency of a molecular vibrational mode ($\nu_{AStokes}$), a strong anti-Stokes signal is generated at $\nu_{AStokes} = 2\ \nu_P - \nu_{Stokes}$.[346] This is a coherent process in which the generated beam is directional and governed by the phase matching conditions, opposite to normal Raman in which the scattering is normally distributed over the whole solid angle. CARS intensity depends linearly on the Stokes beam intensity and quadratically on the pump beam intensity. In practice, CARS is significantly more sensitive than normal Raman scattering also in case of molecules with intrinsically low cross section (~10^{-30} cm^2/sr), for which resonant Raman is not possible.[293, 294] By coupling CARS with SERS substrates, single molecule sensitivity was demonstrated also for this type of analytes.[294]

5.2.6 Hyper Raman scattering (HRS). HRS is a second order nonlinear process in which two incident photons are simultaneously scattered from a medium (Figure 21).[346] When high-power lasers are used, the molecular polarizability ($\vec{P}$) is not linearly dependent on the electric field and more terms have to be included in its Taylor expansion:

$$\vec{P} = \hat{\alpha}\vec{E} + \hat{\beta}\vec{E}\vec{E} + \hat{\gamma}\vec{E}\vec{E}\vec{E} + ... \quad (39)$$

where $\hat{\alpha}$ is the linar polarizability tensor, $\hat{\beta}$ and $\hat{\gamma}$ the first and second hyper-polarizabilities. Hyper-Raman scattering is due to the modulation of $\hat{\beta}$, induced by the vibrational normal modes of the molecule. This modulation gives rise to scattering components at frequency $2\nu_L - \nu_{Stokes}$ or $2\nu_L + \nu_{AntiStokes}$ where ν_L and ν_{Stokes}, $\nu_{AntiStokes}$ are the laser and vibrational mode frequencies, respectively. HRS allows the experimental investigation of specific molecular informations such as the frequency of vibrational modes not Raman or IR active.[295] However, HRS suffers of fluorescence background, low signal intensity and averaged signal over all molecules in the sample.[295, 296] Coupling molecules with Au NPs proved to be an effective way to simultaneously reduce the background signal and enhance the HRS signal, in some cases up to single molecule level.[295, 296, 347]

5.3 Fluorescence Modulation.

Fluorescence emission from a molecule[290] or a fluorescent NP (such as a semiconductor quantum dot[348] or a rare-earth luminescent nanocrystal[348, 349]) is strongly influenced by the nearby presence of Au NPs. The fluorescence cross section (σ_{Fluo}) can be expressed as the product of the fluorophore absorption cross section (σ_{Abs}) and its quantum yield (Q_{Fluo}) in free space:

$$\sigma_{Fluo} = \sigma_{Abs} Q_{Fluo} \tag{40}$$

leading to the following definition of the fluorescence enhancement factor (EF_{Fluo}):[298]

$$EF_{Fluo} = \frac{\sigma^{Au}_{Fluo}}{\sigma_{Fluo}} = \frac{\sigma^{Au}_{Abs} Q^{Au}_{Fluo}}{\sigma_{Abs} Q_{Fluo}} \tag{41}$$

The superscript "*Au*" pinpoints that the quantities refer to a fluorophore near the Au NPs. The absorption cross section may be written as:[298, 349]

$$\sigma_{Abs} \propto \omega\, Im[\alpha] \left(\frac{E_{loc}}{E_0} \right)^2 cos^2\, \theta \tag{42}$$

where α is the fluorophore linear polarizability and θ is the angle between the direction of the induced dipole moment in the fluorophore and the incident electric field $\overline{E}$. Therefore, the fluorophore absorption cross section is proportional to the square of the local field enhancement:

$$\frac{\sigma^{Au}_{Abs}}{\sigma_{Abs}} = \left(\frac{E_{loc}}{E_0} \right)^2 \tag{43}$$

However, the metal surface acts on fluorescence by influencing both the absorption cross section, and the fluorescence quantum yield (see Figure 23A).[7, 290]

Concerning Q_{Fluo}, it depends on the relative entity of radiative (Γ_{Rad}) and non radiative (Γ_{NRad}) relaxation rates as:[290, 350]

$$Q_{Fluo} = \frac{\Gamma_{Rad}}{\Gamma_{Rad} + \Gamma_{NRad}} \tag{44}$$

and in proximity of a metal surface there are additional contributions entering in the expression of Q_{Fluo}^{Au}:[290, 350]

$$Q_{Fluo}^{Au} = \frac{\Gamma_{Rad} + \Gamma_{Rad}^{Au}}{\Gamma_{Rad} + \Gamma_{Rad}^{Au} + \Gamma_{NRad} + \Gamma_{NRad}^{Au}} \tag{45}$$

From one side, the Au substrate increases the emission rate of the molecule through the Γ_{Rad}^{Au} term, by stimulating photon emission due to the local electromagnetic field enhancement, analogously to what happens to the stimulation of Raman scattered radiation (see paragraph 5.2). In fact, according to Poynting's theorem, the power (P_{Fluo}^{Au}) emitted radiatively from a fluorophore near an Au NP depends on the local field as:[351, 352]

$$P_{Fluo}^{Au} = \frac{p^2 \omega k^3}{12\pi\varepsilon_m} + \frac{\omega}{2} Im\left[\vec{p}^* \cdot \vec{E}_{loc}\right] = P_{Fluo} + \frac{\omega}{2} Im\left[\vec{p}^* \cdot \vec{E}_{loc}\right] \tag{46}$$

where $\vec{p}$ and $\vec{p}^*$ are the the quantum mechanical transition dipole of the fluorophore (treated phenomenologically as a classical dipole) and its complex conjugate.

In addition, electromagnetic energy transfer may occur from the fluorofore to the metal due to the image charges in the NP induced by the fluorophore dipole (Γ_{NRad}^{Au}).[353, 354]

Since EF_{Fluo} depends on the enhancement of the absorption cross section and on the enhancement/quenching undergone by the quantum yield, EF_{Fluo} can reach values up to 1000, but can also be <1.[290, 355]

The effects on fluorescence modulation depends on the type of fluorophore and its orientation.[290, 350, 351] Considering a good fluorophore in free space, $\Gamma_{Rad} >> \Gamma_{NRad}$ and Q_{Fluo}~1, Γ_{Rad}^{Au} will play a limited role on the quantum yield (that cannot be larger than 1). Conversely, in low quantum yield fluorophores (i.e. $\Gamma_{Rad} << \Gamma_{NRad}$ and Q_{fluo}<<1), Γ_{Rad}^{Au} can strongly increase Q_{Fluo}^{Au} with respect to Q_{Fluo}.[290, 350] Clearly, this is valid only if the weight of Γ_{NRad}^{Au} with respect to Γ_{Rad}^{Au} is negligible, otherwise Q_{Fluo}^{Au} will be smaller than Q_{Fluo}. Quenching effects prevail on the radiative enhancement in small NPs (i.e. with low local field enhancement), and at short distance (typically below 5 - 10 nm)[351] and vice versa.[7, 290, 350, 356] This leads to an optimum distance of the dye at which EF_{Fluo} is maximized, that is normally assumed to be in between 5 and 20 nm.[7, 356]

Fluorescence quenching in dyes close to Au NPs occurs on a distance longer than in conventional Forster intermolecular energy transfer processes such as FRET (fluorescence resonance energy transfer).[357] The distance dependence of quenching has been studied in the specific case of a dye attached to a 2 nm Au NP.[355, 358] The nanoparticle-dye distance was set to 7, 12 and 17 nm by using three DNA strands with different lengths as spacers (Figure 23B). The study of the photoluminescence emission, as a function of the distance showed that the quantum efficiency of energy transfer follows a $1/r^4$ distance dependence both in the case of a fluoresceine derivative and Cyanine 5 (Figure 23C). Notably, the authors showed that the gold nanoparticle does not modify the radiative emission of the dyes ($\Gamma_{Rad}^{Au} << \Gamma_{Rad}$) and hence the distance dependence measured arises only from an additional non-radiative decay pathway, due to the so called nanosurface energy transfer process (NSET).

Concerning applications, fluoresence modulation has been used in the detection of metal ions, small molecules, proteins, pathogens and mammal cells.[1] For example, β-cyclodextrin (β-CD) functionalized Au NPs can work as a FRET cholesterol sensor.[359] When fluorescein is included into the cavity of CD, its fluorescence is quenched by FRET towards the nanoparticle: due to its higher binding affinity to β-CD, cholesterol can replace fluoresceine, releasing it from the cavity and restoring its fluorescence. In this way cholesterol at nanomolar concentration can be detected.[359]

The incorporation of fluorophores as gain material in suitably engineered Au NPs assemblies (such as Au core/silica shell or porous silica capsules embedding Au NPs) makes it possible to induce resonant energy transfer processes from gain units to plasmonic NPs to compensate losses.[360, 361]

5.4 SEIRA.

In SEIRA two mechanisms contribute to enhance the IR absorption: *(i)* the electromagnetic mechanism causes an increase of the absorption cross section for the same reason discussed about fluorescence enhancement and in the same way described by eq. (42); *(ii)* the chemical mechanism corresponds to a change of the absorption cross section upon adsorption of the molecule on the metal substrate, by a similar mechanism discussed about chemical enhancement in SERS.[7, 306]

The absorption cross section for vibrational modes can be written as:[7, 362]

$$\sigma_{Abs} \propto \left| \frac{\partial \mu}{\partial Q_i} \right|^2 E^2 \cos^2 \theta \tag{47}$$

where $\left| \partial \mu / \partial q_i \right|$ is the first derivative of the dipole transition moment with respect to a normal vibrational coordinate Q_i, and θ is the angle between $\left| \partial \mu / \partial Q_i \right|$ and the oscillating electric field E. Therefore, similar to eq. (41), the increase of the molecule absorption cross section is due to the electric field enhancement generated by the plasmonic substrate, that is:

$$\frac{\sigma_{Abs}^{Au}}{\sigma_{Abs}} = \left(\frac{E_{loc}}{E_0} \right)^2 \tag{48}$$

It was suggested that surface enhanced scattering, scaling with E_{loc}^4 due to the contribution of the nearby nanoantenna, can also contribute to the IR extinction measured in ordinary SEIRA experiments.[163] This was experimentally verified by measuring the scattering of a Si tip placed in proximity of an Au dimer nanoantenna.[163] In this case, the apparent IR extinction cross section of the analyte extracted from SEIRA experiments can show a mixed dependence on E_{Loc}:[7, 163]

$$\frac{\sigma_{Ext}^{Au}}{\sigma_{Abs}} = k_1 \left(\frac{E_{loc}}{E_0} \right)^2 + k_2 \left(\frac{E_{loc}}{E_0} \right)^4 \qquad (49)$$

Experimental SEIRA enhancement factors are normally in the range 10-10^3,[362] although they can exceed 10^5 in the hot spots of optimized substrates,[363] where Fano resonance effects involving the interference of a broadband plasmon with the narrowband vibration from adsorbates are possible.[364, 365]

SEIRA is most efficient within 5 nm of the surface, where the effect of the two mechanisms of enhancement is larger, since the absorption enhancement decays as $1/r^6$, where r is the distance between analyte and metal surface.[7]

In SEIRA the local field enhancement is required at IR frequencies, therefore best hot spots are achieved at the junction between linear Au nanoantennas with high aspect ratio (up to 10) and micrometer length, using illumination with light that is polarized parallel to the antenna axis (Figure 24A-B).[363, 365] Interestingly, appropriate engineering of the Au nanoantennas allows simultaneous SERS and SEIRA on the same substrate, by endowing it with both visible and infrared SPRs (Figure 24A).[366]

As for applications, SEIRA has been used for the characterization of ultrathin films in several contexts, to study catalytic reactions and electrochemical processes with improved sensitivity, and in cultural heritage studies.[7, 306, 367]

Recently, the photothermal-induced resonance imaging (PTIR) technique emerged for the investigation of SEIRA with 30-100 nm of spatial resolution.[368] In PTIR, samples are illuminated with a tuneable IR laser in a total internal reflection configuration. The absorption of laser light by the sample results in local heating, sample expansion, and thus in a mechanical excitation which can be detected with an AFM cantilever in contact with the sample (Figure 24C). AFM tip displacement will be proportional to the absorbance of the probed area at each specific IR wavelength used. Therefore, PTIR provides an IR absorption spectrum, directly comparable with IR spectral libraries, but collected with 30-100 nm of spatial resolution, that is compatible with plasmonic features of several Au nanostructures acting as SEIRA substrates.[368, 369]

5.5 Enhanced optical absorption and photovoltaic applications.

Surface enhanced absorption is possible in molecules with electronic transitions in the same spectral range of the SPR in the Au NPs (see eq. (42)). Coupling between the LSP and the electronic transition in molecules was also observed.[370, 371] It was recently shown that molecules electronic structure is modified after adsorption on the metal surface, with spectral changes in their absorption bands far from the SPR frequency.[291]

The enhancement of light absorption in materials near Au NPs surface find application also in the field of photovoltaics.[372, 373] Conventional silicon or bulk heterojunction solar cells are fabricated in order to meet two opposite requirements, that are good absorption of the sunlight and efficient collection of the generated charge carriers. An increase of the cell thickness would improve the former but reduce the latter since charge carriers generated far from the p-n junction (in Si cells) or the acceptor-donor junction (in bulk heterojunction cells) have higher probability of charge recombination. Improving the absorption efficiency of the photovoltaic layer would allow one to fabricate thinner cells, with a reduction of the production costs and an increase of charge carrier collection efficiency. Plasmonic nanoparticles can be used to this aim, following two different schemes (Figure 25):[372, 374-377]

(i) Light scattering. Metal nanoparticles placed above the photovoltaic layer drive the sunlight preferentially into the photovoltaic layer itself, introducing an angular spread that increases the effective light path and therefore the absorption.

(ii) Light concentration. Metal nanoparticles are embedded in the photovoltaic layer: sunlight absorption is increased due to the intense local field present at the surface of the metal nanoparticles.

6. Other applications and advanced phenomena.

6.1 Optical trapping and manipulation.

Optical forces and torques stem from the conservation of linear and angular momentum during the light-matter interaction.[166] Such mechanical effects of light are the enabling principles of the so-called *optical tweezers* (OT),[166, 378] tools based on highly focused laser spots that can trap and manipulate particles over a broad size range, from atoms to cells. Capable of applying and detecting extremely small forces (at the femtonewton range) and torques, OT find applications in many research fields ranging from life sciences, to spectroscopic sensing, and quantum technologies.[378] In this context, the plasmonic response of gold has been exploited for two main class of OT applications: *(i)* optical trapping and manipulation of colloidal gold nanoparticles,[379] aggregates,[107, 380] and composites,[381, 382] where the particles large polarizability as well as their localized plasmonic response enhances optical forces; *(ii)* the so-called *plasmonic tweezers*,[383] where particles are trapped by the enhanced near-fields associated with the plasmonic response of gold nanostructures on a substrate.[384]

6.1.1 Optical trapping of Au NPs. Optical trapping of colloidal gold nanoparticles is generally achieved by tuning the light on the long wavelength side of any plasmon resonance, i.e., typically in the near infrared (NIR) where the optical response of individual metal nanoparticles is dictated by the free-electron plasma resulting in an increased dipolar polarizability.[385] Thus, a ten-fold enhancement of optical trapping forces is measured on individual gold nanoparticles with respect to, e.g., polystyrene ones.[378, 386] Particle shape has a key role in determining the optomechanical interaction in plasmonic system as can modify the optical response on a broad spectral region.[387] Optical trapping, alignment, and rotation of gold nanorods,[388-390] and nano-aggregates[380, 391] has been achieved using a single-beam linearly polarized OT in the NIR. However, when the light is nearly-resonant with the particle SPR, trapping forces are overwhelmed by radiation pressure and particles can be pushed along the laser beam propagation axis.[392, 393] Thus, the frequency dependence of the plasmon resonance yields a frequency dependent plasmon-enhanced radiation force that can be exploited for optical force deposition,[394] to sort gold nanoparticles of different sizes,[392] or to create controlled SERS active regions, such as in a microfluidic environment.[393] Noteworthy, optical trapping of colloidal metal particles can be often accompanied by heating effects because of light absorption,[380, 395-397] even at wavelengths far from plasmon resonances that can be exploited for optical injection in living cells.[398]

In Raman tweezers (RT), OT and Raman spectroscopy are performed with the same laser line and optical set up, to collect Raman signals from the trapped object (Figure 26).

6.1.2 Plasmonic tweezers with Au NPs. Plasmonic tweezers based on Au NPs exploit the enhanced field associated with localized hot spots generated by gold structures (pads, holes, nanoantennas) fixed on a substrate.[384, 399] The localized hot spots provide three-dimensional optical trapping at the nanoscale.[384, 399] Changing the shape and size of the nanostructures results in a wide tunability of the optomechanical interaction. This enables the optical trapping and SERS up to single molecule level.[400]

6.2 Plasmonic chiroptical effects.

Any object is chiral if its image in a plane mirror cannot be brought to coincide with itself and, consequently, chiral objects can have left or right handedness.[401] This means that the inversion symmetry is broken, i.e. the object does not have a mirror and rotation-reflection symmetry.[402] In nature, chirality is associated to chiroptical effects, due to the fact that the refractive index and the extinction coefficient of chiral objects (or enantiomers) differ for left- and right-hand circularly polarized light. The difference in refractive index causes a rotation of the plane of linearly polarized light (optical rotation or optical activity), while the difference of extinction coefficient causes a difference in transmission for left and right-hand circularly polarized light (circular dichroism or CD).[401] When optical rotation is probed as a function of wavelength, it is called optical rotatory dispersion (ORD).

Optical rotation (OR) and CD also have a nonlinear optical counterparts such as SHG-OR and SHG-CD, although nonlinear chiroptical effects are sensitive to different structural parameters and selection rules.[401]

Chiroptical effects are at the basis of several applications such as optical modulation, the characterization of molecular enantiomers (biomolecules, organic compounds, etc.), and have the potential of inducing asymmetric synthesis and catalysis (chiral photochemistry).[401, 402]

6.2.1 Intrinsic chiroptical effects in Au NPs. Chiroptical effects in Au NPs can have different origin:[401]

(i) The kink atoms of high Miller index surfaces, such as one at which the (001), (011), and (111) surfaces of a cubic lattice intersect (not related to the SPR).

(ii) The relaxation of surface atoms due to surface patterning with adsorbed molecules (chiral footprinting, not related to the SPR).

(iii) The shape or the assembly of Au NPs into chiral geometry. In fact, the same symmetry requisites of molecules showing chiroptical effects are valid also for plasmonic nanostructures.[402] However, chiroptical effects in molecules are small because the chiral arrangement of molecular bonds occurs over a much shorter distance than the helical pitch of circularly polarized light. Instead, the shape or assembly of Au NPs can be optimized to increase the chiroptical effects several orders of magnitude higher than those for common biomolecules,[403] for instance by increasing the chiral pitch of the material to match that of circularly polarized light.[401] Typical chiral shapes are 2D and 3D spirals, also obtained by the superposition of achiral objects (Figure 27). In particular, chirality can be obtained from the assembly of achiral Au NPs onto chiral molecules and nanostructures, such as organic fibers or DNA scaffolds.[404, 405]

This is exploitable for designing elegant chiroplasmonic sensors. For instance, Au-Ag NPs conjugated with aptamers were assembled into chiral structures capable of intense CD signals only when the HER2 antigen of specific cancer cells is present, due to the bioaffinity for the aptamer coating.[406]

On the other hand, chiroptical effects can lead to negative refractive index, which is of interest for the realization of metamaterials (i.e. materials with optical properties not found in nature) and the related wide range of possible photonic applications.[401]

6.2.2 Enhancement of chiroptical effects in nearby molecules. Au NPs can increase the chiroptical effects in nearby molecules in several ways. In general, the chiroptical effects are related to the optical chirality C_{co}:[403]

$$C_{co} = -\frac{\varepsilon_0 \omega}{2} Im\left[\vec{E}_{loc}{}^* \cdot \vec{B}_{loc}\right] \tag{50}$$

Thus, the chiroptical effects scales linearly with the local electric field enhancement, and chiral enhancement in a molecule close to the Au NPs can be expressed as:[354, 403]

$$\hat{C} = \frac{C_{co}\left(E_{Loc}, B_{Loc}\right)}{C_{co}\left(E_0, B_0\right)} \tag{51}$$

It was calculated that C_{co} of molecules near chiral Au NPs can be about 20 times higher than in the absence of the NPs (Figure 27).[403] Therefore, the same plasmonic NPs possessing intrinsic chiroptical properties can also enhance the chiroptical effects of nearby molecules, in principle allowing the identification of enantiomers with higher sensitivity,[403] or significantly increasing the enantiomeric excess of direct asymmetric synthesis and catalysis.[401]

A more detailed expression can be used for C_{co}:[354]

$$C_{co} = a_{co}\, Im\left[\left(\hat{P}\vec{\mu}_{12}\right) \cdot \vec{m}_{21}\right] + b_{co} F\left(\vec{\mu}_{12}, \vec{m}_{21}\right) \tag{52}$$

where $\vec{\mu}_{12}$ and $\vec{m}_{21}$ are the electric and magnetic dipole moments of a molecule, a_{CO}, b_{CO} and $F\left(\vec{\mu}_{12}, \vec{m}_{21}\right)$ are coefficients depending on the geometry, material and incident light frequency, $\hat{P}$ is the electric-field enhancement matrix. For increasing distance between molecule and NP, $\hat{P}$ tend to unit matrix and b tend to 0. The first term in eq. (52) shows that $\hat{P}$ can change the angle between $\hat{P}\vec{\mu}_{12}$ and $\vec{m}_{21}$, which allows the creation of a non zero CD signal also in molecules with a mirror-symmetry plane and orthogonal dipole moments.[354] This means that the interaction with a NP may lower the symmetry of a molecule and create a CD signal. The second term in eq. (52) accounts for mutual interactions between molecules and NP, such as the chiral currents inside a NP induced by the dipole of a chiral molecule. Both the first and second term of eq. (52) must be considered to properly reproduce the observed Fano resonance effects in CD spectra.[354]

6.3 Magneto-plasmonic effects.

Literature refers to magneto-plasmonics in Au NPs in two distinct cases:[407]

(i) when magnetic and plasmonic properties are combined in a single nanosystem, resulting in additive magnetic-plasmonic effects, without reciprocal influence on the magnetic or plasmonic responses;

(ii) when the magnetic properties influence the plasmonic response or viceversa, resulting in new magneto-plasmonic performances or phenomena.

A consequence of this definition is that "magnetic-plasmonic" devices require the combination of a ferro-, ferri- or para-magnetic material to a plasmonic one, whereas "magneto-plasmonic" phenomena can in principle be observed also in traditionally dia-magnetic plasmonic materials such as pure Au. Nonetheless, external magnetic fields must be applied to enable magnetoplasmonic activity, thus the presence of "magnetic" elements such as Fe, Co or Ni is generally preferred to obtain stronger or new combined effects.[407] On the other hand, magnetic materials have damped plasmon resonance and limited chemical stability in ordinary operating conditions,[36] which justifies the combination with good plasmonic materials such as Au to obtain appreciable optical properties.[35, 130, 407]

Magnetic-plasmonic NPs are exploited for a variety of applications taking advantage of the coexistence of the two effects. For instance, magnetism allows localization of NPs in a specific area for collection and enhanced detection of analytes, for localized drug delivery or for realization of remotely-assembled and reconfigurable plasmonic devices, including arrays of SERS substrates.[407-409] Magnetism is also exploited in nanomedicine for multimodal imaging and therapeutic properties to Au NPs.[132, 410-412]

Magneto-plasmonics is an emerging research field including some well established physical phenomena such as magneto-optic Kerr effect (MOKE) and the Faraday effect (Figure 28A), and new phenomena that are still under debate such as photoswitchable magnetism.[407] MOKE consists in the rotation of the polarization plane of light reflected from a magnetized material.[346] The Faraday effect is the equivalent of MOKE for transmitted light.[346] The rotation of the plane of polarization is linearly proportional to the component of the magnetic field in the direction of light propagation. Faraday effect can be seen as a magnetic field induced circular birefringence, meaning that left and right circularly polarized waves propagate at slightly different speeds in the medium.[346]

Essential devices in photonics technology such as light polarization rotators and nonreciprocal optical isolators are based on MOKE or Faraday rotation, and magnetoplasmonics is a promising route to bring these devices to the nanoscale.[413] Besides, magneto-optical SPR (MOSPR) sensors, which employ the MOKE signal as the sensing magnitude instead of the reflectivity, theoretically allows much higher sensitivity than the pure plasmonic equivalents for gas and biosensing detection.[407, 408] As discussed below, the MOKE signal is enhanced when the probe frequency is in resonance with the LSP modes, and the SPR is influenced by the refractive index of the surroundings (see paragraphs 2.1 and 4.1), thus providing the sensing principle of the MOSPR sensors.[414]

The physics of magneto-plasmonics can actually be divided in its two parts. Concerning the magnetic response, magneto-optical activity is observed because the optical constant of any material, that is a tridimensional tensor in the general case, becomes non-diagonal when an external magnetic field (B) is present. In case of an isotropic material like Au, ε is:[407]

$$\hat{\varepsilon}(B) = \begin{pmatrix} \varepsilon_x & k_1 \Pi_z & k_1 \Pi_y \\ -k_1 \Pi_z & \varepsilon_y & -k_1 \Pi_x \\ -k_1 \Pi_y & k_1 \Pi_x & \varepsilon_z \end{pmatrix} \tag{53}$$

where $k_1\Pi_i$ are the magneto-optical constants of the material and Π_i are the B-dependent components. In dia- and para-magnetic materials, Π_i are proportional to B, while in ferro-magnetic materials Π_i are set by material magnetization and are orders of magnitude larger than those of dia- and para-magnetic materials, thus justifying the use of ferromagnetic materials for magnetoplasmonics.[407]

Like all noble metals, Au is dia-magnetic, and MO effects can be observed only for large enough applied B. In particular, MO effects are possible when the SPR is excited by circularly polarized light in the presence of a static magnetic field parallel to the direction of light propagation.[407, 415, 416]

The MO effect can be well described by considering a Drude model and the Lorentz force induced by the B field on the circular collective movement of conduction electrons under circularly polarized light illumination, that for the single electron is:[415, 416]

$$\vec{F}_L = -e\vec{E}_0 - e\vec{v}_e \times \vec{B} \tag{54}$$

with e the electron charge and v_e the electron speed. The effect is a collective circular charge motion more or less confined depending on the helicity of the circular plasmonic mode, that correspond to splitting, i.e. to a positive or negative shift of the SPR frequency roughly proportional to B:[415]

$$\omega_{SPR}^{Au}(B) \approx \omega_{SPR}^{Au}(B=0) \pm \frac{e}{2m_e} B \tag{55}$$

where the sign depends on light helicity (Figure 28B). The entity of this shift is of about 0.01 nm per applied Tesla, observable by ordinary magnetic circular dichroism (MCD) spectroscopy.[415]

On the other hand, MO effects also benefit of the plasmon resonance and the associated local field enhancement. For instance, when linear p-polarized light is reflected from a sample, it is possible to express the MOKE performance by the complex Kerr rotation (Φ):[407]

$$\Phi = \frac{r_{ps}}{r_{pp}} \tag{56}$$

where r_{pp} and r_{ps} are the polarization conversion fraction of p- and s- polarized light, respectively.

r_{pp} scales with the reflectivity of the material, meaning that at the SPR, where light absorption is maximum, also the MOKE performance is larger. r_{ps} scales with the magneto-optical ability of the material, and can be expressed as:[407]

$$r_{ps} \propto \left\langle E_p E_s \right\rangle k_1 \Pi_i d \qquad (57)$$

where $\left\langle E_p E_s \right\rangle$ is the mean value of the two components of the electric field, and d is the thickness of the MO material. The $\left\langle E_p E_s \right\rangle$ term is greatly increased when the magnetic material is in proximity of a plasmonic structure and incident light is in resonance with its LSP modes.

Therefore, the excitation of a LSP increase the MOKE performance both by decreasing reflectivity and increasing the magneto-optical term.[407]

There are several examples of surface plasmon resonance-enhanced magneto-optics (SuPREMO) in composite magnetic/plasmonic nanosystem.[407, 408, 417] Plasmon-enhanced Faraday rotation was observed in Au-coated maghemite (γ-Fe_2O_3) NPs and attributed to the near-field enhancement resulting from the spectral overlap of the surface plasmon resonance in the gold with the electronic transition in maghemite.[417] SPR enhancement of the MO activity was observed also in Au/Co/Au nanosandwiches, Au/CoPt/Au nanodisks, in colloidal Au-Fe_3O_4 NPs.[407, 408] Interestingly, the tunability of the SPR by acting on Au NPs structure is exploitable also for the spectral tunability of the MO effects.

An open point in magneto-plasmonic is the possibility of using the SPR to change the magnetic properties of NPs. For instance, it was observed that a reversible optically-induced variation of the magnetic moment was possible in Fe-doped Au NPs, opening interesting perspectives for the realization of photoswitchable nanomagnets that can be controlled and monitored by light.[418] One major problem of Au:Fe alloys is the presence of segregated domains of the two elements, with no "true" alloying taking place.[418] Indeed, these studies requires the coupling of magnetic and plasmonic elements at the atomic level and have been limited in the past by the lack of effective ways for the production of stable Au-X alloy NPs, where X is a magnetic element such as Fe, Co or Ni, that have been developed only recently.[128, 130] Overall, due to the limited number of nanosystems with magnetic and plasmonic properties coexisting in the same phase, such as the recently developed Fe-doped plasmonic nanoalloys,[128, 130, 131, 409] the realm of magnetoplasmonic effects still has to be fully investigated.

6.4 Nonlinear optical applications.

Au NPs have highly polarizable electrons, which ensure a strong nonlinear optical (NLO) response, i.e. a large nonlinear susceptibility.[13] However, by definition, NLO depends on light intensity and requires high fields,[346] which poses the problem of heating and NPs degradation.[238] Besides, the nonlinear response of Au NPs cannot be predicted from the knowledge of the linear optical constant alone.[419] Therefore, several aspects related to plasmonic NLO (PNLO) are still under debate.

There are two types of PNLO:

(i) PNLO effects originated from the Au NPs, i.e. depending on the electric field inside the NPs;

(ii) PNLO effects originated by nearby structures, i.e. depending on local field enhancement at electromagnetic hot spots. To date, these are less frequent and mostly concern the effects mentioned in section 5.

6.4.1 Optical Kerr effect (OKE). The OKE is a 3rd order phenomenon consisting in the light intensity dependent variation of the refractive index of a material. Au NPs have large third-order susceptibility ($\chi^{(3)}$), especially at frequencies close to the SPR. When embedded in dielectric matrices, Au NPs are of interest in ultrafast all optical switching devices based on OKE.[420, 421] The magnitude of the nonlinear response varies with size and shape as well as volume fraction of metal nanoclusters in the dielectric matrix.[420, 421] Three mechanisms contribute to $\chi^{(3)}$:[422] (*i*) a fast mechanism (~500 fs) due to electron-electron scattering after SPR excitation, driving to the electrons thermalization, (*ii*) a contribution from interband transition, which occurs on the same time scale of the former and (*iii*) an hot electrons mechanism on a time scale of ps or longer. Only the first two mechanisms are fast enough for optical switching applications.

6.4.2 Multiple harmonic generation (MHG). In MHG, two, three, or more photons with same frequency are simultaneously annihilated by exciting the material to a virtual electronic state, from which it decays generating a single photon with frequency sum of the incoming ones, resulting in second, third or higher harmonic generation. Au NPs exhibit significant MHG conversion efficiencies,[423] with best performances achieved for excitation or emission wavelength resonant with particles SPR.[419] In fact, Miller's rule predicts that the nonlinear conversion is maximum when the linear optical properties exhibit resonances either at the fundamental or the harmonic frequencies.[346] As for the linear plasmonic response, also MHG in Au NPs can be qualitatively described by the anharmonic oscillator model.[419]

Several advances were recently reported about the engineering of Au NPs for MHG. For instance, SHG is a second order process occuring in objects without an inversion center, and is subjected to parity and angular momentum conservation rules.[346] Therefore, optimal SHG was observed in coupled Au NPs satisfying three criteria (Figure 29A):

(i) having multiple narrow SPRs at both the excitation and SH wavelengths;

(ii) allowing a significant spatial overlap of the local fields at the wavelengths of interest;

(iii) having optimized geometry and symmetry for dipole-allowed SH emission.[424]

Plasmonic Fano resonances, due to reduced linewidth, are also highly attractive for enhancing PNLO.[419] For instance, spectrally tunable SHG was measured in Au NPs arrays supporting Fano resonances at different frequency depending on particle size and separation.[425]

The local field enhancement in Au NPs hot spots justified also a series of studies where traditional NLO materials are coupled to the plasmonic substrate. According to some authors, the SHG of a NLO material can be locally enhanced by 4–6 orders of magnitude.[426] For instance, a ZnO nanowire coupled to the hot-spots of a gold pentamer oligomer showed SHG conversion efficiency of $3 \cdot 10^{-5}$ %, that is 1700 times larger than outside the hot-spot and among the highest values for this type of objects.[427]

However, other authors showed with quantitative arguments that, in several cases, MHG is originated with higher efficiency by the Au NPs when a NLO material is placed in their proximity.[13, 419] In a series of experiments with electron-beam lithography deposition of standard NLO materials such as lithium niobate ($LiNbO_3$) or indium tin oxide (ITO) at the hot spots of Au nanoantennas, the observed THG signal enhancement was related to changes in the linear optical properties of the Au NPs without appreciable contributions from the NLO crystals.[13, 423]

Due to the intrinsic low background, MHG phenomena are promising for bioimaging, biolabelling and, in particular, for sensing. For instance, THG spectra are narrower than the linear plasmon resonance, due to the third-order dependence of the signal on the incident light intensity (Figure 29B).[428] This corresponds to a larger sensitivity to local changes in the refractive index as compared to the commonly used linear localized surface plasmon resonance sensing, allowing detection of refractive index changes as small as 10^{-3}.[428] Similarly, SHG is proportional to the square of the laser intensity.[346] In a double resonance plasmonic SHG systems, a FOM* ~ 40 was found, much higher than single-particle SPR-based platforms.[424] A SHG-based plasmonic nanoruler was also proposed as a possible method for measuring nanoscale distances with high spectral accuracy and signal-to-noise ratio.[429]

Although SHG is not allowed in isotropic dispersions of non-centrosymmetric particles, a weak frequency doubling phenomenon is still possible, called hyper Rayleigh scattering.[430] This is a non-linear second-order light scattering that relies upon the fluctuations of the density or orientation of nanoparticles, which instantaneously break the centrosymmetry of isotropic media as liquid solutions and create conditions of net frequency doubling.[346] This is exploitable for detection of analytes which promotes the assembly of centrisymmetric NPs into non-centrosymmetric aggregates, such as Au NPs functionalized with antibodies that conjugate a target antigen into a fractal structure.[430]

6.4.3 Multiphoton absorption induced photoluminescence (MPL). In MPL, multiple photons are absorbed by the Au NPs, generating an electron-hole couple that decays radiatively. MPL is of possible interest for bioimaging.[431] The observed photoluminescence spectra are usually broad and are not correlated with the SPR.[431] However, MPL is related to Au band structure, explaining why two and four photons PL processes are more efficient than three and five photons processes.[432] 2PPL in gold is the result of two sequential single-photon absorption steps mediated by a real state, where the first photon excites an electron via an intraband transition within the sp conduction band, while the second photon excites an electron from the d band to recombine with an sp hole in the conduction band (Figure 29C).[432] In 4PPL, the first step is a three-photon sp → sp direct interband transition followed by a single-photon transition. Compared to 2PPL, the 4PPL is favoured with ultrashort (< 100 fs) laser pulses, providing a way to switch between the two mechanisms by acting on pulse duration.[432]

Although 2PPL is a third order effect, associated with two-photon absorption, whereas SHG is a second order nonlinear optical effect, both depends on the second power of laser intensity, making the discrimination of the two contributions nontrivial.[117, 433]

6.4.4 Optical limiting (OL). In OL materials, their transmittance decreases rapidly when incident light exceeds a threshold fluence, due to the increased light absorption and/or scattering (Figure 29D).[346] Au NPs are excellent optical limiters due to free carriers multiphoton absorption and nonlinear scattering.[434-436] Independent of the mechanism, all the investigations on optical limiting properties of Au NPs pointed out the following aspects:[434-436] *i*) the OL performances are amongst the best ever measured; *ii*) big nanoparticles are better optical limiters than small ones *iii*) nanoparticles loose limiting efficiency after few laser pulses due to their fragmentation, that is more rapid and has a lower threshold when particles size is big; *iv*) nanoparticles have appreciable OL performances only at frequencies close to the SPR or interband transitions. In several cases, the optical limiting properties were enhanced by blending Au NPs with organic molecules.[435] An extremely long durability under laser irradiation was observed in case of Au NPs blended with zinc phthalocyanines (PCs). The origin of the enhanced OL performances resides in the ability of the Au NPs to self – heal during the laser pulse irradiation by interaction with the PCs (Figure 29E), via a mechanism mediated by SPR absorption and photoinduced melting of NPs aggregates.[435] The Au NPs/PCs blend represents the first reported example of a functional nanomaterials that self – heals during use.[14, 435]

Conclusions.

Exploited since centuries for their intense coloration, in the last two decades Au NPs have been the subject of a growing number of scientific investigations related to their SPR properties. Plasmon physics is rich and intriguing, and LSPs of Au NPs enter in numberless applications. Although the “traditional” research about optical sensing, SERS and photothermal phenomena are the lion’s share of literature, new fields are rapidly emerging such as nonlinear optics, optical trapping, chiroptical effects, magnetoplasmonics and plasmon enhanced catalysis. At the same time, the control over the SPR of Au NPs is no more restricted to shape, size, assembly and surface chemistry, but is now expanding towards new frontiers such as alloying. With the continuous progress in modelling and understanding of plasmon physics, and a parallel advancement in the realization of gold NPs with precisely controlled structure and composition, in the next future one can easily expect a further increase in the number of technological and scientific applications.

Acknowledgments.

R. Saija is gratefully acknowledged for useful discussions. V.A. acknowledges financial support from the University of Padova (PRAT no. CPDA114097/11 and Progetto Strategico STPD11RYPT_001).

Bibliography.

1) K. Saha, S. S. Agasti, C. Kim, X. Li and V. M. Rotello, *Chem. Rev.*, 2012, 112, 2739-2779.

2) E. Di Fabrizio, S. Schlücker, J. Wenger, R. Regmi, H. Rigneault, G. Calafiore, M. West, S. Cabrini, M. Fleischer and N. F. Van Hulst, *Journal of Optics,* 2016, 18, 063003.

3) C. J. Murphy, A. M. Gole, J. W. Stone, P. N. Sisco, A. M. Alkilany, E. C. Goldsmith and S. C. Baxter, *Acc. Chem. Res.,* 2008, .

4) L. A. Austin, B. Kang and M. A. El-Sayed, *Nano Today,* 2015, 10, 542-558.

5) P. Ghosh, G. Han, M. De, C. K. Kim and V. M. Rotello, *Adv. Drug Deliv. Rev.,* 2008, 60, 1307-1315.

6) N. S. Abadeer and C. J. Murphy, *The Journal of Physical Chemistry C,* 2016, 120, 4691-4716.

7) M. Jahn, S. Patze, I. J. Hidi, R. Knipper, A. I. Radu, A. Mühlig, S. Yüksel, V. Peksa, K. Weber and T. Mayerhöfer, *Analyst,* 2016, 141, 756-793.

8) J. N. Anker, W. P. Hall, O. Lyandres, N. C. Shah, J. Zhao and R. P. Van Duyne, *Nat. Mater.*, 2008, 7, 442-453.

9) X. Chen, G. Cabello, D. Wu and Z. Tian, *Journal of Photochemistry and Photobiology C: Photochemistry Reviews,* 2014, 21, 54-80.

10) S. Schlücker, *Angewandte Chemie International Edition,* 2014, 53, 4756-4795.

11) E. S. Cho, J. Kim, B. Tejerina, T. M. Hermans, H. Jiang, H. Nakanishi, M. Yu, A. Z. Patashinski, S. C. Glotzer and F. Stellacci, *Nature materials,* 2012, 11, 978-985.

12) R. J. Barsotti, M. D. Vahey, R. Wartena, Y. Chiang, J. Voldman and F. Stellacci, *Small,* 2007, 3, 488-499.

13) M. Hentschel, B. Metzger, B. Knabe, K. Buse and H. Giessen, *Beilstein journal of nanotechnology,* 2016, 7, 111-120.

14) V. Amendola and M. Meneghetti, *Journal of Materials Chemistry,* 2012, 22, 24501-24508.

15) S. A. Maier, *Plasmonics: fundamentals and applications*, Springer, 2007.

16) B. Luk'yanchuk, N. I. Zheludev, S. A. Maier, N. J. Halas, P. Nordlander, H. Giessen and C. T. Chong, *Nature materials,* 2010, 9, 707-715.

17) E. C. Dreaden, A. M. Alkilany, X. Huang, C. J. Murphy and M. A. El-Sayed, *Chem. Soc. Rev.,* 2012, 41, 2740-2779.

18) V. Amendola and M. Meneghetti, *Phys. Chem. Chem. Phys.*, 2009, 11, 3805-3821.

19) M. C. Daniel and D. Astruc, *Chem. Rev.,* 2004, 104, 293-346.

20) P. Colomban, *Journal of Nano Research,* 2009, 8, 109-132.

21) I. Freestone, N. Meeks, M. Sax and C. Higgitt, *Gold Bulletin,* 2007, 40, 270-277.

22) F. E. Wagner, S. Haslbeck, L. Stievano, S. Calogero, Q. Pankhurst and K. Martinek, *Nature,* 2000, 407, 691-692.

23) L. Hunt, *Gold Bulletin*, 1976, 9, 134-139.

24) A. Ruivo, C. Gomes, A. Lima, M. L. Botelho, R. Melo, A. Belchior and A. P. de Matos, *Journal of Cultural Heritage,* 2008, 9, e134-e137.

25) J. Spadavecchia, E. Apchain, M. Albéric, E. Fontan and I. Reiche, *Angewandte Chemie International Edition*, 2014, 53, 8363-8366.

26) M. Blosi, S. Albonetti, F. Gatti, G. Baldi and M. Dondi, *Dyes and Pigments,* 2012, 94, 355-362.

27) M. Faraday, *Philosophical Transactions of the Royal Society of London*, 1857, 147, 145-181.

28) G. Mie, *Ann. Phys.*, 1908, 1, 377-445.

29) C. Kittel and P. McEuen, *Introduction to solid state physics,* Wiley New York, 1996.

30) U. Kreibig and M. Vollmer, *Optical Properties of Metal Clusters*, Springer, Berlin, 1995.

31) P. Biagioni, J. Huang and B. Hecht, *Reports on Progress in Physics,* 2012, 75, 024402.

32) J. Zuloaga and P. Nordlander, *Nano letters*, 2011, 11, 1280-1283.

33) M. A. Kats, N. Yu, P. Genevet, Z. Gaburro and F. Capasso, *Optics express,* 2011, 19, 21748-21753.

34) K. M. Mayer and J. H. Hafner, *Chem. Rev.*, 2011, 111, 3828-3857.

35) V. Amendola, R. Sajia, O. M. Maragò and A. Iatì, *Nanoscale*, 2015, 19, 8782-8792.

36) M. G. Blaber, M. D. Arnold and M. J. Ford, *J. Phys. Cond. Matt.,* 2010, 22, 143201.

37) C. F. Bohren and D. R. Huffman, *Absorption and scattering of light by small particles*, Wiley-Interscience, New York, 1983.

38) A. J. Haes, C. L. Haynes, A. D. McFarland, G. C. Schatz, R. P. Van Duyne and S. Zou, *MRS Bull,* 2005, 30, 368-375.

39) Y. Xia and N. J. Halas, *MRS Bull,* 2005, 30, 338–348.

40) M. D. Arnold and M. G. Blaber, *Opt. Expr.,* 2009, 17, 3835-3847.

41) L. Novotny and N. Van Hulst, *Nature Photonics,* 2011, 5, 83-90.

42) K. L. Kelly, E. Coronado, L. L. Zhao and G. C. Schatz, *J. Phys. Chem. B,* 2003, 107, 668–677.

43) V. Amendola and M. Meneghetti, *J. Phys. Chem. C,* 2009, 113, 4277-4285.

44) J. Olson, S. Dominguez-Medina, A. Hoggard, L. Wang, W. Chang and S. Link, *Chem. Soc. Rev.,* 2015, 44, 40-57.

45) C. Sönnichsen, T. Franzl, T. Wilk, G. von Plessen, J. Feldmann, O. Wilson and P. Mulvaney, *Phys. Rev. Lett.,* 2002, 88, 077402.

46) J. A. Scholl, A. García-Etxarri, A. L. Koh and J. A. Dionne, *Nano letters,* 2013, 13, 564-569.

47) J. A. Scholl, A. L. Koh and J. A. Dionne, *Nature,* 2012, 483, 421-427.

48) O. Nicoletti, F. de La Peña, R. K. Leary, D. J. Holland, C. Ducati and P. A. Midgley, *Nature,* 2013, 502, 80-84.

49) A. C. Atre, B. J. Brenny, T. Coenen, A. García-Etxarri, A. Polman and J. A. Dionne, *Nature nanotechnology,* 2015, 10, 429-436.

50) A. Losquin, L. F. Zagonel, V. Myroshnychenko, B. Rodríguez-González, M. Tencé, L. Scarabelli, J. Förstner, L. M. Liz-Marzán, García de Abajo, F Javier and O. Stéphan, *Nano letters,* 2015, 15, 1229-1237.

51) S. Link and M. A. El-Sayed, *Annu. Rev. Phys. Chem.,* 2003, 54, 331-366.

52) C. Voisin, N. Del Fatti, D. Christofilos and F. Vallée, *The Journal of Physical Chemistry B,* 2001, 105, 2264-2280.

53) D. J. Griffiths and Reed College, *Introduction to electrodynamics,* prentice Hall Upper Saddle River, NJ, 1999.

54) C. Sönnichsen, T. Franzl, T. Wilk, G. Von Plessen and J. Feldmann, *New Journal of Physics,* 2002, 4, 93.

55) A. Alabastri, S. Tuccio, A. Giugni, A. Toma, C. Liberale, G. Das, F. D. Angelis, E. D. Fabrizio and R. P. Zaccaria, *Materials,* 2013, 6, 4879-4910.

56) S. Link and M. A. El-Sayed, *J Phys Chem B,* 1999, 103, 4212-4217.

57) K. O. Aruda, M. Tagliazucchi, C. M. Sweeney, D. C. Hannah, G. C. Schatz and E. A. Weiss, *Proc. Natl. Acad. Sci. U. S. A.,* 2013, 110, 4212-4217.

58) Y. Tang and M. Ouyang, *Nature materials,* 2007, 6, 754-759.

59) X. Li, D. Xiao and Z. Zhang, *New Journal of Physics,* 2013, 15, 023011.

60) M. L. Brongersma, N. J. Halas and P. Nordlander, *Nat. Nanotech.,* 2015, 10, 25-34.

61) X. Meng, L. Liu, S. Ouyang, H. Xu, D. Wang, N. Zhao and J. Ye, *Adv Mater,* 2016, .

62) M. Perner, P. Bost, U. Lemmer, G. Von Plessen, J. Feldmann, U. Becker, M. Mennig, M. Schmitt and H. Schmidt, *Phys. Rev. Lett.,* 1997, 78, 2192.

63) E. Dulkeith, T. Niedereichholz, T. Klar, J. Feldmann, G. Von Plessen, D. Gittins, K. Mayya and F. Caruso, *Physical Review B,* 2004, 70, 205424.

64) E. M. Goldys and M. A. Sobhan, *Advanced Functional Materials,* 2012, 22, 1906-1913.

65) V. Amendola, *Phys. Chem. Chem. Phys.,* 2016, 18, 2230-2241.

66) V. Amendola, G. A. Rizzi, S. Polizzi and M. Meneghetti, *J Phys. Chem. B,* 2005, 109, 23125-23128.

67) B. Persson, *Surf. Sci.,* 1993, 281, 153-162.

68) A. Kawabata and R. Kubo, *Journal of the physical society of Japan,* 1966, 21, 1765-1772.

69) C. F. Negre and C. G. Sánchez, *Chemical Physics Letters,* 2010, 494, 255-259.

70) P. Zijlstra, P. M. Paulo, K. Yu, Q. Xu and M. Orrit, *Angewandte Chemie International Edition,* 2012, 51, 8352-8355.

71) M. A. Garcia, J. de la Venta, P. Crespo, J. LLopis, S. Penadés, A. Fernández and A. Hernando, *Phys. Rev. B,* 2005, 72, 241403.

72) M. A. García, *J. Phys. D*, 2011, 44, 283001.

73) S. Malola, L. Lehtovaara, J. Enkovaara and H. Häkkinen, *ACS nano,* 2013, 7, 10263-10270.

74) O. Yeshchenko, I. Bondarchuk, V. Gurin, I. Dmitruk and A. Kotko, *Surf. Sci.,* 2013, 608, 275-281.

75) P. Zolotavin, A. Alabastri, P. Nordlander and D. Natelson, *ACS nano,* 2016, 10, 6972-6979.

76) J. G. Bouillard, W. Dickson, D. P. O'Connor, G. A. Wurtz and A. V. Zayats, *Nano letters,* 2012, 12, 1561-1565.

77) T. R. Jensen, M. L. Duval, K. L. Kelly, A. A. Lazarides, G. C. Schatz and R. P. Van Duyne, *The Journal of Physical Chemistry B,* 1999, 103, 9846-9853.

78) Y. Bao, B. Zhao, D. Hou, J. Liu, F. Wang, X. Wang and T. Cui, *J. Appl. Phys.,* 2014, 115, 223503.

79) Y. Bao, B. Zhao, X. Tang, D. Hou, J. Cai, S. Tang, J. Liu, F. Wang and T. Cui, *Appl. Phys. Lett.,* 2015, 107, 201909.

80) P. K. Jain, K. S. Lee, I. H. El-Sayed and M. A. El-Sayed, *J. Phys. Chem. B,* 2006, 110, 7238-7248.

81) A. Poletti, G. Fracasso, G. Conti, R. Pilot and V. Amendola, *Nanoscale,* 2015, 7, 13702-13714.

82) A. O. Govorov and H. H. Richardson, *Nano Today,* 2007, 2, 30-38.

83) A. O. Govorov, W. Zhang, T. Skeini, H. Richardson, J. Lee and N. A. Kotov, *Nanosc. Res. Lett.,* 2006, 1, 84-90.

84) F. Borghese, P. Denti, R. Saija, G. Toscano and O. I. Sindoni, *Aer. Sci. Technol.,* 1984, 3, 227-235.

85) E. A. Coronado and G. C. Schatz, *J. Chem. Phys.*, 2003, 119, 3926-3934.

86) F. Bonaccorso, M. Zerbetto, A. C. Ferrari and V. Amendola, *J. Phys. Chem. C,* 2013, 117, 13217-13229.

87) V. Amendola, O. M. Bakr and F. Stellacci, *Plasmonics,* 2010, 5, 85-97.

88) A. L. Gonzalez, C. Noguez, G. P. Ortiz and G. Rodriguez-Gattorno, *J. Phys. Chem. B,* 2005, 109, 17512-17517.

89) S. Berciaud, L. Cognet, P. Tamarat and B. Lounis, *Nano Lett.*, 2005, 5, 515-518.

90) H. Häkkinen, *Chem. Soc. Rev.,* 2008, 37, 1847-1859.

91) L. Sementa, A. Marini, G. Barcaro, F. R. Negreiros and A. Fortunelli, *ACS Photonics*, 2014, 1, 315-322.

92) M. Stener, A. Nardelli, R. De Francesco and G. Fronzoni, *The Journal of Physical Chemistry C,* 2007, 111, 11862-11871.

93) N. Durante, A. Fortunelli, M. Broyer and M. Stener, *The Journal of Physical Chemistry C,* 2011, 115, 6277-6282.

94) G. Piccini, R. W. Havenith, R. Broer and M. Stener, *The Journal of Physical Chemistry C,* 2013, 117, 17196-17204.

95) L. Bursi, A. Calzolari, S. Corni and E. Molinari, *ACS Photonics,* 2016, 3, 520-525.

96) R. L. Gieseking, M. A. Ratner and G. C. Schatz, *The Journal of Physical Chemistry A,* 2016, .

97) N. Zohar, L. Chuntonov and G. Haran, *Journal of Photochemistry and Photobiology C: Photochemistry Reviews,* 2014, 21, 26-39.

98) S. K. Ghosh and T. Pal, *Chem. Rev.,* 2007, 107, 4797-4862.

99) N. A. Mirin, K. Bao and P. Nordlander, *The Journal of Physical Chemistry A,* 2009, 113, 4028-4034.

100) A. Lovera, B. Gallinet, P. Nordlander and O. J. Martin, *ACS nano,* 2013, 7, 4527-4536.

101) M. Rahmani, B. Lukiyanchuk, B. Ng, A. T. KG, Y. Liew and M. Hong, *Optics express,* 2011, 19, 4949-4956.

102) S. Mukherjee, H. Sobhani, J. B. Lassiter, R. Bardhan, P. Nordlander and N. J. Halas, *Nano letters,* 2010, 10, 2694-2701.

103) P. K. Jain, W. Huang and M. A. El-Sayed, *Nano Letters,* 2007, 7, 2080-2088.

104) T. Atay, J. Song and A. V. Nurmikko, *Nano Letters,* 2004, 4, 1627-1631.

105) P. K. Jain and M. A. El-Sayed, *Nano letters,* 2007, 7, 2854-2858.

106) J. J. Storhoff, A. A. Lazarides, R. C. Mucic, C. A. Mirkin, R. L. Letsinger and G. C. Schatz, *J. Am. Chem. Soc.,* 2000, 122, 4640-4650.

107) E. Messina, E. Cavallaro, A. Cacciola, M. A. Iatì, P. G. Gucciardi, F. Borghese, P. Denti, R. Saija, G. Compagnini, M. Meneghetti, V. Amendola and O. M. Maragò, *ACS Nano,* 2011, 5, 905.

108) R. W. Taylor, R. Esteban, S. Mahajan, R. Coulston, O. A. Scherman, J. Aizpurua and J. J. Baumberg, *The Journal of Physical Chemistry C,* 2012, 116, 25044-25051.

109) M. Hentschel, M. Saliba, R. Vogelgesang, H. Giessen, A. P. Alivisatos and N. Liu, *Nano letters,* 2010, 10, 2721-2726.

110) A. K. Sarychev, G. Shvets and V. M. Shalaev, *Physical Review E,* 2006, 73, 036609.

111) F. Shafiei, F. Monticone, K. Q. Le, X. Liu, T. Hartsfield, A. Alù and X. Li, *Nature nanotechnology,* 2013, 8, 95-99.

112) S. Mühlig, A. Cunningham, S. Scheeler, C. Pacholski, T. Bürgi, C. Rockstuhl and F. Lederer, *ACS nano,* 2011, 5, 6586-6592.

113) S. Campione, C. Guclu, R. Ragan and F. Capolino, *Acs Photonics,* 2014, 1, 254-260.

114) S. N. Sheikholeslami, H. Alaeian, A. L. Koh and J. A. Dionne, *Nano letters,* 2013, 13, 4137-4141.

115) J. Park, H. Kang, Y. H. Kim, S. Lee, T. G. Lee and J. Wi, *Nanoscale*, 2016, 8, 15514-15520.

116) J. Wi, S. Tominaka, K. Uosaki and T. Nagao, *Physical Chemistry Chemical Physics,* 2012, 14, 9131-9136.

117) P. Reichenbach, A. Horneber, D. A. Gollmer, A. Hille, J. Mihaljevic, C. Schäfer, D. P. Kern, A. J. Meixner, D. Zhang and M. Fleischer, *Optics express,* 2014, 22, 15484-15501.

118) S. Barbosa, A. Agrawal, L. Rodríguez-Lorenzo, I. Pastoriza-Santos, R. A. Alvarez-Puebla, A. Kornowski, H. Weller and L. M. Liz-Marzán, *Langmuir,* 2010, 26, 14943-14950.

119) L. Soares, A. Csáki, J. Jatschka, W. Fritzsche, O. Flores, R. Franco and E. Pereira, *Analyst,* 2014, 139, 4964-4973.

120) H. Wu, C. Kuo and M. H. Huang, *Langmuir,* 2010, 26, 12307-12313.

121) J. Luan, K. Liu, S. Tadepalli, Q. Jiang, J. J. Morrissey, E. D. Kharasch and S. Singamaneni, *ACS Applied Materials & Interfaces,* 2016, .

122) N. Harris, M. J. Ford, P. Mulvaney and M. B. Cortie, *Gold Bull.*, 2008, 41, 5-14.

123) S. W. Prescott and P. Mulvaney, *J. Appl. Phys.*, 2006, 99, 123504.

124) P. K. Jain, I. H. El-Sayed and M. A. El-Sayed, *Nano Today,* 2007, 2, 18-29.

125) S. Link and M. A. El-Sayed, *The Journal of Physical Chemistry B,* 1999, 103, 8410-8426.

126) A. Teulle, M. Bosman, C. Girard, K. L. Gurunatha, M. Li, S. Mann and E. Dujardin, *Nat. Mater.,* 2014, .

127) L. O. Herrmann, V. K. Valev, C. Tserkezis, J. S. Barnard, S. Kasera, O. A. Scherman, J. Aizpurua and J. J. Baumberg, *Nat. Commun.,* 2014, 5.

128) V. Amendola, S. Scaramuzza, S. Agnoli, S. Polizzi and M. Meneghetti, *Nanoscale,* 2014, 6, 1423-1433.

129) M. B. Cortie and A. M. McDonagh, *Chem. Rev.*, 2011, 111, 3713-3735.

130) V. Amendola, M. Meneghetti, O. M. Bakr, P. Riello, S. Polizzi, S. Fiameni, H. Dalaver, P. Arosio, T. Orlando, C. de Julian Fernandez, F. Pineider, C. Sangregorio and A. Lascialfari, *Nanoscale*, 2013, 5, 5611-5619.

131) V. Amendola, S. Scaramuzza, S. Agnoli, G. Granozzi, M. Meneghetti, G. Campo, V. Bonanni, F. Pineider, C. Sangregorio, P. Ghigna, S. Fiameni and L. Nodari, *Nano Res.*, 2015, 8, 4007-4023.

132) V. Amendola, S. Scaramuzza, L. Litti, M. Meneghetti, G. Zuccolotto, A. Rosato, E. Nicolato, P. Marzola, G. Fracasso, C. Anselmi, M. Pinto and M. Colombatti, *Small,* 2014, 10, 2476-2486.

133) D. Rioux and M. Meunier, *The Journal of Physical Chemistry C,* 2015, 119, 13160-13168.

134) S. W. Verbruggen, M. Keulemans, J. A. Martens and S. Lenaerts, *The Journal of Physical Chemistry C,* 2013, 117, 19142-19145.

135) S. Link, Z. L. Wang and M. El-Sayed, *J. Phys. Chem. B*, 1999, 103, 3529-3533.

136) S. Sarina, H. Zhu, E. Jaatinen, Q. Xiao, H. Liu, J. Jia, C. Chen and J. Zhao, *J. Am. Chem. Soc.*, 2013, 135, 5793-5801.

137) J. Suntivich, Z. Xu, C. E. Carlton, J. Kim, B. Han, S. W. Lee, N. Bonnet, N. Marzari, L. F. Allard, H. A. Gasteiger, K. Hamad-Schifferli and Y. Shao-Horn, *J. Am. Chem. Soc.*, 2013, 135, 7985-7991.

138) F. Wang, C. Li, H. Chen, R. Jiang, L. Sun, Q. Li, J. Wang, J. C. Yu and C. Yan, *J. Am. Chem. Soc.*, 2013, 135, 5588-5601.

139) R. E. Cable and R. E. Schaak, *Chem. Mater.*, 2007, 19, 4098-4104.

140) V. Keast, J. Wallace, C. Wrightson, M. Tai, A. Gentle, M. Arnold and M. Cortie, *Journal of Physics: Condensed Matter,* 2015, 27, 505501.

141) P. K. Jain, X. Huang, I. H. El-Sayed and M. A. El-Sayed, *Acc. Chem. Res.*, 2008, 41, 1578-1586.

142) Y. Lee, Y. Kudryavtsev, V. Nemoshkalenko, R. Gontarz and J. Rhee, *Phys. Rev. B*, 2003, 67, 104424.

143) G. Baffou, R. Quidant and García de Abajo, F Javier, *ACS nano*, 2010, 4, 709-716.

144) S. Bruzzone and M. Malvaldi, *J. Phys. Chem. C*, 2009, 113, 15805-15810.

145) L. Le Thi Ngoc, T. Yuan, N. Oonishi, J. W. van Nieuwkasteele, A. van den Berg, H. P. Permentier, R. Bischoff and E. T. Carlen, *J. Phys. Chem. C,* 2016, 120, 18756-18762.

146) M. A. Iatì, E. Lidorikis and R. Saija, in *in Handbook of enhanced spectroscopies,* ed. nonymous Pan Stanford Publishing, 2016,.

147) M. I. Mishchenko, L. D. Travis and A. A. Lacis, *Scattering, absorption, and emission of light by small particles,* Cambridge university press, 2002.

148) J. Zhao, A. O. Pinchuk, J. M. McMahon, S. Li, L. K. Ausman, A. L. Atkinson and G. C. Schatz, *Acc. Chem. Res.*, 2008, 41, 1710-1720.

149) P. B. Johnson and R. W. Christy, *Phys. Rev. B,* 1972, 6, 4370-4379.

150) E. D. Palik, *Handbook of Optical Constants of Solids*, Academic Press, 1985.

151) R. L. Olmon, B. Slovick, T. W. Johnson, D. Shelton, S. Oh, G. D. Boreman and M. B. Raschke, *Physical Review B,* 2012, 86, 235147.

152) J. Trollmann and A. Pucci, *The Journal of Physical Chemistry C,* 2014, 118, 15011-15018.

153) V. Myroshnychenko, J. Rodríguez-Fernández, I. Pastoriza-Santos, A. M. Funston, C. Novo, P. Mulvaney, L. M. Liz-Marzán and de Abajo, F Javier Garcia, *Chem. Soc. Rev.*, 2008, 37, 1792-1805.

154) N. A. Mortensen, S. Raza, M. Wubs, T. Søndergaard and S. I. Bozhevolnyi, *Nature communications*, 2014, 5.

155) K. J. Savage, M. M. Hawkeye, R. Esteban, A. G. Borisov, J. Aizpurua and J. J. Baumberg, *Nature,* 2012, 491, 574-577.

156) W. Zhu, R. Esteban, A. G. Borisov, J. J. Baumberg, P. Nordlander, H. J. Lezec, J. Aizpurua and K. B. Crozier, *Nature communications*, 2016, 7.

157) J. Zuloaga, E. Prodan and P. Nordlander, *Nano letters,* 2009, 9, 887-891.

158) R. Esteban, A. G. Borisov, P. Nordlander and J. Aizpurua, *Nature Communications*, 2012, 3, 825.

159) C. Ciraci, R. T. Hill, J. J. Mock, Y. Urzhumov, A. I. Fernandez-Dominguez, S. A. Maier, J. B. Pendry, A. Chilkoti and D. R. Smith, *Science*, 2012, 337, 1072-1074.

160) A. D. Boardman, *Electromagnetic surface modes*, John Wiley & Sons, 1982.

161) A. L. Fetter, *Annals of Physics*, 1973, 81, 367-393.

162) M. Quinten, *Optical properties of nanoparticle systems: Mie and beyond*, John Wiley & Sons, 2010.

163) P. Alonso-González, P. Albella, M. Schnell, J. Chen, F. Huth, A. García-Etxarri, F. Casanova, F. Golmar, L. Arzubiaga and L. Hueso, *Nature communications*, 2012, 3, 684.

164) A. L. Aden and M. Kerker, *J. Appl. Phys.*, 1951, 22, 1242-1246.

165) P. J. Wyatt, *Physical Review*, 1962, 127, 1837.

166) P. Jones, O. Maragó and G. Volpe, *Optical tweezers: Principles and applications*, Cambridge University Press, 2015.

167) T. Wriedt, *Journal of Quantitative Spectroscopy and Radiative Transfer*, 2009, 110, 833-843.

168) E. M. Purcell and C. R. Pennypacker, *Astrophys. J.*, 1973, 186, 705-714.

169) B. T. Draine, *Astrophys. J.*, 1988, 333, 848-872.

170) J. Goodman, B. T. Draine and P. J. Flatau, *Opt. Lett.*, 1991, 16, 1198-1200.

171) B. T. Draine and P. J. Flatau, *arXiv,* 2013, , 1305.6497.

172) M. A. Yurkin and A. G. Hoekstra, *Journal of Quantitative Spectroscopy and Radiative Transfer,* 2007, 106, 558-589.

173) C. Girard, *Reports on progress in physics,* 2005, 68, 1883.

174) B. T. Draine and P. J. Flatau, *arXiv,* 2010, , 1002.1505.

175) F. L. Teixeira, *Journal of Microwaves, Optoelectronics and Electromagnetic Applications (JMOe),* 2007, 6, 83-95.

176) K. S. Yee, *IEEE Trans.Antennas Propag,* 1966, 14, 302-307.

177) F. Hao, C. L. Nehl, J. H. Hafner and P. Nordlander, *Nano letters*, 2007, 7, 729-732.

178) A. Taflove and S. C. Hagness, *Norwood, 2nd Edition, MA: Artech House, l995,* 1995, .

179) J. D. Jackson, *Classical electrodynamics*, Wiley, 1999.

180) F. G. de Abajo and A. Howie, *Phys. Rev. Lett.,* 1998, 80, 5180.

181) D. M. Solis, J. M. Taboada, F. Obelleiro, L. M. Liz-Marzan and García de Abajo, F Javier, *ACS nano,* 2014, 8, 7559-7570.

182) F. Borghese, P. Denti and R. Saija, *Scattering from model nonspherical particles: theory and applications to environmental physics*, Springer, 2007.

183) P. C. Waterman, *Physical review D,* 1971, 3, 825.

184) R. Saija, M. A. Iatì, F. Borghese, P. Denti, S. Aiello and C. Cecchi-Pestellini, *Astrophys. J.,* 2001, 559, 993.

185) M. Iatì, C. Cecchi-Pestellini, D. Williams, F. Borghese, P. Denti, R. Saija and S. Aiello, *Monthly Notices of the Royal Astronomical Society*, 2001, 322, 749-756.

186) F. Borghese, P. Denti, R. Saija, G. Toscano and O. Sindoni, *Il Nuovo Cimento B (1971-1996),* 1984, 81, 29-50.

187) F. Borghese, P. Denti, R. Saija, M. Iatı and O. Sindoni, *Journal of Quantitative Spectroscopy and Radiative Transfer,* 2001, 70, 237-251.

188) E. Fucile, F. Borghese, P. Denti and R. Saija, *JOSA A,* 1993, 10, 2611-2617.

189) Y. Okada, in *in Light Scattering Reviews 5,* ed. nonymous Springer, 2010, pp.3-35.

190) P. Nordlander, C. Oubre, E. Prodan, K. Li and M. Stockman, *Nano Letters,* 2004, 4, 899-903.

191) H. Wang, D. W. Brandl, P. Nordlander and N. J. Halas, *Acc. Chem. Res.,* 2007, 40, 53-62.

192) P. Chýlek, G. Videen, D. Geldart, J. S. Dobbie and H. Tso, *Light scattering by nonspherical particles: theory, measurements, and applications*, 2000, 1, 274.

193) D. Stroud, *Physical Review B*, 1975, 12, 3368.

194) P. D. Howes, R. Chandrawati and M. M. Stevens, *Science*, 2014, 346, 1247390.

195) O. Tokel, F. Inci and U. Demirci, *Chem. Rev.*, 2014, 114, 5728-5752.

196) W. Zhou, X. Gao, D. Liu and X. Chen, *Chem. Rev.*, 2015, 115, 10575-10636.

197) K. S. Lee and M. A. El-Sayed, *J Phys Chem B*, 2006, 110, 19220-19225.

198) G. Y. Tonga, K. Saha and V. M. Rotello, *Adv Mater*, 2014, 26, 359-370.

199) L. Guo, J. A. Jackman, H. Yang, P. Chen, N. Cho and D. Kim, *Nano Today*, 2015, 10, 213-239.

200) Z. Yuan, C. Hu, H. Chang and C. Lu, *Analyst*, 2016, 141, 1611-1626.

201) W. Zheng, H. Li, W. Chen, J. Ji and X. Jiang, *Anal. Chem.*, 2016, 88, 4140-4146.

202) L. Chen, J. Li and L. Chen, *ACS applied materials & interfaces*, 2014, 6, 15897-15904.

203) H. Niu, S. Wang, Z. Zhou, Y. Ma, X. Ma and Y. Cai, *Anal. Chem.*, 2014, 86, 4170-4177.

204) Y. Jiang, H. Zhao, N. Zhu, Y. Lin, P. Yu and L. Mao, *Angewandte Chemie*, 2008, 120, 8729-8732.

205) C. Guarise, L. Pasquato, V. De Filippis and P. Scrimin, *Proc. Natl. Acad. Sci. U. S. A.*, 2006, 103, 3978-3982.

206) A. Laromaine, L. Koh, M. Murugesan, R. V. Ulijn and M. M. Stevens, *J. Am. Chem. Soc.*, 2007, 129, 4156-4157.

207) T. Lin, W. Chen, Y. Shiang, C. Huang and H. Chang, *Biosensors and Bioelectronics*, 2011, 29, 204-209.

208) C. A. Mirkin, R. L. Letsinger, R. C. Mucic and J. J. Storhoff, *Nature*, 1996, 382, 607-609.

209) C. M. Niemeyer, *Angew.Chem.Int.Ed.*, 2001, 40, 4128-4158.

210) H. Li and L. Rothberg, *Proc. Natl. Acad. Sci. U. S. A.*, 2004, 101, 14036-14039.

211) L. Guo, Y. Xu, A. R. Ferhan, G. Chen and D. Kim, *J. Am. Chem. Soc.*, 2013, 135, 12338-12345.

212) C. D. Medley, J. E. Smith, Z. Tang, Y. Wu, S. Bamrungsap and W. Tan, *Anal. Chem.*, 2008, 80, 1067-1072.

213) P. Cairns, *Nature Reviews Cancer*, 2007, 7, 531-543.

214) W. Zhao, M. A. Brook and Y. Li, *ChemBioChem*, 2008, 9, 2363-2371.

215) T. M. Lee, *Sensors*, 2008, 8, 5535-5559.

216) B. M. Reinhard, M. Siu, H. Agarwal, A. P. Alivisatos and J. Liphardt, *Nano letters*, 2005, 5, 2246-2252.

217) J. Becker, A. Trügler, A. Jakab, U. Hohenester and C. Sönnichsen, *Plasmonics*, 2010, 5, 161-167.

218) J. Yamamichi, T. Ojima, M. Iida, K. Yurugi, T. Imamura, E. Ashihara, S. Kimura and T. Maekawa, *Analytical and bioanalytical chemistry*, 2014, 406, 4527-4533.

219) A. Horrer, K. Krieg, K. Freudenberger, S. Rau, L. Leidner, G. Gauglitz, D. P. Kern and M. Fleischer, *Analytical and bioanalytical chemistry*, 2015, 407, 8225-8231.

220) J. Yuan, R. Oliver, J. Li, J. Lee, M. Aguilar and Y. Wu, *Biosensors and Bioelectronics*, 2007, 23, 144-148.

221) M. Frasconi, C. Tortolini, F. Botre and F. Mazzei, *Anal. Chem.*, 2010, 82, 7335-7342.

222) M. Frasconi, F. Mazzei and T. Ferri, *Analytical and bioanalytical chemistry*, 2010, 398, 1545-1564.

223) O. V. Gnedenko, Y. V. Mezentsev, A. A. Molnar, A. V. Lisitsa, A. S. Ivanov and A. I. Archakov, *Anal. Chim. Acta*, 2013, 759, 105-109.

224) F. Mastrotto, P. Caliceti, V. Amendola, S. Bersani, J. P. Magnusson, M. Meneghetti, G. Mantovani, C. Alexander and S. Salmaso, *Chem.Commun.*, 2011, 47, 9846-9848.

225) X. Huang, I. H. El Sayed, W. Qian and M. A. El Sayed, *J. Am. Chem. Soc.*, 2006, 128, 2115-2120.

226) V. Amendola and M. Meneghetti, *J. Mater. Chem.*, 2007, 17, 4705-4710.

227) J. C. Love, L. A. Estroff, J. K. Kriebel, R. G. Nuzzo and G. M. Whitesides, *Chem. Rev.*, 2005, 105, 1103-1170.

228) A. Verma and F. Stellacci, *Small*, 2010, 6, 12-21.

229) P. del Pino, F. Yang, B. Pelaz, Q. Zhang, K. Kantner, R. Hartmann, N. Martinez de Baroja, M. Gallego, M. Möller and B. B. Manshian, *Angewandte Chemie International Edition*, 2016, 55, 5483-5487.

230) J. H. Johnston and K. A. Lucas, *Gold Bulletin*, 2011, 44, 85-89.

231) G. Wang, X. Chen, S. Liu, C. Wong and S. Chu, *ACS nano*, 2016, 10, 1788-1794.

232) P. Zijlstra, J. W. Chon and M. Gu, *Nature*, 2009, 459, 410-413.

233) P. K. Kundu, D. Samanta, R. Leizrowice, B. Margulis, H. Zhao, M. Börner, T. Udayabhaskararao, D. Manna and R. Klajn, *Nature chemistry,* 2015, 7, 646-652.

234) M. Hu, J. Chen, Z. Y. Li, L. Au, G. V. Hartland, X. Li, M. Marquez and Y. Xia, *Chem. Soc. Rev.,* 2006, 35, 1084-1094.

235) X. Huang, P. K. Jain, I. H. El-Sayed and M. A. El-Sayed, *Las.Med.Sci.,* 2008, 23, 217-228.

236) R. Weissleder, *Nat. Biotechnol.,* 2001, 19, 316-316.

237) P. Vijayaraghavan, C. Liu, R. Vankayala, C. Chiang and K. C. Hwang, *Adv Mater,* 2014, 26, 6689-6695.

238) S. Hashimoto, D. Werner and T. Uwada, *J. Photochem. Photobiol. C,* 2012, 13, 28-54.

239) K. Jiang, D. A. Smith and A. O. Pinchuk, *J. Phys. Chem. C,* 2013, 117, 27073-27080.

240) G. Baffou, R. Quidant and C. Girard, *Appl. Phys. Lett.,* 2009, 94, 153109.

241) S. Freddi, L. Sironi, R. D'Antuono, D. Morone, A. Donà, E. Cabrini, L. D'Alfonso, M. Collini, P. Pallavicini and G. Baldi, *Nano letters,* 2013, 13, 2004-2010.

242) S. S. Agasti, A. Chompoosor, C. You, P. Ghosh, C. K. Kim and V. M. Rotello, *J. Am. Chem. Soc.,* 2009, 131, 5728-5729.

243) D. Pissuwan, T. Niidome and M. B. Cortie, *J. Controlled Release,* 2011, 149, 65-71.

244) C. Hsiao, H. Chen, Z. Liao, R. Sureshbabu, H. Hsiao, S. Lin, Y. Chang and H. Sung, *Adv. Funct. Mater.,* 2014, 25, 721.

245) K. Turcheniuk, C. Hage, J. Spadavecchia, A. Y. Serrano, I. Larroulet, A. Pesquera, A. Zurutuza, M. G. Pisfil, L. Héliot and J. Boukaert, *J. Mater. Chem. B,* 2015, 3, 375-386.

246) W. Li and X. Chen, *Nanomedicine,* 2015, 10, 299-320.

247) D. Boyer, P. Tamarat, A. Maali, B. Lounis and M. Orrit, *Science,* 2002, 297, 1160-1163.

248) G. Baffou, J. Polleux, H. Rigneault and S. Monneret, *The Journal of Physical Chemistry C,* 2014, 118, 4890-4898.

249) Z. Fang, Y. Zhen, O. Neumann, A. Polman, García de Abajo, F Javier, P. Nordlander and N. J. Halas, *Nano Lett.,* 2013, 13, 1736-1742.

250) L. Tong, Y. Zhao, T. B. Huff, M. N. Hansen, A. Wei and J. Cheng, *Adv Mater,* 2007, 19, 3136-3141.

251) E. S. Day, J. G. Morton and J. L. West, *J. Biomech. Eng.,* 2009, 131, 074001.

252) P. Atkins and J. De Paula, *New York,* 2006, , 776-780.

253) M. Borzenkov, A. Määttänen, P. Ihalainen, M. Collini, E. Cabrini, G. Dacarro, P. Pallavicini and G. Chirico, *ACS applied materials & interfaces,* 2016, 8, 9909-9916.

254) M. S. Yavuz, Y. Cheng, J. Chen, C. M. Cobley, Q. Zhang, M. Rycenga, J. Xie, C. Kim, K. H. Song and A. G. Schwartz, *Nature materials*, 2009, 8, 935-939.

255) J. Conde, N. Oliva, Y. Zhang and N. Artzi, *Nat. Mater.*, 2016, 15, 1128-1138.

256) C. Leduc, J. Jung, R. R. Carney, F. Stellacci and B. Lounis, *ACS nano,* 2011, 5, 2587-2592.

257) E. Y. Lukianova-Hleb, Y. Kim, I. Belatsarkouski, A. M. Gillenwater, B. E. O'Neill and D. O. Lapotko, *Nature nanotechnology,* 2016, 11, 525-532.

258) R. Lachaine, C. Boutopoulos, P. Lajoie, É. Boulais and M. Meunier, *Nano letters,* 2016, 16, 3187-3194.

259) J. Shao, M. Xuan, L. Dai, T. Si, J. Li and Q. He, *Angewandte Chemie,* 2015, 127, 12973-12978.

260) E. Y. Lukianova-Hleb, A. N. Volkov and D. O. Lapotko, *Langmuir,* 2014, 30, 7425-7434.

261) H. M. Robert, F. Kundrat, E. Bermúdez-Ureña, H. Rigneault, S. Monneret, R. Quidant, J. Polleux and G. Baffou, *ACS Omega,* 2016, 1, 2-8.

262) S. Y. Nam, L. M. Ricles, L. J. Suggs and S. Y. Emelianov, *PLoS One*, 2012, 7, e37267.

263) C. Bao, N. Beziere, P. del Pino, B. Pelaz, G. Estrada, F. Tian, V. Ntziachristos, de la Fuente, Jesus M and D. Cui, *Small,* 2013, 9, 68-74.

264) F. Ratto, S. Centi, C. Avigo, C. Borri, F. Tatini, L. Cavigli, C. Kusmic, B. Lelli, S. Lai and S. Colagrande, *Advanced Functional Materials,* 2016, .

265) A. Taruttis and V. Ntziachristos, *Nat. Photon.*, 2015, 9, 219-227.

266) I. Aibara, S. Mukai and S. Hashimoto, *The Journal of Physical Chemistry C,* 2016, 120, 17745-17752.

267) A. Urban, M. Fedoruk, M. Horton, J. Radler, F. Stefani and J. Feldmann, *Nano letters,* 2009, 9, 2903-2908.

268) L. Cao, D. N. Barsic, A. R. Guichard and M. L. Brongersma, *Nano letters,* 2007, 7, 3523-3527.

269) S. Hashimoto, T. Uwada, M. Hagiri, H. Takai and T. Ueki, *The Journal of Physical Chemistry C,* 2009, 113, 20640-20647.

270) O. Neumann, C. Feronti, A. D. Neumann, A. Dong, K. Schell, B. Lu, E. Kim, M. Quinn, S. Thompson, N. Grady, P. Nordlander, M. Oden and N. J. Halas, *Proc. Natl. Acad. Sci. U. S. A.,* 2013, 110, 11677-11681.

271) O. Neumann, A. S. Urban, J. Day, S. Lal, P. Nordlander and N. J. Halas, *ACS nano,* 2012, 7, 42-49.

272) G. González-Rubio, A. Guerrero-Martínez and L. M. Liz-Marzán, *Acc. Chem. Res.*, 2016, 49, 678-686.

273) P. Boyer and M. Meunier, *J. Phys. Chem. C,* 2012, 116, 8014-8019.

274) J. Qiu and W. D. Wei, *The Journal of Physical Chemistry C,* 2014, 118, 20735-20749.

275) C. Vázquez-Vázquez, B. Vaz, V. Giannini, M. Pérez-Lorenzo, R. A. Alvarez-Puebla and M. A. Correa-Duarte, *J. Am. Chem. Soc.*, 2013, 135, 13616-13619.

276) Y. Ben-Shahar, F. Scotognella, I. Kriegel, L. Moretti, G. Cerullo, E. Rabani and U. Banin, *Nature communications,* 2016, 7.

277) Y. Ben-Shahar, F. Scotognella, N. Waiskopf, I. Kriegel, S. Dal Conte, G. Cerullo and U. Banin, *Small,* 2015, 11, 462-471.

278) Y. Kim, D. Dumett Torres and P. K. Jain, *Nano letters,* 2016, 16, 3399-3407.

279) A. Sousa-Castillo, M. Comesaña-Hermo, B. Rodríguez-González, M. Pérez-Lorenzo, Z. Wang, X. Kong, A. O. Govorov and M. A. Correa-Duarte, *The Journal of Physical Chemistry C,* 2016, 120, 11690-11699.

280) Y. Zhang, C. Yam and G. C. Schatz, *The journal of physical chemistry letters,* 2016, .

281) P. Dombi, A. Hörl, P. Rácz, I. Márton, A. Trügler, J. R. Krenn and U. Hohenester, *Nano letters,* 2013, 13, 674-678.

282) S. Mukherjee, L. Zhou, A. M. Goodman, N. Large, C. Ayala-Orozco, Y. Zhang, P. Nordlander and N. J. Halas, *J. Am. Chem. Soc.*, 2013, 136, 64-67.

283) L. Ma, K. Chen, F. Nan, J. Wang, D. Yang, L. Zhou and Q. Wang, *Advanced Functional Materials,* 2016, 26, 6076-6083.

284) K. Ueno, T. Oshikiri and H. Misawa, *ChemPhysChem,* 2016, 17, 199-215.

285) Z. Xu, M. Quintanilla, F. Vetrone, A. O. Govorov, M. Chaker and D. Ma, *Advanced Functional Materials,* 2015, 25, 2950-2960.

286) Y. Yu, Z. Ji, S. Zu, B. Du, Y. Kang, Z. Li, Z. Zhou, K. Shi and Z. Fang, *Adv. Funct. Mater.*, 2016, 26, 6394-6401.

287) S. Mubeen, J. Lee, N. Singh, S. Krämer, G. D. Stucky and M. Moskovits, *Nature nanotechnology,* 2013, 8, 247-251.

288) T. Oshikiri, K. Ueno and H. Misawa, *Angewandte Chemie,* 2016, .

289) M. Moskovits, *J. Raman Spectrosc.*, 2005, 36, 485-496.

290) J. R. Lakowicz, *Anal. Biochem.*, 2001, 298, 1-24.

291) B. L. Darby, B. Auguié, M. Meyer, A. E. Pantoja and E. C. Le Ru, *Nature Photonics*, 2016, 10, 40-45.

292) T. Jensen, R. V. Duyne, S. Johnson and V. Maroni, *Appl. Spectrosc.*, 2000, 54, 371-377.

293) T. Ichimura, N. Hayazawa, M. Hashimoto, Y. Inouye and S. Kawata, *J. Raman Spectrosc.*, 2003, 34, 651-654.

294) Y. Zhang, Y. Zhen, O. Neumann, J. K. Day, P. Nordlander and N. J. Halas, *Nature communications*, 2014, 5.

295) J. Butet and O. J. Martin, *The Journal of Physical Chemistry C*, 2015, 119, 15547-15556.

296) H. K. Turley, Z. Hu, D. W. Silverstein, D. A. Cooper, L. Jensen and J. P. Camden, *J. Phys. Chem. C*, 2016, 120, 20936-20942.

297) R. Dynich and A. Ponyavina, *Journal of Applied Spectroscopy*, 2008, 75, 832-838.

298) E. Le Ru and P. Etchegoin, *Principles of Surface-Enhanced Raman Spectroscopy: and related plasmonic effects*, Elsevier, 2008.

299) G. Toscano, S. Raza, S. Xiao, M. Wubs, A. Jauho, S. I. Bozhevolnyi and N. A. Mortensen, *Opt. Lett.*, 2012, 37, 2538-2540.

300) K. Imura, H. Okamoto, M. K. Hossain and M. Kitajima, *Nano letters*, 2006, 6, 2173-2176.

301) V. Amendola and M. Meneghetti, *Adv. Funct. Mater.*, 2012, 22, 353-360.

302) E. C. Le Ru and P. G. Etchegoin, *Chem. Phys. Lett.*, 2006, 423, 63-66.

303) S. L. Kleinman, B. Sharma, M. G. Blaber, A. Henry, N. Valley, R. G. Freeman, M. J. Natan, G. C. Schatz and R. P. Van Duyne, *J. Am. Chem. Soc.*, 2012, 135, 301-308.

304) C. D'Andrea, A. Irrera, B. Fazio, A. Foti, E. Messina, O. Maragò, S. Kessentini, P. Artoni, C. David and P. Gucciardi, *Journal of Optics*, 2015, 17, 114016.

305) P. Alonso-González, P. Albella, F. Neubrech, C. Huck, J. Chen, F. Golmar, F. Casanova, L. E. Hueso, A. Pucci and J. Aizpurua, *Phys. Rev. Lett.*, 2013, 110, 203902.

306) R. Aroca, *Surface-enhanced vibrational spectroscopy*, John Wiley & Sons, 2006.

307) K. C. Bantz, A. F. Meyer, N. J. Wittenberg, H. Im, Ö. Kurtuluş, S. H. Lee, N. C. Lindquist, S. Oh and C. L. Haynes, *Physical Chemistry Chemical Physics*, 2011, 13, 11551-11567.

308) J. R. Lombardi and R. L. Birke, *J. Phys. Chem. C*, 2008, 112, 5605-5617.

309) J. R. Lombardi and R. L. Birke, *Acc. Chem. Res.*, 2009, 42, 734-742.

310) E. C. Le Ru, P. G. Etchegoin and M. Meyer, *J. Chem. Phys.*, 2006, 125, 204701.

311) M. Moskovits, *Phys. Chem. Chem. Phys.*, 2013, 15, 5301-5311.

312) A. Wokaun, *Solid state physics*, 1984, 38, 223-294.

313) E. Le Ru, M. Meyer, E. Blackie and P. Etchegoin, *J. Raman Spectrosc.*, 2008, 39, 1127-1134.

314) G. Kovacs, R. Loutfy, P. Vincett, C. Jennings and R. Aroca, *Langmuir*, 1986, 2, 689-694.

315) C. Murray and D. Allara, *J. Chem. Phys.*, 1982, 76, 1290-1303.

316) G. Compagnini, C. Galati and S. Pignataro, *Physical Chemistry Chemical Physics*, 1999, 1, 2351-2353.

317) C. M. Aikens and G. C. Schatz, *J Phys. Chem. A*, 2006, 110, 13317-13324.

318) I. Ros, T. Placido, V. Amendola, C. Marinzi, N. Manfredi, R. Comparelli, M. Striccoli, A. Agostiano, A. Abbotto, D. Pedron, R. Pilot and R. Bozio, *Plasmonics*, 2014, 9, 581-593.

319) L. Litti, V. Amendola, G. Toffoli and M. Meneghetti, *Anal. Bioanal. Chem.*, 2016, in press.

320) X. M. Qian and S. M. Nie, *Chem. Soc. Rev.*, 2008, 37, 912-920.

321) P. G. Etchegoin and E. C. L. Ru, *Phys. Chem. Chem. Phys.*, 2008, 10, 6079-6089.

322) B. Sharma, R. R. Frontiera, A. Henry, E. Ringe and R. P. Van Duyne, *Materials today*, 2012, 15, 16-25.

323) L. Polavarapu and L. M. Liz-Marzán, *Physical Chemistry Chemical Physics*, 2013, 15, 5288-5300.

324) M. Fan, G. F. Andrade and A. G. Brolo, *Anal. Chim. Acta*, 2011, 693, 7-25.

325) F. Romanato, R. Pilot, M. Massari, T. Ongarello, G. Pirruccio, P. Zilio, G. Ruffato, M. Carli, D. Sammito and V. Giorgis, *Microelectronic Engineering*, 2011, 88, 2717-2720.

326) J. G. Son, S. W. Han, J. Wi and T. G. Lee, *Nanoscale*, 2015, 7, 8338-8342.

327) N. Felidj, J. Aubard, G. Levi, J. Krenn, A. Hohenau, G. Schider, A. Leitner and F. Aussenegg, *Appl. Phys. Lett.*, 2003, 82, 3095-3097.

328) R. Pilot, A. Zoppi, S. Trigari, F. Deepak, E. Giorgetti and R. Bozio, *Physical Chemistry Chemical Physics*, 2015, 17, 7355-7365.

329) V. Weber, A. Feis, C. Gellini, R. Pilot, P. Salvi and R. Signorini, *Physical Chemistry Chemical Physics*, 2015, 17, 21190-21197.

330) A. D. McFarland, M. A. Young, J. A. Dieringer and R. P. Van Duyne, *The Journal of Physical Chemistry B*, 2005, 109, 11279-11285.

331) W. Xie and S. Schlücker, *Physical Chemistry Chemical Physics*, 2013, 15, 5329-5344.

332) R. A. Tripp, R. A. Dluhy and Y. Zhao, *Nano Today,* 2008, 3, 31-37.

333) S. D. Hudson and G. Chumanov, *Anal. Bioanal. Chem.,* 2009, 394, 679-686.

334) S. Zeng, K. Yong, I. Roy, X. Dinh, X. Yu and F. Luan, *Plasmonics,* 2011, 6, 491-506.

335) J. Zheng and L. He, *Comprehensive reviews in food science and food safety,* 2014, 13, 317-328.

336) V. Amendola, M. Meneghetti, S. Fiameni, S. Polizzi, G. Fracasso, A. Boscaini and M. Colombatti, *Anal. Meth.,* 2011, 3, 849-856.

337) Y. Wang, B. Yan and L. Chen, *Chem. Rev.,* 2012, 113, 1391-1428.

338) L. A. Lane, X. Qian and S. Nie, *Chem. Rev.,* 2015, 115, 10489-10529.

339) S. Harmsen, R. Huang, M. A. Wall, H. Karabeber, J. M. Samii, M. Spaliviero, J. R. White, S. Monette, R. O'Connor, K. L. Pitter, S. A. Sastra, M. Saborowski, E. C. Holland, S. Singer, K. P. Olive, S. W. Lowe, R. G. Blasberg and M. F. Kircher, *Sci. Transl. Med.,* 2015, 7, 271ra7.

340) R. Toy, L. Bauer, C. Hoimes, K. B. Ghaghada and E. Karathanasis, *Adv. Drug Deliv. Rev.,* 2014, 76, 79-97.

341) J. V. Jokerst, Z. Miao, C. Zavaleta, Z. Cheng and S. S. Gambhir, *Small,* 2011, 7, 625-633.

342) J. V. Jokerst, A. J. Cole, D. Van de Sompel and S. S. Gambhir, *ACS nano,* 2012, 6, 10366-10377.

343) M. F. Kircher, A. de la Zerda, J. V. Jokerst, C. L. Zavaleta, P. J. Kempen, E. Mittra, K. Pitter, R. Huang, C. Campos and F. Habte, *Nat. Med.,* 2012, 18, 829-834.

344) T. Hartman, C. S. Wondergem, N. Kumar, A. van den Berg and B. M. Weckhuysen, *The journal of physical chemistry letters,* 2016, 7, 1570-1584.

345) S. Zaleski, A. J. Wilson, M. Mattei, X. Chen, G. Goubert, M. F. Cardinal, K. A. Willets and R. P. Van Duyne, *Acc. Chem. Res.,* 2016, 49, 2023-2030.

346) R. W. Boyd, *Nonlinear optics,* Academic Press / Elsevier, Inc., Oxford, UK, 2008.

347) C. B. Milojevich, B. K. Mandrell, H. K. Turley, V. Iberi, M. D. Best and J. P. Camden, *The Journal of Physical Chemistry Letters,* 2013, 4, 3420-3423.

348) O. Kulakovich, N. Strekal, A. Yaroshevich, S. Maskevich, S. Gaponenko, I. Nabiev, U. Woggon and M. Artemyev, *Nano Letters,* 2002, 2, 1449-1452.

349) W. Park, D. Lu and S. Ahn, *Chem. Soc. Rev.,* 2015, 44, 2940-2962.

350) J. R. Lakowicz, *Anal. Biochem.,* 2004, 324, 153-169.

351) L. Novotny, *Appl. Phys. Lett.,* 1996, 69, 3806-3808.

352) O. Muskens, V. Giannini, J. Sanchez-Gil and J. Gomez Rivas, *Nano letters,* 2007, 7, 2871-2875.

353) J. Lee, A. O. Govorov, J. Dulka and N. A. Kotov, *Nano Letters,* 2004, 4, 2323-2330.

354) A. O. Govorov, Z. Fan, P. Hernandez, J. M. Slocik and R. R. Naik, *Nano letters,* 2010, 10, 1374-1382.

355) E. Dulkeith, A. Morteani, T. Niedereichholz, T. Klar, J. Feldmann, S. Levi, F. Van Veggel, D. Reinhoudt, M. Möller and D. Gittins, *Phys. Rev. Lett.,* 2002, 89, 203002.

356) E. Fort and S. Grésillon, *J. Phys. D,* 2007, 41, 013001.

357) J. R. Lakowicz, Y. Shen, S. D'Auria, J. Malicka, J. Fang, Z. Gryczynski and I. Gryczynski, *Anal. Biochem.,* 2002, 301, 261-277.

358) T. Jennings, M. Singh and G. Strouse, *J. Am. Chem. Soc.,* 2006, 128, 5462-5467.

359) N. Zhang, Y. Liu, L. Tong, K. Xu, L. Zhuo and B. Tang, *Analyst,* 2008, 133, 1176-1181.

360) M. Infusino, A. De Luca, A. Veltri, C. Vázquez-Vázquez, M. A. Correa-Duarte, R. Dhama and G. Strangi, *ACS Photonics,* 2014, 1, 371-376.

361) A. De Luca, M. P. Grzelczak, I. Pastoriza-Santos, L. M. Liz-Marzán, M. La Deda, M. Striccoli and G. Strangi, *ACS nano,* 2011, 5, 5823-5829.

362) M. Osawa, in *in Near-Field Optics and Surface Plasmon Polaritons,* ed. nonymous Springer, 2001, pp.163-187.

363) C. Huck, F. Neubrech, J. Vogt, A. Toma, D. Gerbert, J. Katzmann, T. Härtling and A. Pucci, *ACS nano,* 2014, 8, 4908-4914.

364) F. Neubrech, A. Pucci, T. W. Cornelius, S. Karim, A. García-Etxarri and J. Aizpurua, *Phys. Rev. Lett.,* 2008, 101, 157403.

365) T. Neuman, C. Huck, J. Vogt, F. Neubrech, R. Hillenbrand, J. Aizpurua and A. Pucci, *The Journal of Physical Chemistry C,* 2015, 119, 26652-26662.

366) C. D’Andrea, J. Bochterle, A. Toma, C. Huck, F. Neubrech, E. Messina, B. Fazio, O. M. Marago, E. Di Fabrizio and Lamy de La Chapelle, Marc, *ACS nano,* 2013, 7, 3522-3531.

367) G. Sciutto, M. Zangheri, S. Prati, M. Guardigli, M. Mirasoli, R. Mazzeo and A. Roda, *Top. Curr. Chem.,* 2016, 374, 1-28.

368) B. Lahiri, G. Holland, V. Aksyuk and A. Centrone, *Nano Lett.,* 2013, 13, 3218-3224.

369) J. Chae, B. Lahiri and A. Centrone, *ACS photonics,* 2015, 3, 87-95.

370) W. Ni, T. Ambjörnsson, S. P. Apell, H. Chen and J. Wang, *Nano letters,* 2009, 10, 77-84.

371) A. E. Schlather, N. Large, A. S. Urban, P. Nordlander and N. J. Halas, *Nano letters*, 2013, 13, 3281-3286.

372) H. A. Atwater and A. Polman, *Nature materials*, 2010, 9, 205-213.

373) S. Pillai and M. Green, *Solar Energy Mater. Solar Cells*, 2010, 94, 1481-1486.

374) L. Lu, T. Zheng, Q. Wu, A. M. Schneider, D. Zhao and L. Yu, *Chem. Rev.*, 2015, 115, 12666-12731.

375) N. Lagos, M. Sigalas and E. Lidorikis, *Appl. Phys. Lett.*, 2011, 99, 063304.

376) E. Lidorikis, *J. Quant. Spect. Rad. Trans.*, 2012, 113, 2573-2584.

377) G. Kakavelakis, I. Vangelidis, A. Heuer-Jungemann, A. G. Kanaras, E. Lidorikis, E. Stratakis and E. Kymakis, *Advanced Energy Materials*, 2016, 6.

378) O. M. Maragò, P. H. Jones, P. G. Gucciardi, G. Volpe and A. C. Ferrari, *Nature nanotechnology*, 2013, 8, 807-819.

379) A. Lehmuskero, P. Johansson, H. Rubinsztein-Dunlop, L. Tong and M. Kall, *ACS nano*, 2015, 9, 3453-3469.

380) E. Messina, E. Cavallaro, A. Cacciola, R. Saija, F. Borghese, P. Denti, B. Fazio, C. D’Andrea, P. G. Gucciardi, M. A. Iati, M. Meneghetti, G. Compagnini, V. Amendola and O. M. Maragò, *J. Phys. Chem. C*, 2011, 115, 5115-5122.

381) E. Messina, L. D’Urso, E. Fazio, C. Satriano, M. Donato, C. D’Andrea, O. Maragò, P. Gucciardi, G. Compagnini and F. Neri, *J. Quant. Spectr. Rad. Trans.*, 2012, 113, 2490-2498.

382) D. Spadaro, M. A. Iatì, M. G. Donato, P. G. Gucciardi, R. Saija, A. R. Cherlakola, S. Scaramuzza, V. Amendola and O. M. Maragò, *RSC Advances*, 2015, 5, 93139-93146.

383) M. L. Juan, M. Righini and R. Quidant, *Nature Photonics*, 2011, 5, 349-356.

384) A. Grigorenko, N. Roberts, M. Dickinson and Y. Zhang, *Nature Photonics*, 2008, 2, 365-370.

385) J. Arias-González and M. Nieto-Vesperinas, *JOSA A*, 2003, 20, 1201-1209.

386) V. Demergis and E. Florin, *Nano letters*, 2012, 12, 5756-5760.

387) O. Brzobohatý, M. Šiler, J. Trojek, L. Chvátal, V. Karásek and P. Zemánek, *Optics express*, 2015, 23, 8179-8189.

388) M. Pelton, M. Liu, H. Y. Kim, G. Smith, P. Guyot-Sionnest and N. F. Scherer, *Opt. Lett.*, 2006, 31, 2075-2077.

389) C. Selhuber-Unkel, I. Zins, O. Schubert, C. Sönnichsen and L. B. Oddershede, *Nano letters*, 2008, 8, 2998-3003.

390) L. Tong, V. D. Miljkovic and M. Käll, *Nano letters,* 2009, 10, 268-273.

391) P. Jones, F. Palmisano, F. Bonaccorso, P. Gucciardi, G. Calogero, A. Ferrari and O. Marago, *ACS nano,* 2009, 3, 3077-3084.

392) M. Ploschner, T. Cizmar, M. Mazilu, A. Di Falco and K. Dholakia, *Nano letters,* 2012, 12, 1923-1927.

393) B. Fazio, C. D'Andrea, A. Foti, E. Messina, A. Irrera, M. G. Donato, V. Villari, N. Micali, O. M. Maragò and P. G. Gucciardi, *Scientific reports,* 2016, 6, 26952.

394) S. Nedev, A. S. Urban, A. A. Lutich and J. Feldmann, *Nano letters,* 2011, 11, 5066-5070.

395) Y. Seol, A. E. Carpenter and T. T. Perkins, *Opt. Lett.,* 2006, 31, 2429-2431.

396) P. M. Bendix, S. N. S. Reihani and L. B. Oddershede, *ACS nano,* 2010, 4, 2256-2262.

397) M. Šiler, J. Ježek, P. Jákl, Z. Pilát and P. Zemánek, *Opt. Lett.,* 2016, 41, 870-873.

398) C. McDougall, D. J. Stevenson, C. T. Brown, F. Gunn-Moore and K. Dholakia, *Journal of biophotonics,* 2009, 2, 736-743.

399) M. Righini, P. Ghenuche, S. Cherukulappurath, V. Myroshnychenko, García de Abajo, Francisco Javier and R. Quidant, *Nano letters,* 2009, 9, 3387-3391.

400) S. Jones, A. A. Al Balushi and R. Gordon, *Journal of Optics,* 2015, 17, 102001.

401) V. K. Valev, J. J. Baumberg, C. Sibilia and T. Verbiest, *Adv Mater,* 2013, 25, 2517-2534.

402) S. Gao, J. Liu and W. Zhang, *The Journal of Physical Chemistry C,* 2016, 120, 10500-10505.

403) M. Schäferling, D. Dregely, M. Hentschel and H. Giessen, *Physical Review X,* 2012, 2, 031010.

404) J. Majoinen, J. Hassinen, J. S. Haataja, H. T. Rekola, E. Kontturi, M. A. Kostiainen, R. H. Ras, P. Törmä and O. Ikkala, *Adv Mater,* 2016, .

405) A. Cecconello, J. S. Kahn, C. Lu, L. Khosravi Khorashad, A. O. Govorov and I. Willner, *J. Am. Chem. Soc.,* 2016, .

406) Y. Zhao, Y. Yang, J. Zhao, P. Weng, Q. Pang and Q. Song, *Adv Mater,* 2016, .

407) G. Armelles, A. Cebollada, A. Garcia-Martin and M. U. Gonzalez, *Adv. Opt. Mater.,* 2013, 1, 2-2.

408) I. S. Maksymov, *Reviews in Physics,* 2016, 1, 36-51.

409) S. Scaramuzza, D. Badocco, P. Pastore, D. F. Coral, Fernández van Raap, Marcela B and V. Amendola, *ChemPhysChem,* 2016, .

410) B. Sanavio and F. Stellacci, *Curr. Med. Chem.*, 2016, 23.

411) L. Huang, L. Ao, D. Hu, W. Wang, Z. Sheng and W. Su, *Chemistry of Materials*, 2016, 28, 5896-5904.

412) W. Chen, N. Xu, L. Xu, L. Wang, Z. Li, W. Ma, Y. Zhu, C. Xu and N. A. Kotov, *Macromolecular rapid communications*, 2010, 31, 228-236.

413) K. Lodewijks, N. Maccaferri, T. Pakizeh, R. K. Dumas, I. Zubritskaya, J. Åkerman, P. Vavassori and A. Dmitriev, *Nano letters*, 2014, 14, 7207-7214.

414) M. Manera, G. Pellegrini, P. Lupo, V. Bello, C. de Julián Fernández, F. Casoli, S. Rella, C. Malitesta, F. Albertini and G. Mattei, *Sensors Actuators B: Chem.*, 2017, 239, 100-112.

415) F. Pineider, G. Campo, V. Bonanni, C. de Julián Fernández, G. Mattei, A. Caneschi, D. Gatteschi and C. Sangregorio, *Nano letters*, 2013, 13, 4785-4789.

416) B. Sepúlveda, J. B. González-Díaz, A. García-Martín, L. M. Lechuga and G. Armelles, *Phys. Rev. Lett.*, 2010, 104, 147401.

417) P. K. Jain, Y. Xiao, R. Walsworth and A. E. Cohen, *Nano Lett.*, 2009, 9, 1644-1650.

418) L. Bogani, L. Cavigli, C. de Julián Fernández, P. Mazzoldi, G. Mattei, M. Gurioli, M. Dressel and D. Gatteschi, *Adv. Mater.*, 2010, 22, 4054–4058.

419) B. Metzger, M. Hentschel and H. Giessen, *ACS Photonics*, 2016, .

420) F. Hache, D. Ricard, C. Flytzanis and U. Kreibig, *Applied Physics A*, 1988, 47, 347-357.

421) C. Torres-Torres, A. López-Suárez, B. Can-Uc, R. Rangel-Rojo, L. Tamayo-Rivera and A. Oliver, *Nanotechnology*, 2015, 26, 295701.

422) Y. Wang, X. Xie and T. Goodson, *Nano letters*, 2005, 5, 2379-2384.

423) B. Metzger, M. Hentschel, T. Schumacher, M. Lippitz, X. Ye, C. B. Murray, B. Knabe, K. Buse and H. Giessen, *Nano letters*, 2014, 14, 2867-2872.

424) M. Celebrano, X. Wu, M. Baselli, S. Großmann, P. Biagioni, A. Locatelli, C. De Angelis, G. Cerullo, R. Osellame and B. Hecht, *Nature nanotechnology*, 2015, 10, 412-417.

425) G. F. Walsh and L. Dal Negro, *Nano letters*, 2013, 13, 3111-3117.

426) A. Belardini, A. Benedetti, M. Centini, G. Leahu, F. Mura, S. Sennato, C. Sibilia, V. Robbiano, M. C. Giordano and C. Martella, *Advanced Optical Materials*, 2014, 2, 208-213.

427) G. Grinblat, M. Rahmani, E. Cortés, M. Caldarola, D. Comedi, S. A. Maier and A. V. Bragas, *Nano letters*, 2014, 14, 6660-6665.

428) M. Mesch, B. Metzger, M. Hentschel and H. Giessen, *Nano letters*, 2016, 16, 3155-3159.

429) S. Shen, L. Meng, Y. Zhang, J. Han, Z. Ma, S. Hu, Y. He, J. Li, B. Ren and T. Shih, *Nano letters*, 2015, 15, 6716-6721.

430) C. X. Zhang, Y. Zhang, X. Wang, Z. M. Tang and Z. H. Lu, *Anal. Biochem.*, 2003, 320, 136-140.

431) R. A. Farrer, F. L. Butterfield, V. W. Chen and J. T. Fourkas, *Nano letters,* 2005, 5, 1139-1142.

432) P. Biagioni, D. Brida, J. Huang, J. Kern, L. Duò, B. Hecht, M. Finazzi and G. Cerullo, *Nano letters*, 2012, 12, 2941-2947.

433) J. Wang, J. Butet, A. Baudrion, A. Horrer, G. Lévêque, O. J. Martin, A. J. Meixner, M. Fleischer, P. Adam and A. Horneber, *The Journal of Physical Chemistry C,* 2016, 120, 17699-17710.

434) Y. Chen, P. Lee, P. Shen, J. Launer, R. Oketani, K. Li, Y. Huang, K. Masui, S. Shoji and K. Fujita, *ACS Photonics*, 2016, .

435) V. Amendola, D. Dini, S. Polizzi, J. Shen, K. M. Kadish, M. J. F. Calvete, M. Hanack and M. Meneghetti, *J. Phys. Chem. C*, 2009, 113, 8688-8695.

436) L. François, M. Mostafavi, J. Belloni and J. A. Delaire, *Physical Chemistry Chemical Physics,* 2001, 3, 4965-4971.

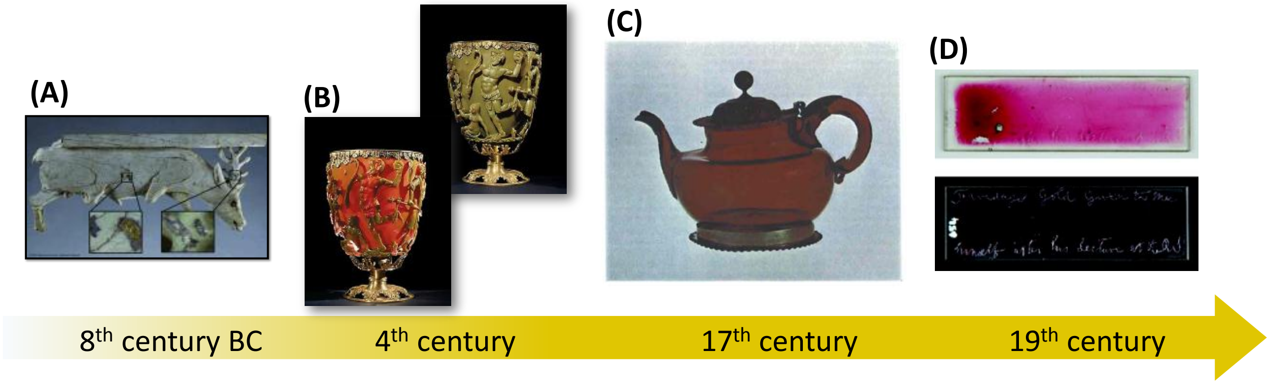

Figure 1. Due to their intense coloration, Au NPs are found in human products since thousands of years. (A) Egyptian Gold-Plated Archaeological Ivory (8th century BC, Louvre collection originated from Arslan Tash, Syria). (B) The 4th-century Roman Lycurgus Cup, which appears red when illuminated from behind and green when illuminated from the front (British Museum). (C) Tea-pot (1680) obtained by Johann KunckeI using the “Purple of Cassius” technique. (D) Michael Faraday’s original gold colloid samples (1852); the inscription reads “Faraday’s gold given to me himself after his lecture at the RI” (Whipple Museum of the History of Science). Images reprinted with permissions from ref.[25] (A) ,[23] (C),[34] (D).

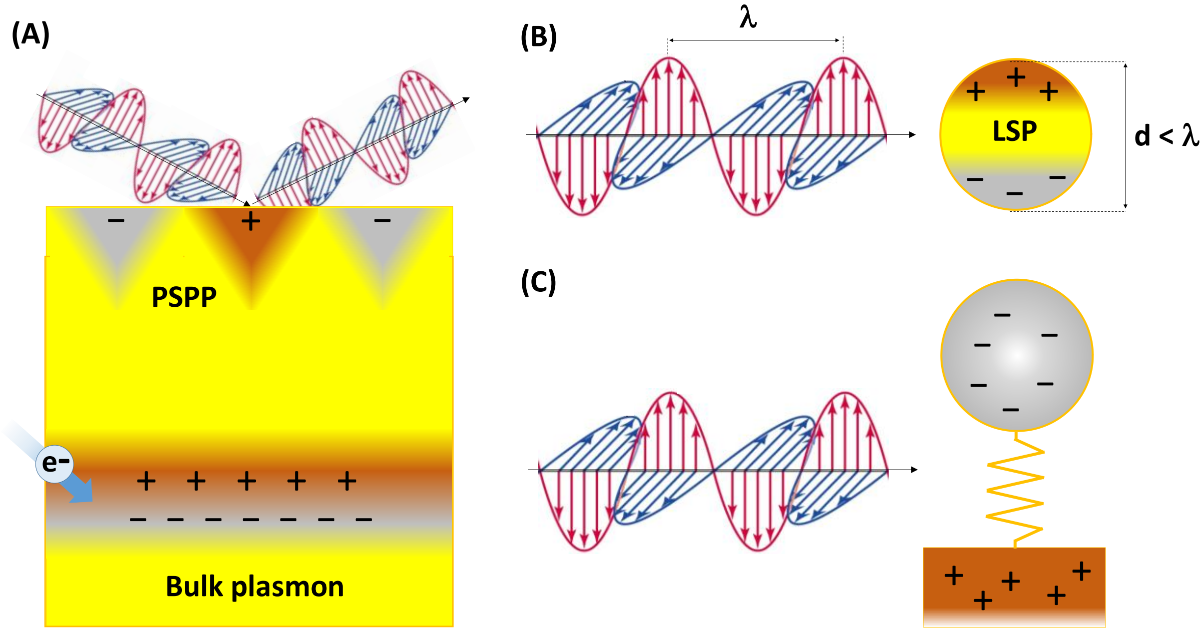

Figure 2. Graphical illustration of plasmons in bulk gold (A) and NPs (B). (A) Bulk plasmons can be excited by an electron beam (bottom), while PSPPd are excited by the evanescent field of light (top). (B) LSPs are excited by light propagating in free space or dielectric media. (C) The LSP in Au NPs can be modelled, as a first approximation, like a spring-mass harmonic oscillator, where the free electrons density is equivalent to the mass.

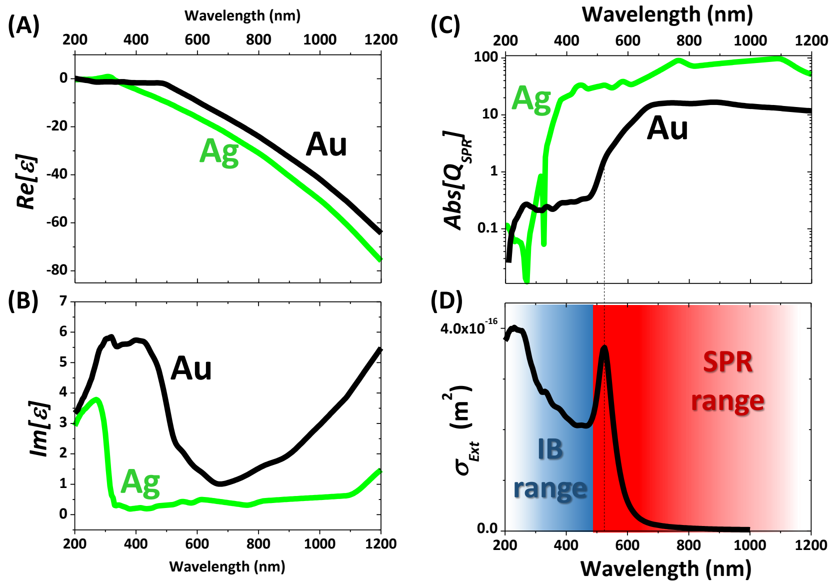

Figure 3. Plot of *Re[ε]* (A) and *Im[ε]* (B) for Au (black) and Ag (green), as reported in ref.[149]. (C) Semi-log plot of Q_{SPR} (in absolute value) for Au and Ag (adapted from ref.[65]). (D) Extinction spectrum of spherical Au NPs (20 nm diameter, in water, calculated with the Mie model). Onset of interband (IB) and SPR regions are highlighted in blue and red respectively.

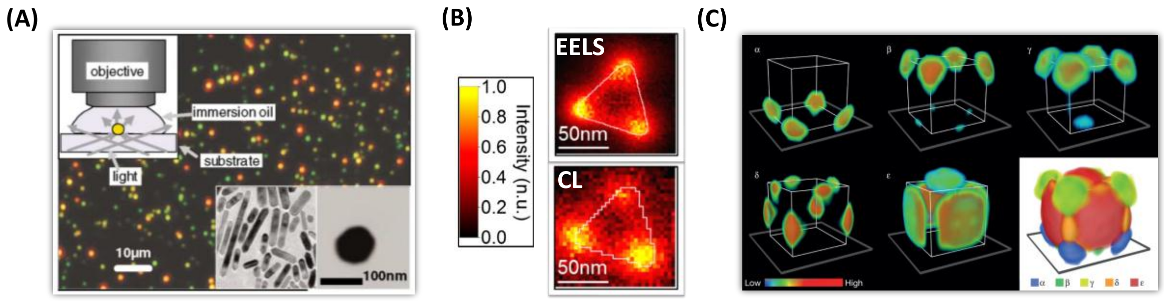

Figure 4. (A) Photograph of Au nanorods (red colour, bottom left inset) and 60 nm nanospheres (green colour, bottom right inset) in dark-field illumination (inset upper left). Reprinted with permissions from ref.[45]. (B) EELS (top) and CL (bottom) maps of the dipolar LSP in an Au nanprism. Reprinted with permissions from ref.[50]. (C) 3D LSP mapping of a plasmonic nanocube. The colour bar indicates the SPR intensity for the five LSP modes considered. Reprinted with permissions from ref.[48].

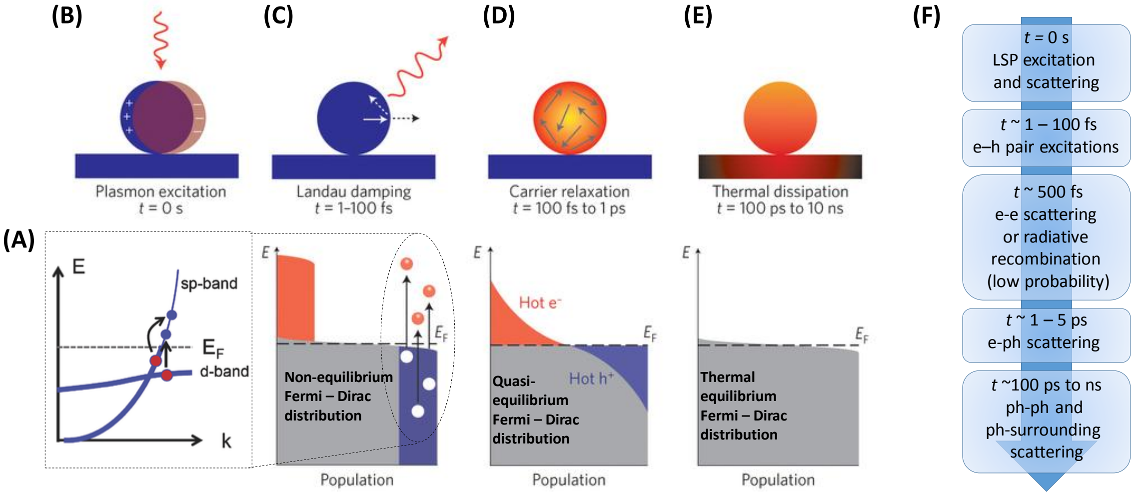

Figure 5. (A) Formation of electron-hole pairs in Au can be either intraband or interband. After LSP excitation (B), the athermal distribution of electron–hole (e-h) pairs decays in 1 – 100 fs by photon emission (radiatively) or through Landau damping and formation of hot carriers (non radiatively) (C). Hot carriers redistribute their energy by electron–electron scattering on a timescale ranging from 100 fs to 1 ps (D). Then, heat is transferred inside the NP by electron-phonon (e-ph) scattering on a timescale of few ps, and from the NP to the surroundings on a timescale of several ps to ns (E). The Fermi electron population is reported in grey, hot electrons are represented by the red areas above the Fermi energy (E_F) and hot hole distributions are represented by the blue area below E_F. Adapted with permission from ref.[60]. (F) The complete timeline of SPR relaxation.

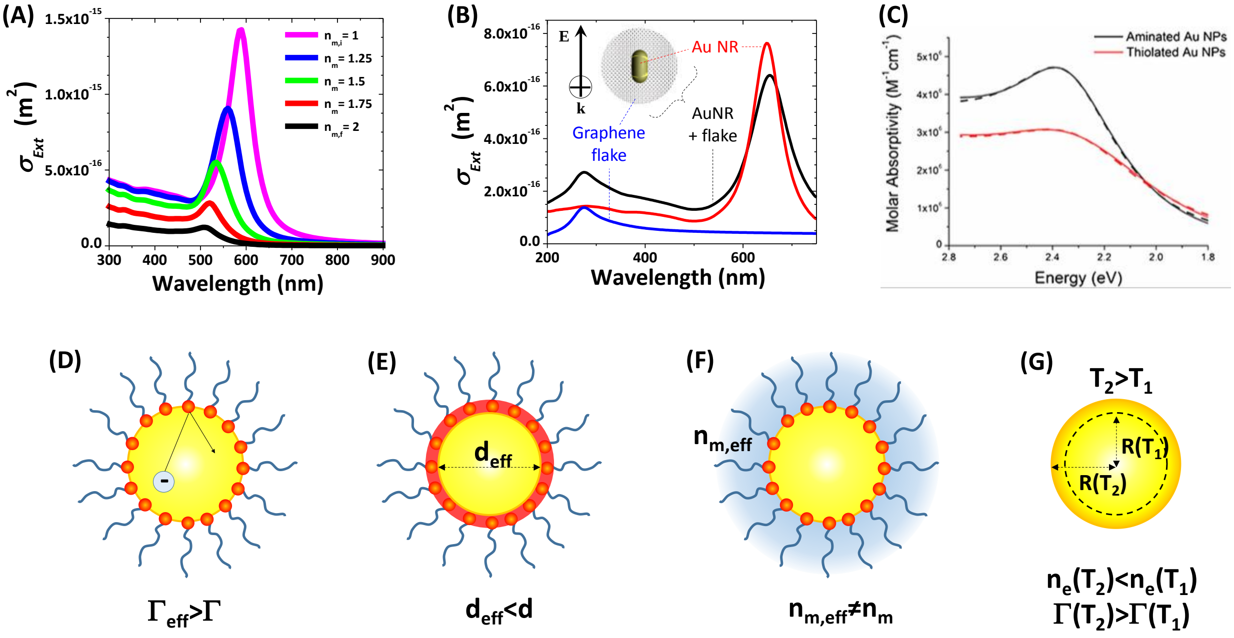

Figure 6. (A) Mie model calculation of the SPR of a 20 nm Au NP in a non absorbing dielectric matrix with refractive index increasing from n_i=1 (black line) to n_f=2 (with Δn=0.25). (B) Numerical calculations of SPR quenching in an Au nanorod (10 nm x 25 nm) faced to a 50 nm circular graphene flake with 1 nm of interparticle gap. Reproduced with permission from ref.[65]. (C) UV-vis spectra on 3.5 nm Au NPs coated with different ligands (thiols or amines) show that CID depends on the type of adsorbates (adapted with permissions from ref.[57]). In general, adsorbates induce three effects on the Au NPs: increase of Γ (D), decrease of effective NPs size d (E), change in the effective permittivity of the surrounding matrix $n_{m,eff}$ (F). (G) T increase implies NPs dilatation, with decrease of electron density n_e, and a larger Γ.

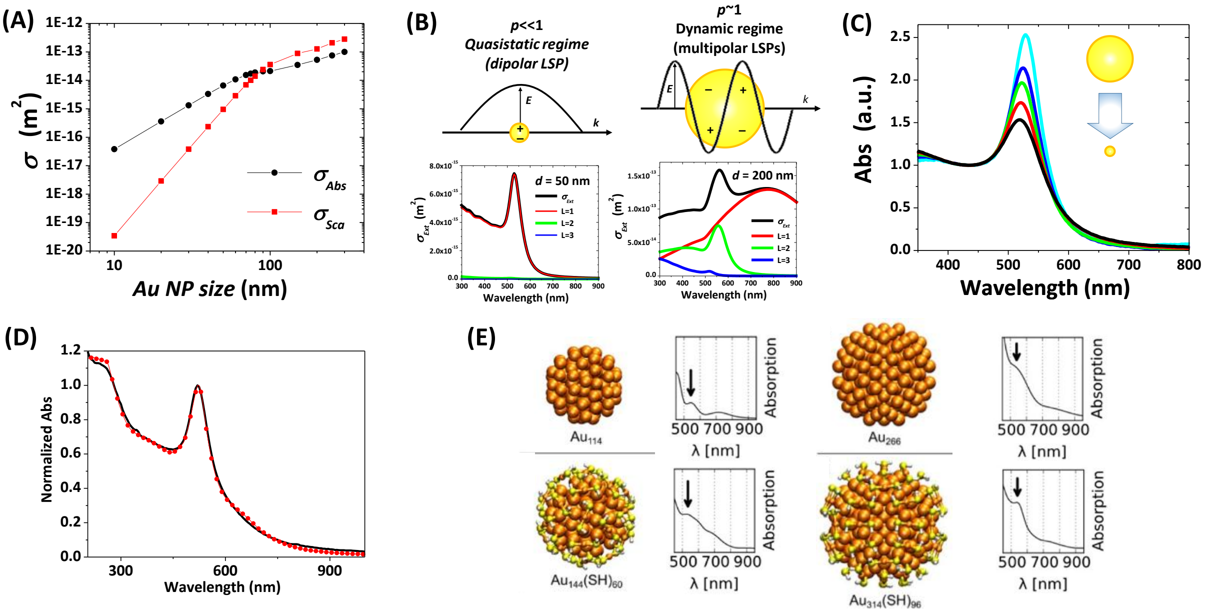

Figure 7. (A) Mie calculations of maximum plasmon σ_{Abs} (black) and σ_{Sca} (red) in isolated Au nanospheres dispersed in water matrix. The spectral range 400 – 1200 nm was considered. Spectral position of SPR maxima for σ_{Abs} and σ_{Sca} usually do not coincide. (B) Contribution of dipolar (red), quadrupolar (green) and octupolar (blue) LSP to the σ_{Ext} (black) in Au nanospheres with size of 10, 50, 100 and 200 nm. (C) SPR broadening and damping in Au nanospheres with size decreasing from to 5 to 25 nm (adapted with permission from ref.[86]). (D) Fit of experimental Au NPs optical absorption spectrum with a Mie – Gans model. Adapted with permission from ref.[43]. (E) Calculated absorption spectra of small Au clusters (114, 144, 266 and 314 atoms). The 144 and 314 clusters are coated by a monolayer of thiols as indicated in the figure. Adapted with permission from ref.[73].

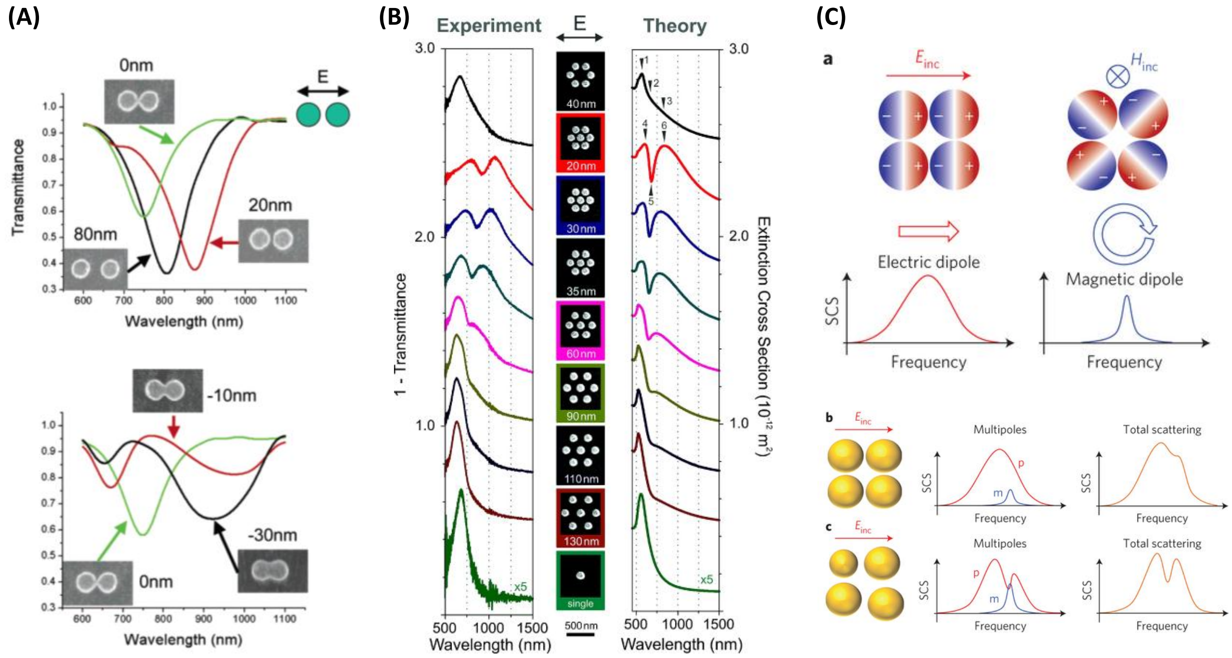

Figure 8. (A) Polarized transmission spectra in periodic arrays of Au nanodisks with variable interparticle gap (left: positive gap; right: negative gap). Reprinted with permission from ref.[104]. (B) Appearance of Fano resonance in Au nanodisks assemblies over glass substrate in air when interparticle gap goes above the threshold of about 60 nm. Left column: experimental extinction spectra. The presence or absence of the central nanoparticle can switch on or off the formation of the Fano resonance. Middle column: SEM images of the corresponding Au NPs. Right column: simulated extinction cross-section spectra. Reprinted with permission from ref.[109]. (C) As shown by the Au NPs quadrumer ring in (a), charge currents associated to electric SPR have a dipolar character (i.e. the ring of NPs behave as an electric dipole), while MPR are associated to a circulating displacement current and hence the ring of NPs behave as a magnetic dipole. E_{inc} and H_{inc} represent the incident electric and magnetic fields, respectively. Colours indicate the charge distribution (b-c) The ring shape and interparticle gap determine the relative intensity and spectral position of the electric and magnetic resonances. For instance, symmetry-breaking (c) induces interference between the electric dipole (p) and magnetic dipole (m) modes, which gives rise to a pronounced Fano resonance in the scattering spectrum. Reprinted with permission from ref.[111].

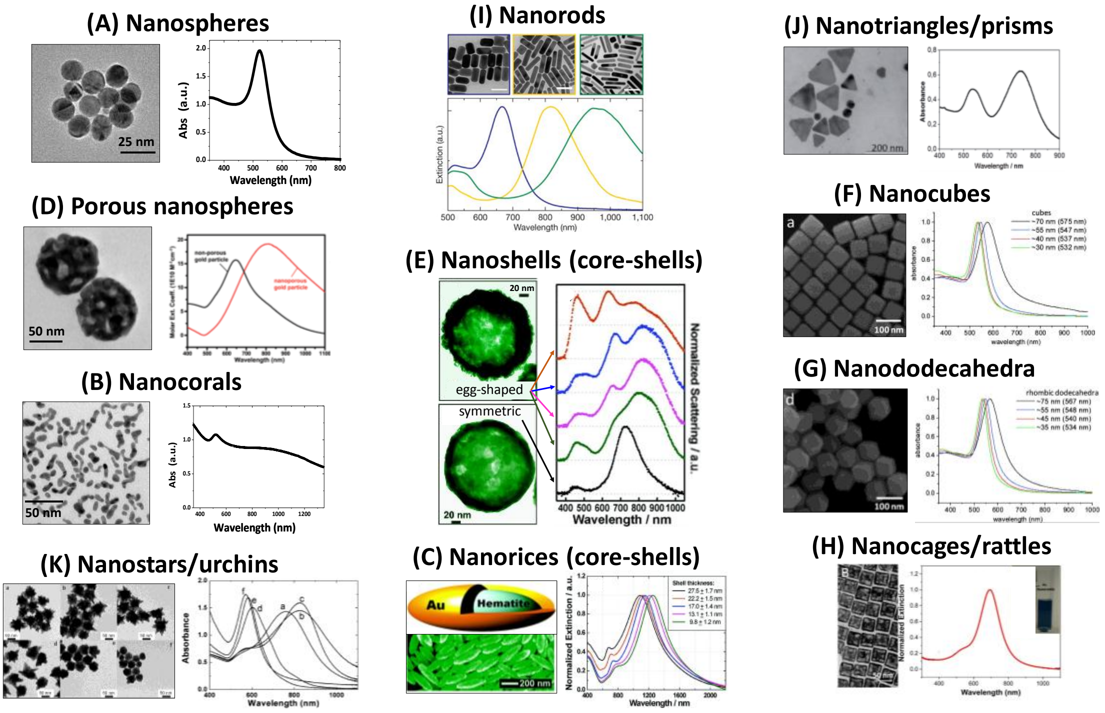

Figure 9. Au NPs with different shape and corresponding optical extinction (transmission) or scattering (dark field) spectra. Images adapted with permissions from the following references: nanospheres[86] porous nanospheres,[115] nanocorals,[81] nanostars (or nanourchins),[118] nanorods,[232] nanotriangles (or nanoprisms),[119] nanoshells and nanorices,[191] nanocubes and (rhombic) nanododecahedra,[120] nanocages (or nanorattles).[121]

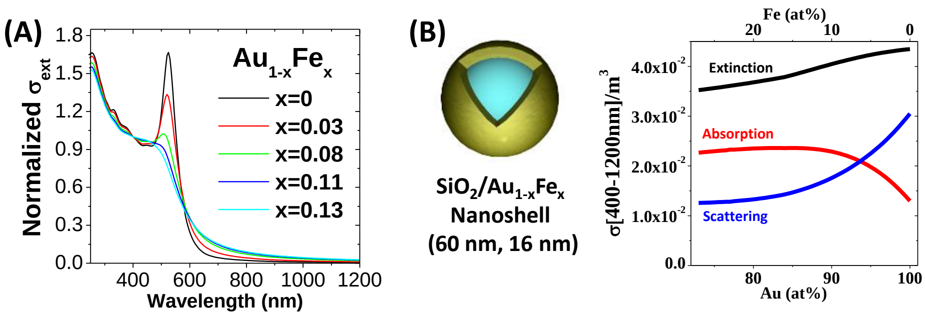

Figure 10. Calculated (Mie model) optical extinction spectra for Au$_{1-x}$Fe$_x$ alloy nanospheres in water, with 0<x<0.13. Reprinted with permission from ref.[128]. Integral in the 400 – 1200 nm range of the cross section for Au-Fe alloy nanoshell (calculated with the Mie model) versus composition.

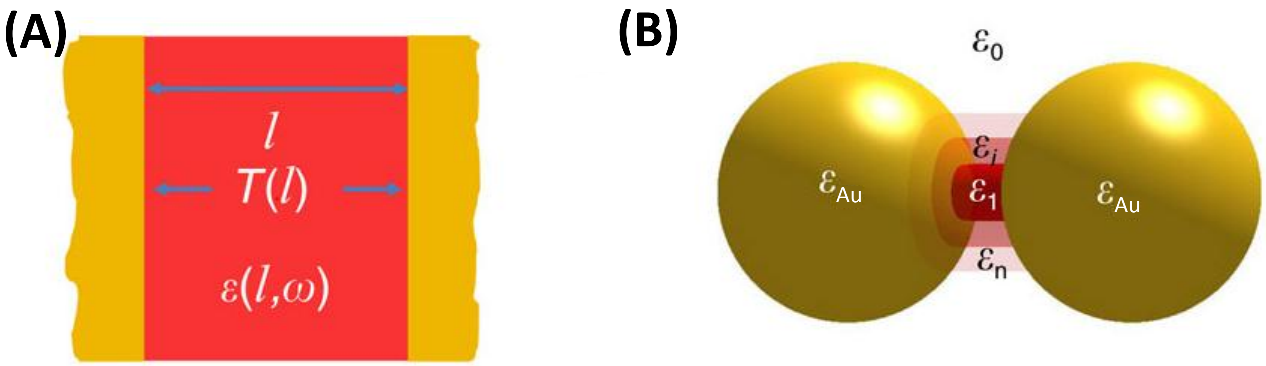

Figure 11. (A) In the ideal case of two semi-infinite Au surfaces separated by a distance l and characterized by tunnelling transmission $T(l)$, the tunnelling-induced conductivity between the surfaces defines the l-dependent dielectric material $\varepsilon_m(l, \omega)$ used in the QCM. (B) In the more realistic case of curved surfaces, the inhomogeneous distribution of the local dielectric constant used in the QCM is accounted for by using a fictitious concentric multilayer of separation-dependent medium dielectric constants (three shells are shown in this example). Reprinted with permission from ref.[158].

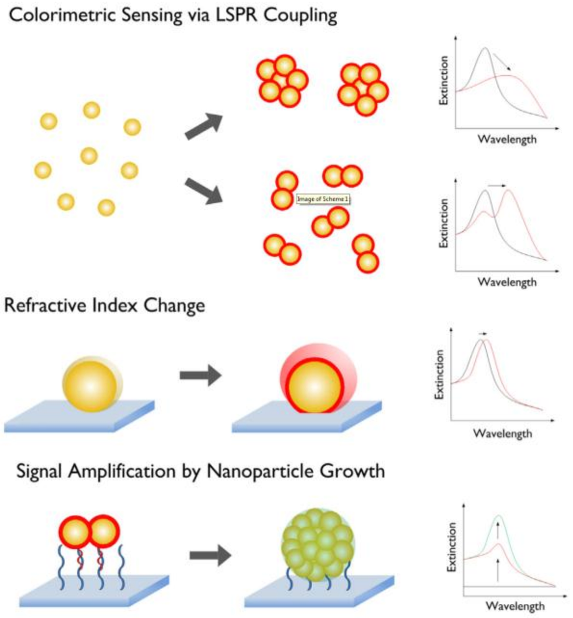

Figure 12. Illustration of different strategies for SPR sensing: colorimetric change by NPs aggregation (top), SPR shift due to change in the physical-chemical environment (middle) or Au NPs structural changes (bottom). Reprinted with permission from ref.[199].

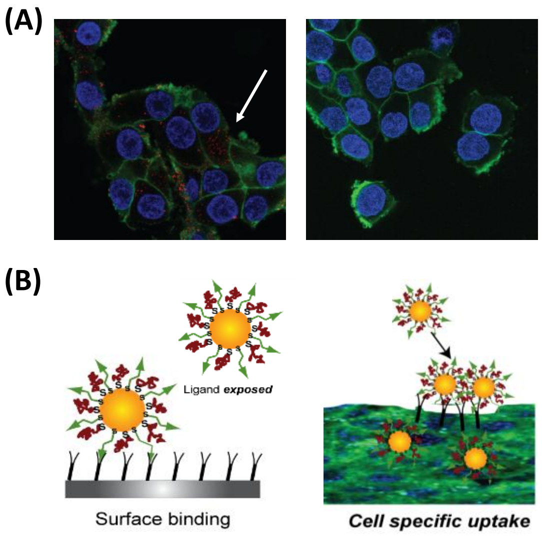

Figure 13. (A) Dark field optical microscope images of KB cells incubated with targeted (left) or untargeted (right) Au NPs. Only in the left image, Au NPs are visible inside cells as red spots. Cell nuclei are stained in blue and cell membrane in green. (B) The general concept for selective binding between analytes or biological targets requires that Au NPs are surface functionalized with chemical recognizing units capable (sketched as green arrows in the figure). Adapted with permission from ref.[224].

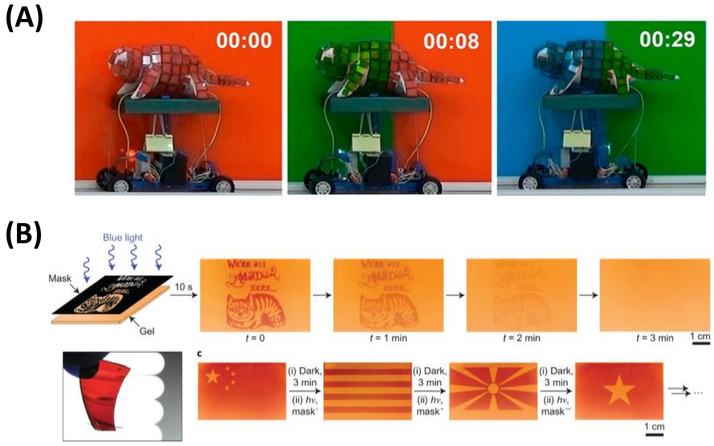

Figure 14. (A) Plasmonic "chameleon" assembled from electrochemically responsive Au Nps substrate. The chameleon changes color depending to the backgrounds, by connection of the responsive plasmonic "skin" to a photodetector. Reprinted with permission from ref.[231]. (B) Photopatternable gel containing a solution of Au NPs. The solution appears red when particles are dispersed and yellow when they are aggregated, due to dominating absorption of a yellow dye added to the solution. The gel is self erasing after photopatterining, and can be impressed multiple times.[233]

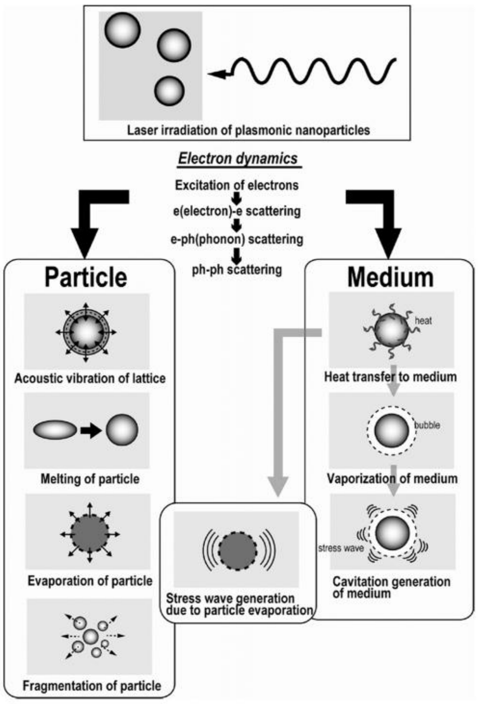

Figure 15. Possible phenomena occurring after interaction of laser light with Au NPs. Reprinted with permission from ref.[238].

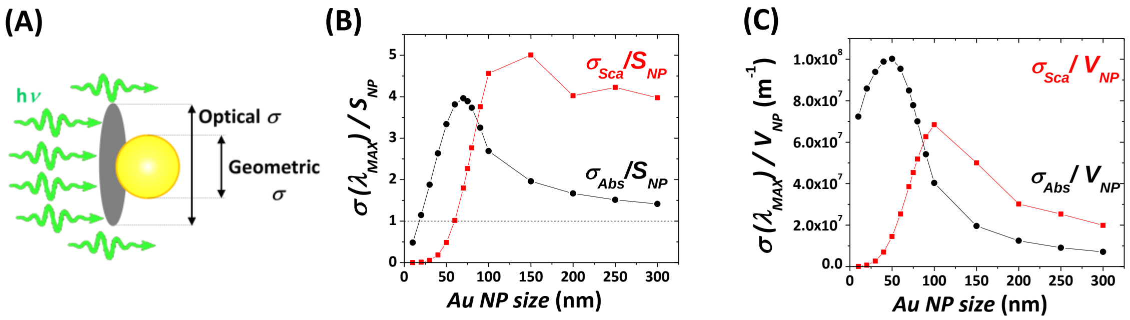

Figure 16. (A) Geometric and optical σ do not correspond, as shown by the plot of σ_{Abs}/V_{NP} and σ_{Sca}/V_{NP} (B), σ_{Abs}/S_{NP} and σ_{Sca}/S_{NP} (C) measured at SPR maximum for Au nanospheres in water (Mie model calculations).

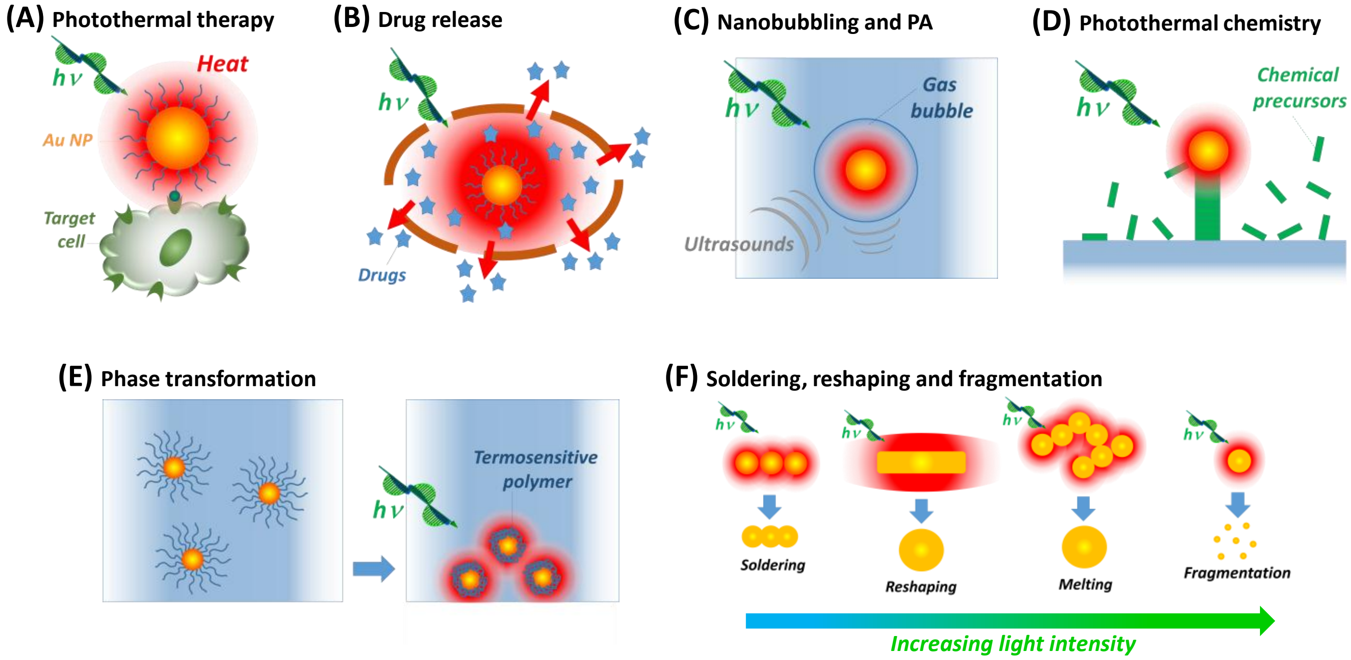

Figure 17. Pictorial sketch of main applications related to photothermal heating in Au NPs: (A) PT for destruction of malignant cells (possibly associated to selective targeting); (B) enhancement of drug diffusion from nanocargoes towards the target; (C) generation of nanobubbles, exploitable for enhancement of contrast during PA imaging; (D) Activation of chemical reactions with nanoscale resolution; (E) Phase transition, for instance in thermosensitive polymers which go from hydrophilic to hydrophobic state above a critical *T*; (F) Soldering, reshaping, melting or fragmentation of Au NPs, depending on starting nanomaterial and light intensity.

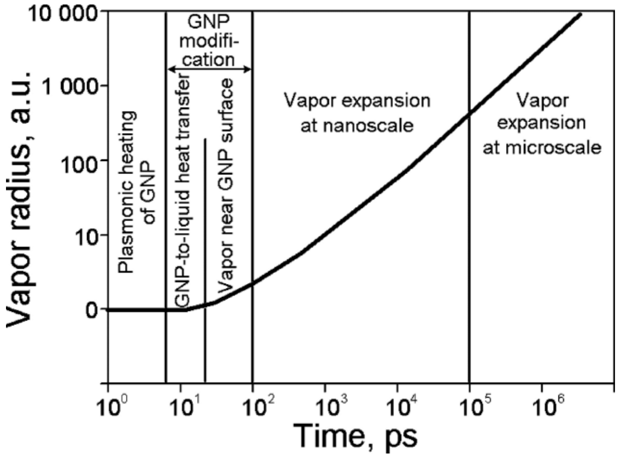

Figure 18. Temporal sequence of processes involved in the generation of nanobubbles after excitation of the SPR in Au NPs. Reprinted with permission from ref.[260].

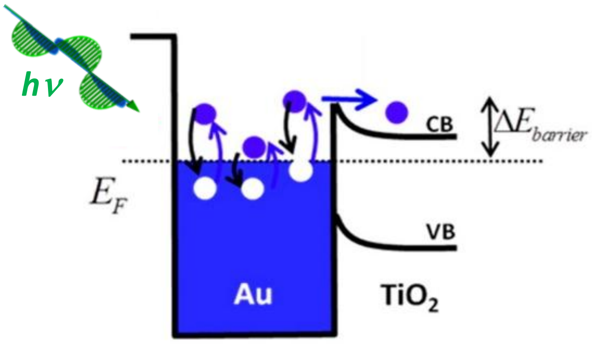

Figure 19. Pictorial sketch of hot-carriers generation during SPR excitation and charge injection in nearby acceptor material (TiO_2 in this case), when acceptor energy levels are close to the Fermi level of the Au NP ($\Delta E_{barrier} \rightarrow 0$). Reprinted with permission from ref.[279].

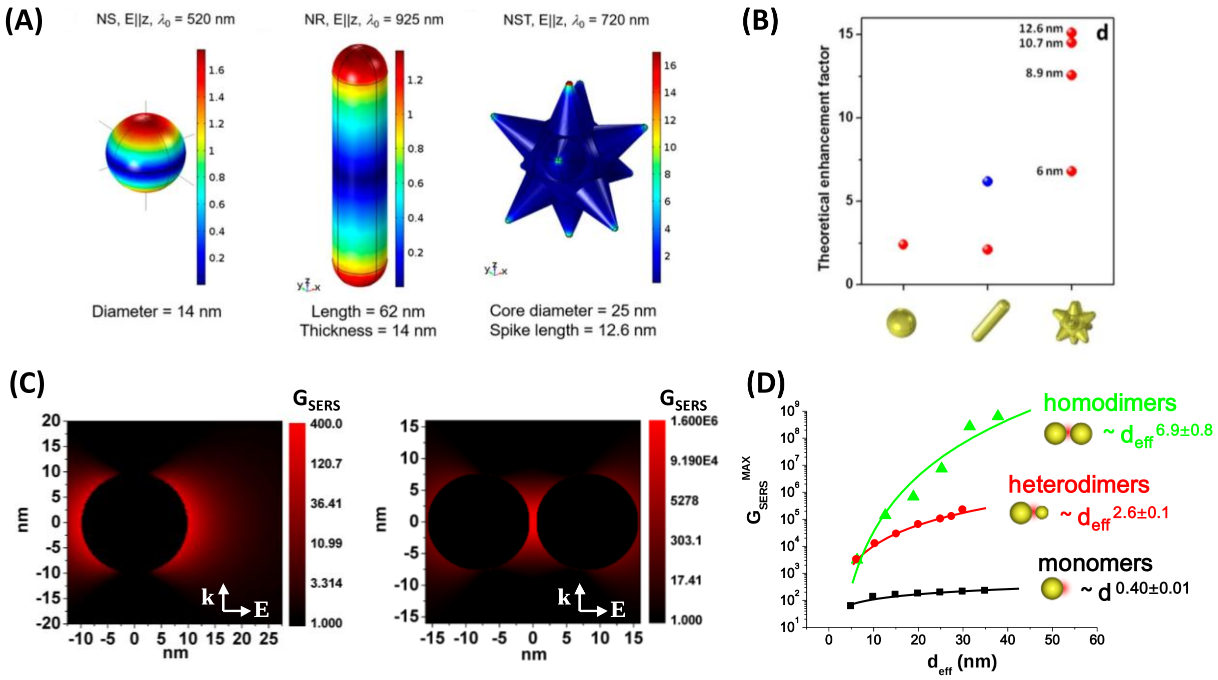

Figure 20. (A) Local field (E_{loc}) maps calculated for Au nanosphere, nanorod and nanostar (structural parameters are indicated in the figure). at the wavelength of maximum SPR intensity. (B) Theoretical enhancement factors for the three different morphologies (in case of the nanostar, also different spike lengths, at parity of core size, are considered). The blue dot corresponds to the enhancement factor of the Au nanorod when it is parallel to the incident electric field vector. Reprinted with permission from ref.[279]. (C) G_{SERS} map in Au NP monomer (20 nm) or dimer (gap 1 nm). (D) Plot of maximum G_{SERS} versus Au NPs morphology (monomers, heterodimers and homodimers with different size). Reprinted with permission from ref.[301].

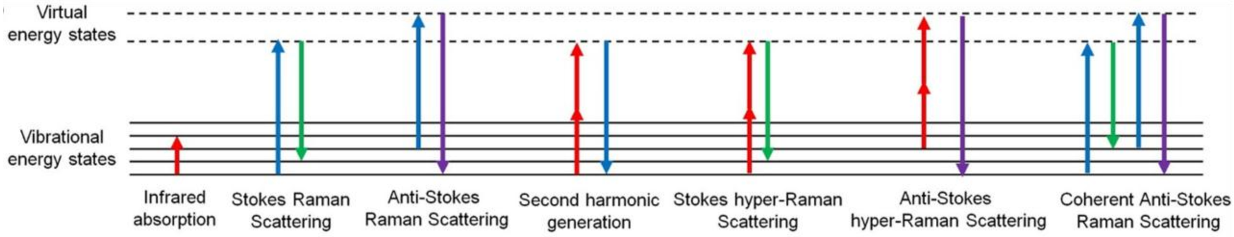

Figure 21. Jablonski diagram illustrating IR, Raman, SHG, HRS and CARS spectroscopy. To each colour corresponds a definite frequency. Reprinted with permission from ref.[295].

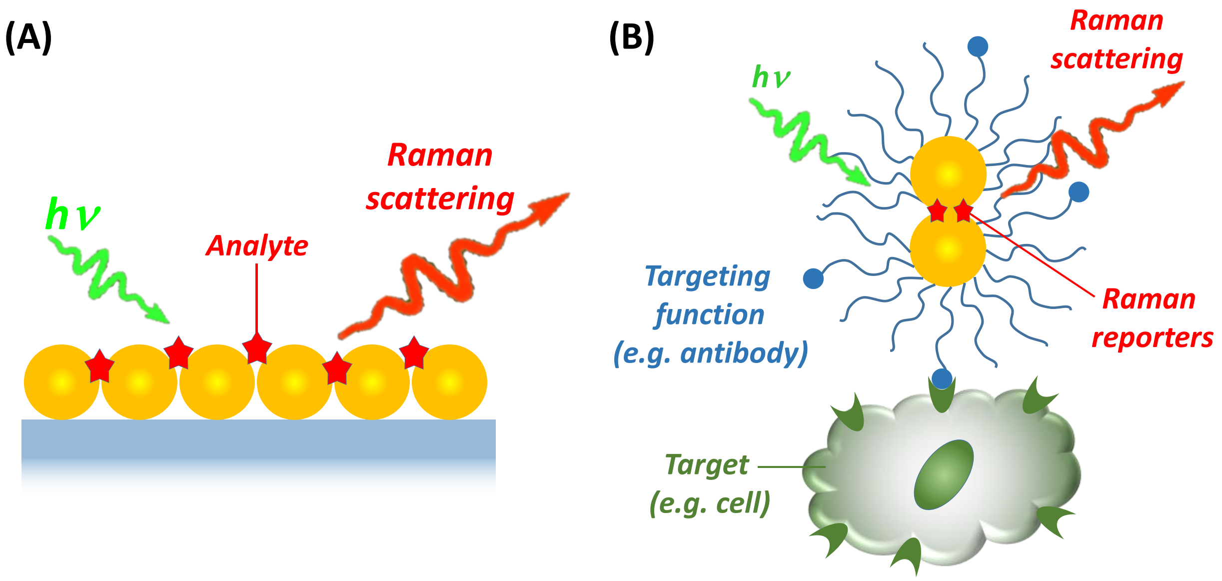

Figure 22. SERS is exploited for ultrasensitive detection of analytes by Raman spectroscopy (A) or for ultra-bright labeling of target samples (B). In (A), the analyte emits intense Raman signals when deposed on the Au NPs substrate. In (B), Au NPs are loaded with a Raman-active dye (reporter) and a targeting function, so that the target analyte is detected by the intense Raman signal after binding of the SERS label to it.

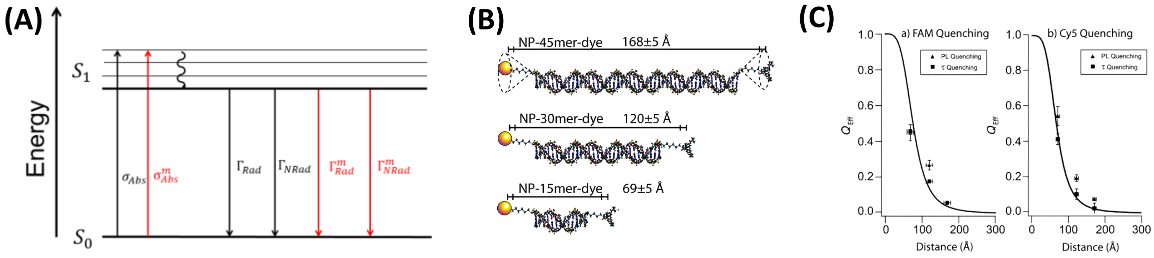

Figure 23. (A) Simplified Jablonski diagram for a fluorophore in free space (black arrows and labels) and in presence of the metallic substrate (red straight arrows and labels). Γ_{Rad} and Γ_{NRad} are the radiative and non-radiative decay rates without metal; Γ^{Au}_{Rad} and Γ^{Au}_{NRad} are the additional contributions brought about by the metal. σ_{Abs} and σ^{Au}_{Abs} represent the absorption cross sections of the molecule in free space and in presence of the metal. Notice that Γ^{Au}_{Rad} and Γ^{Au}_{NRad} are additive contributions to the corresponding quantities in free space; σ^{Au}_{Abs} instead is the enhanced cross section and not an additive contribution to σ_{Abs}. (B) In a fluorescence quenching experiment, DNA strands of different lengths were used as spacer to vary the distance between the dyes (fluoresceine and Cyanine 5) and Au NPs. (C) Quantum efficiency of energy transfer (Q_{eff}) follows a $1/r^4$ distance dependence for both dyes. Reprinted with permission from ref.[358].

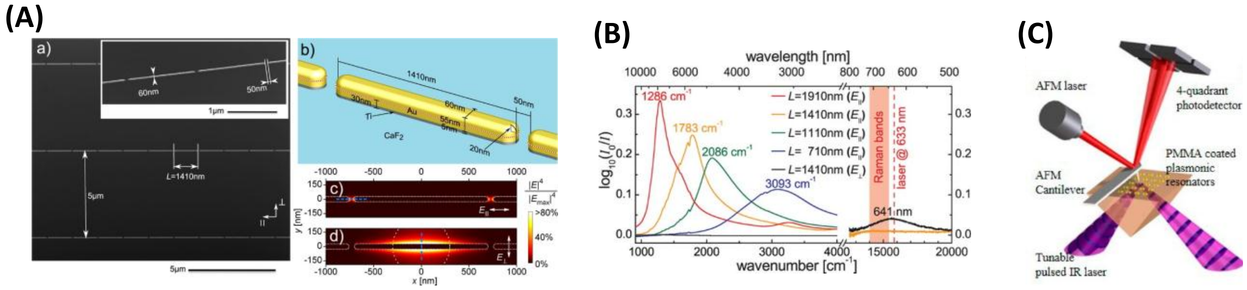

Figure 24. (A) SEM image of the Au nanoantennas for SEIRA (a), and structural parameters (b). In (c) the local field maps for excitation along the longitudinal and transversal axis are shown. (B) IR and visible extinction spectra of nanoantennas with different shape (red line: L = 1910 nm, orange line: L = 1410 nm, green line: L = 1110 nm, blue line: L = 710 nm). The spectra are acquired with light polarized parallel (longitudinal, $E_{||}$) and perpendicular (transversal, $E_{\perp}$) to the nanoantennas. In the visible, the plasmonic resonance is independent of the antenna length, thus only the results of one set of antennas (L = 1410 nm) are displayed. Reprinted with permission from ref.[366]. (C) Sketch of the PTIR measurement setup, where signal intensity is determined by the maximum amplitude of the cantilever which is proportional to the energy absorbed by the sample. Reprinted with permission from ref.[369].

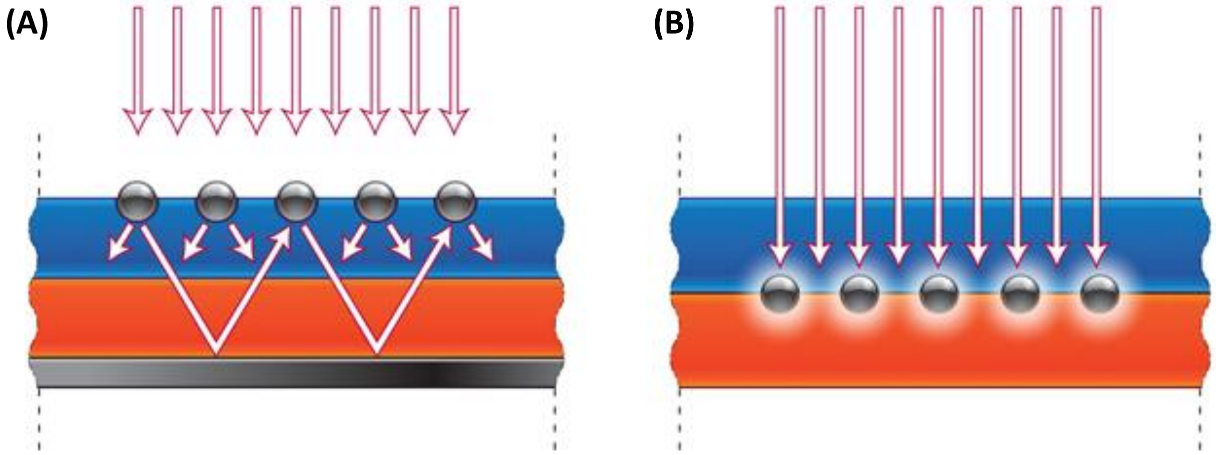

Figure 25. Two different mechanisms and arrangements can be exploited to improve the efficiency of a solar cell with plasmonic nanoparticles. a): Light scattering; b) Light concentration. The blue and red areas represent, for instance, the p- and n- doped layers of a Si cell. Reprinted with permission from ref.[372].

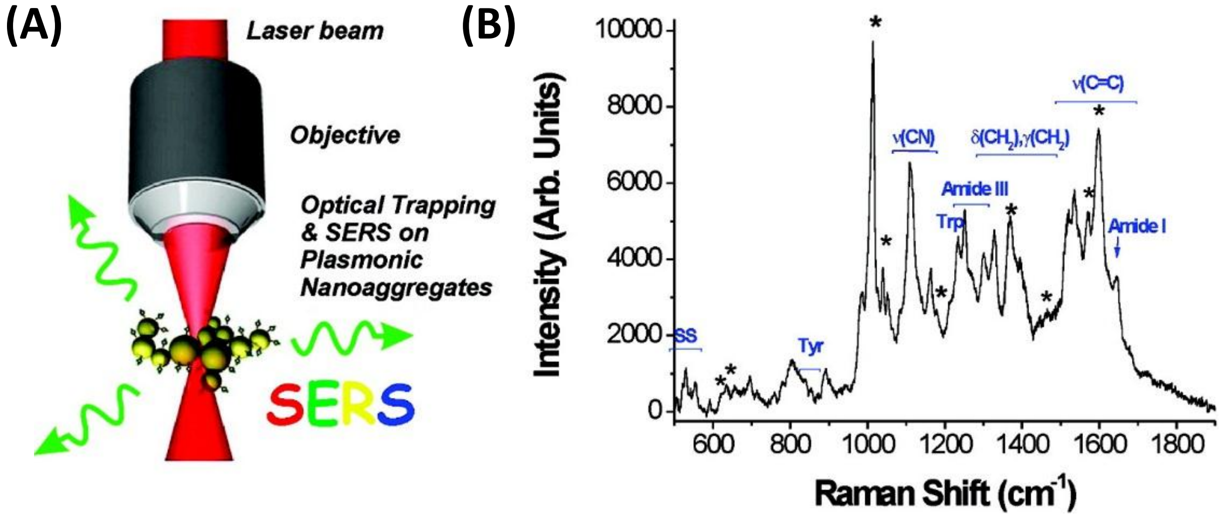

Figure 26. (A) Simplified sketch of the Raman tweezers. (B) Raman signals from the molecules adsorbed on the trapped Au NPs is collected through the same objective used for trapping. In this spectra, pyridine and bovine serum albumin vibrational peaks, adsorbed on the surface of a trapped aggregate of Au NPs, where detected. Reprinted with permission from ref.[380].

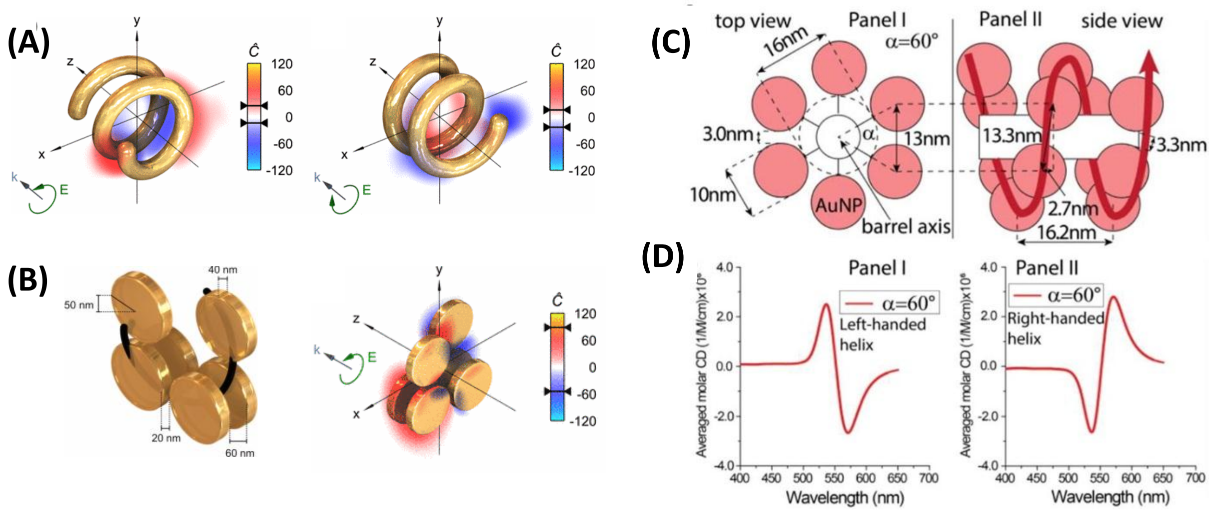

Figure 27. Helical structures are the most intuitive examples for a chiral plasmonic nanostructures, and can be obtained by a single helical object (A), or by assembling nonchiral Au NPs along a chiral path, such as the DNA helix (B-C). (A) Optical chirality enhancement ($\hat{C}$) in a nearby chiral molecule for a left-handed Au helix with left-handed circularly polarized light (left) and its enantiomer (right). For helix diameter and height of the helix of 400 nm and Au thickness of 80 nm, the enhancement is observed for a excitation at 2030 nm. The sign of $\hat{C}$ flips in different points of the helices. (B) Same as in (A) but for an helix obtained by assembling Au nanodisks (50 nm diameter, 40 nm thick, excitation at 900 nm). (C-D) Sketch of helical Au NPs structures assembled on DNA scaffolds (C) and CD spectra corresponding to the left-handed and right-handed helices. Reprinted with permissions from ref.[403] (A, B) and [405] (C).

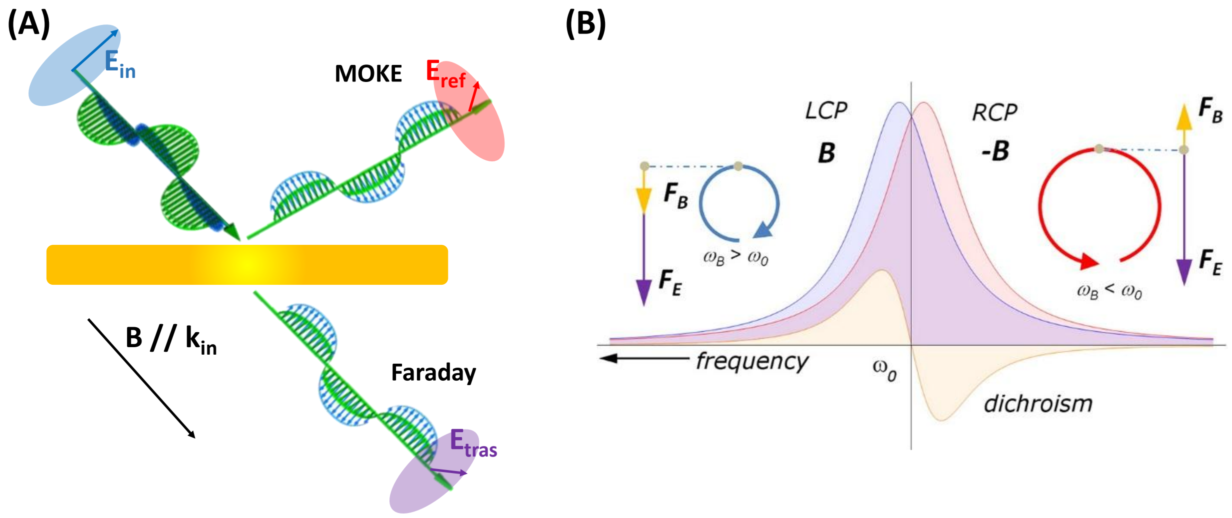

Figure 28. (A) Simplified sketch of MOKE and Faraday effects: in case of linearly polarized light and external magnetic field applied along light propagation direction, there is a rotation of the polarization of the reflected beam (MOKE) or of the transmitted beam (Faraday). (B) Scheme of the process leading to MCD (orange line) in Au NPs, resulting from the difference between the left (blue) and right (red) circular plasmonic modes excited with left-handed or right handed circular polarized light (LCP or RCP), in presence of an external magnetic field B perpendicular to the orbital plane. The electric (F_E) and magnetic (F_B) components (both radial in direction) of the Lorentz force acting on the electrons change for LCP and RCP plasmon excitation. Reprinted with permission from ref.[415].

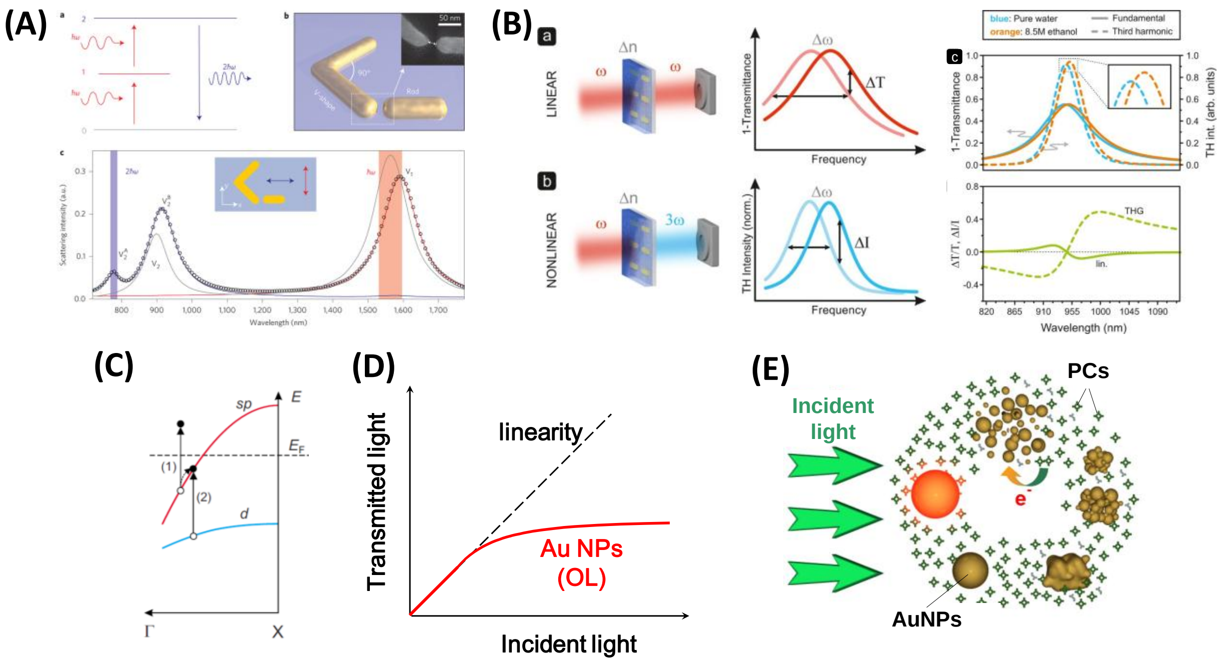

Figure 29. (A) Simplified Jablonski diagram for SHG (a), sketch of an Au nanostructure satisfying the requirements described in the text for optimal SHG (b), and (c) calculated scattering spectra of the isolated V-shaped antenna (grey line) and of the coupled antenna (open black circles). Blue and red lines represent the scattering spectra of the coupled antenna when illuminated with light polarization parallel and orthogonal to the long axis of the nanorod, respectively, showing overlap with the fundamental (red stripe) and the SH (blue stripe) lines. Reprinted with permission from ref.[424]. (B) Principle of linear and nonlinear plasmonic sensing based on a refractive index difference Δn: (a) in the linear SPR sensing, the difference of transmittance (ΔT) at a given frequency ω is tracked; (b) in nonlinear sensing, the SPR is excited at the same frequency of (a), and the resonantly enhanced TH signal (3ω) is detected. (c) The THG resonance is narrower due to its nonlinearity, generating a larger signal, as shown by the spectra obtained for the same nanoantenna in pure water (blue) and 8.5 M ethanol solution (orange). Reprinted with permission from ref.[428]. (C) In 2PPL, the first photon (1) induces an sp-sp intraband transition, and the second photon (2) induces a d-sp interband transition from to the empty state generated in the conduction band, then the e-h couple relaxes radiatively. (D) Au NPs are recognized for their excellent ability to limit the intensity of transmitted light when a critical threshold is exceeded. (E) Au NPs fragmentation, which occurs during OL, can be avoided by a self-repair mechanism in the presence of Pcs: the Pcs promote the assembly of photofragmented Au NPs into larger aggregates, that are photomelted to reform bigger Au NPs ready to efficiently limit light again. Reprinted with permission from ref.[14, 435].